PHASE SEPARATION AND SECOND PHASE PRECIPITATION IN BETA TITANIUM ALLOYS

Arun Devaraj, B.Tech.

Dissertation Prepared for the Degree of

DOCTOR OF PHILOSOPHY

UNIVERSITY OF NORTH TEXAS

May 2011

APPROVED:

Rajarshi Banerjee, Major Professor
Srinivasan Srivilliputhur, Co-Major Professor
Alan Needleman, Committee Member
Soumya Nag, Committee Member
Hamish Fraser, Committee Member
Narendra Dahotre, Chair of the Department of Materials Science and Engineering
Costas Tsatsoulis, Dean of the College of Engineering
James D. Meernik, Acting Dean of the Toulouse Graduate School

Devaraj, Arun. Phase separation and second phase precipitation in beta titanium alloys. Doctor of philosophy (Material Science and Engineering), May 2011, 155 pp., 4 tables, 59 illustrations, references, 157 titles.

The current understanding of the atomic scale phenomenon associated with the influence of beta phase instabilities on the evolution of microstructure in titanium alloys is limited due to their complex nature. Such beta phase instabilities include phase separation and precipitation of nano-scale omega and alpha phases in the beta matrix. The initial part of the present study focuses on omega precipitation within the beta matrix of model binary titanium-molybdenum (Ti-Mo) alloys. Direct atomic scale observation of pre-transition omega-like embryos in quenched alloys, using aberration-corrected high-resolution scanning transmission electron microscopy and atom probe tomography (APT) was compared and contrasted with the results of first-principles computations performed using the Vienna ab initio simulation package (VASP) to present a novel mechanism of these special class of phase transformation. Thereafter the beta phase separation and subsequent alpha phase nucleation in a Ti-Mo-Al ternary alloy was investigated by coupling in-situ high energy synchrotron x-ray diffraction with ex-situ characterization studies performed using aberration corrected transmission electron microscopy and APT to develop a deeper understanding of the mechanism of transformation. Subsequently the formation of the omega phase in the presence of simultaneous development of compositional phase separation within the beta matrix phase of a Ti-10V-6Cu (wt%) alloy during continuous cooling has been investigated using a combination of transmission electron microscopy and atom probe tomography. The results of these investigations provided novel insights into the mechanisms of solid-state transformations in metallic systems by capturing the earliest stages of nucleation at atomic to near atomic spatial and compositional resolution.

ACKNOWLEDGMENTS

First and foremost I would like to thank my advisor Dr. Rajarshi Banerjee for his guidance that took me unobstructed throughout this course of PhD. Also I am thankful to Dipa‟Di and Ritu for your care and affection. I would also like to thank my co advisor Dr. Srinivasan G. Srivilliputhur for introducing me to the interesting world of first principle computations. Thank you for your guidance and inspiration.

I would also like to thank Dr. Hamish Fraser who has been kind enough to let me work on the collaborative research projects with CAMM, OSU. I am also thankful to Dr. J. Tiley, the AFRL program manager of ISES for providing the financial support for all the research works presented here. I am highly grateful to Dr. Barry C Muddle and Dr. HP Ng from ARC Center of Excellence in Design of Light Metals, Monash University. From the UNT research group I would like to thank Dr. Junyeon Hwang and Dr. Soumya Nag for their invaluable guidance. I would also like to thank Dr. Robert E Williams, Dr. R. Srinivasan, Dr. Babu Vishwanathan, Niraj Gupta and Dr. David Diericks. I would also like to appreciate the help of Dr. Soma Chattopadhyay and Dr. Yang Ren from 11IDC beam line of APS, Argonne National Lab in getting the beam time and guiding through the in situ HEXRD work. The help from three „office angels‟ Joan Jolly, Wendy Agnes and April Portor was invaluable. The friendship and camaraderie from my fellow friends Antariksh singh, Sundeep Gopagoni, Kristopher Cody Mahdhak, Ankit Srivastava, Peeyush Nandwana, Anchal Sondhi, Shivraj Karewar, Ming Te lin, Fang Ling Kuo, Ming Hang Lin and Wei Lun Tu made these four years of my PhD life a unique memory of my lifetime. I would also like to acknowledge the friendship from Dr. Rama Bommaraju, Dipak Rajput, Kiran Chandran, Sonia Samuel and Vandana Jain. Finally my life wouldn‟t have been possible without my loving Dad, Mom, Brother and Grandmother. I will always be grateful for your love and affection.

TABLE OF CONTENTS

Page

LIST OF TABLES

LIST OF FIGURES

CHAPTER 1

INTRODUCTION

1.1 Motivation

Titanium and its alloys have been used for aerospace applications since several decades. Their higher strength to weight ratio in combination with high corrosion resistance and compatibility to composite structures made them a better candidate material in comparison to steel and aluminum alloys for aerospace application [1, 2]. However a widespread usage of titanium alloys has been limited because of the cost of production and processing. This motivated significant research to develop lower cost titanium alloys by optimizing composition and processing conditions. Initially α and α/β titanium alloys were the predominant alloys used for aerospace applications. More recently β titanium alloys started to find increasing attention due to their reduced elastic modulus and capability to attain a wide range of strength levels by heat treatment, offering a wider processing window in comparison to α or α/β titanium alloys [2, 3]. This necessitated a deeper understanding of different phase transformations possible within the β phase of β titanium alloys including β phase separation and precipitation of ω and α phases. However the understanding of microstructure evolution in β titanium alloys on heat treatments is still at its infancy which is attributable to the complexity of the different pathways for microstructure evolution available in these alloys [4, 5].

1.2 Contributions of the Dissertation

This present work is directed towards improving the fundamental understanding of β phase separation and precipitation of ω phase in the β titanium alloys. Both β phase separation and ω phase precipitation influence the nucleation site, morphology, distribution, size scale and growth kinetics of equilibrium α phase in β titanium alloys. Such an understanding would help

us to better engineer the processing conditions of β titanium alloys to obtain a custom tailored microstructure that could offer the property requirements for any application.

Titanium-molybdenum binary alloy with 18 wt% Mo was chosen to investigate the ω phase precipitation. The detailed characterization results obtained using advanced characterization tools like aberration corrected high resolution transmission electron microscopy (HRTEM), high resolution scanning transmission electron microscopy (HRSTEM) and three dimensional atom probe tomography (APT) was coupled with first principle computations performed using Vienna ab-initio simulation package (VASP) density functional theory (DFT), to better understand the nucleation and growth of ω precipitates in these β titanium alloys. Subsequently the ω phase was destabilized by adding 5% Al to Ti-20Mo binary alloy and the progress of β phase separation and subsequent nucleation of α phase in Ti-20Mo-5Al was studied in detail by coupling the above said characterization tools with in situ high energy X-ray diffraction performed at the advanced photon source in Argonne national lab. Finally the coexistence of both β phase separation and ω phase formation was investigated in the ternary Ti-10V-6Cu alloy. These fundamental investigations on binary and ternary alloys helped to develop newer insights toward the mechanism of β phase separation and second phase precipitation in β titanium alloys.

1.3 Organization of Dissertation

This dissertation is divided into eight chapters. Chapter 2 presents a background of β titanium alloys. Initially different phases and phase transformations possible in β titanium alloys are introduced. A brief history of application of β titanium alloys in aerospace industry is given later. Chapter 3 describes the different characterization and computational tools employed for

the current study. In addition, a description of the processing of all the investigated binary and ternary alloys is also included in the chapter.

The results and discussions of the present work are given in the next 4 chapters. Chapter 4 starts off by introducing past research attempts to understand the β to ω phase transformation in β titanium alloys. Subsequently the advantage of the current research work performed is justified through the results of characterization of ω phase precipitation and growth during isothermal ageing of Ti-18% Mo binary alloy. Also the new insights obtained by the current study are highlighted by comparing and contrasting the current research results obtained, with the past research attempts in similar alloy systems. The chapter is ended by motivating the effort of using first principle computation techniques to understand the energetic of the β to ω phase transformation. Chapter 5 introduces the result of first principle computations performed using VASP DFT Nudged elastic band method in Ti-Mo binary alloy system. At the end of the chapter, the computational results are coupled with the experimental results given in chapter 4 to highlight the new insights obtained towards β to ω phase transformation mechanism.

Chapter 6 talks about the second aspect of the current work- β phase separation. The experimental results of probing the β phase separation and subsequent nucleation of α phase in Ti-20Mo-5Al alloy is presented in this chapter. The advanced in situ and ex situ characterization results show the development of crystallographic and compositional partitioning during phase separation and subsequent α nucleation.

Chapter 7 presents the investigation of concurrent β phase separation and ω phase formation in Ti-10V-6Cu ternary alloy. Role of β phase separation in dictating the misfit and thereby the resultant ω phase morphology is highlighted by comparing the resultant microstructure after water quenched condition and air cooled condition. As a result, formation of

ω phase in the presence of simultaneous development of compositional modulations within the β matrix is presented using three dimensional atom probe and transmission electron microscopy (TEM) studies.

Chapter 8 summarizes the entire work and presents the future work possibilities to explore the subject in further detail.

1.4 References

[1] Collings EW; Physical metallurgy of titanium alloys; Chapter 5

[2] Boyer RR, Briggs RD. Journal of material engineering and performance 2005;14(6):681.

[3] Nyakan SL, Fanning JC, Boyer RR. Journal of material engineering and performance, 2005;14(6):799.

[4] Nag S, PhD Dissertation, Ohio State University; 2008.

[5] Williams REA, PhD Dissertation, Ohio State university; 2010.

CHAPTER 2

LITERATURE REVIEW

2.1 Introduction

In this chapter a general introduction of β titanium alloys are given. The chapter begins with an overview of the different equilibrium and non equilibrium phases observed in β titanium alloys. Subsequently a description of the different phase transformations in β titanium alloys is given. Also discussion is focused on the role of β phase instabilities in dictating the microstructure evolution in commercial and model β titanium alloy systems. A brief history of the use of β titanium alloys in aerospace industry is presented in the last section of the chapter.

2.2 β Titanium Alloys

β titanium alloys are defined as those titanium alloys with enough concentration of β stabilizing elements to facilitate the retention of 100% of the β phase at room temperature during water quenching from temperatures above β transus [1, 2]. Hence β titanium alloys are not expected to form athermal or stress induced martensite during water quenching. Higher yield strength values can be obtained by precipitating high volume fraction fine scale, undeformable α phase particles from the metastable β phase of β titanium alloys. [3].

2.3 Phases in β Titanium Alloys

Titanium exhibit allotropic transformations with the equilibrium low and high temperature phases (at 1 atm pressure) being the hexagonal close packed (hcp) α and body-centered cubic (bcc) β phases, respectively [1]. The phases in β titanium alloys can be broadly classified into equilibrium and non-equilibrium phases. Equilibrium phases form only when sufficiently long time is given for phase transformation to reach the steady state conditions as

dictated by the phase diagram. Thus equilibrium phases present at any condition of pressure, temperature will have the lowest possible Gibbs free energy. Non-equilibrium phases essentially will represent either a local minima of the Gibbs free energy or could be a "frozen" unstable equilibrium state of the alloy due to kinetic constraints. Such non-equilibrium phases can be formed in thermal treatments faster than the treatment conditions required to form equilibrium phases. These higher free energy phases will transform to lower free energy equilibrium phases on availability of sufficient time and energy for the transformation [1, 4].

2.3.1 Equilibrium β and α Phases

The body centered cubic (BCC) structured β phase forms on heating α phase of elemental Titanium above 883^{o}C (known as β transus temperature). The β titanium has $Im\bar{3}m$ space group with two atoms per unit cell at (0,0,0) and (1/2,1/2,1/2) coordinates. The stabilization of β phase at higher temperature is attributed to the capability of its open structure to accommodate higher vibrational entropy resulting in a net reduction in Gibbs free energy of the phase at the elevated temperatures. Alloying additions of V, Mo, Nb, Hf, Ta, Mn, Cr, Cu, Ni, Fe, Co, Au, Ag, W, Pt and Pd lower the β transus temperature and cause a stabilization of β phase at lower temperatures [1, 4]. These β stabilizing elements are mainly classified into β isomorphous and β eutectoid forming systems. Ti with V, Mo, Nb, Ta or Hf are β isomorphous systems and forms solid solution at most of the temperatures. Fe, Cr, Mn, Co, Ni, Cu, W, Au, Ag, Pt and Pd are β eutectoid forming systems due to the formation of a eutectoid compound at certain temperatures [1]. Some of the β isomorphous systems undergo a β phase separation reaction at higher β stabilizing element concentrations. This is essentially due to positive enthalpy of mixing of these elements leading to a positive curvature of the free energy-composition plot of β phase. This effect is sometimes represented as a monotectoid system with

a presence of miscibility gap in the phase diagram [1, 4]. A typical β monotectoid phase diagram is shown in Fig. 2.1.

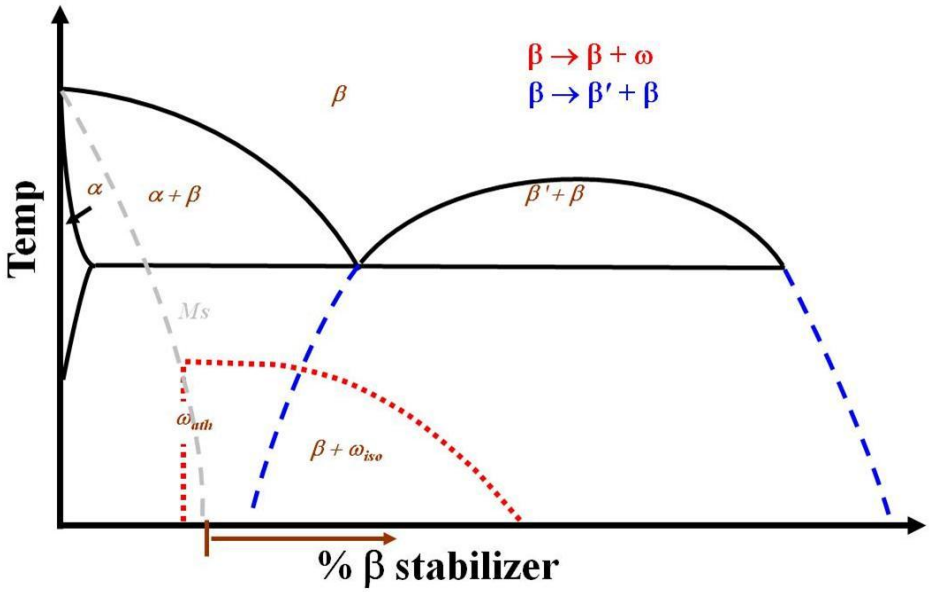

Fig. 2.1 Typical β monotectoid phase diagram showing the superimposed region of athermal and isothermal ω phase formation.

Additions of β stabilizers are also known to lower the martensitic start temperature below room temperature. This feature is used to get a quantitative value for the β phase stabilization effect of individual elements in terms of Mo equivalency [4]. The Mo equivalency is calculated as follows.

[Mo]eq = [Mo] + 0.2 [Ta] + 0.28 [Nb] + 0.4 [W] + 0.67[V] + 1.25 [Cr] + 1.25 [Ni] + 1.7 [Mn] + 1.7 [Co] + 2.5 [Fe]

Pure Ti is stable in the hexagonal close packed (HCP) structure of α at room temperature [4]. The space group of α is $p6_3mmc$ with two atoms at (0,0,0) and (1/3,2/3,1/2) positions. The equilibrium α phase is precipitated on ageing the β titanium alloys below the β transus temperature or slow cooling from temperatures above β transus [1]. The nucleation sites for α phase can be classified into intra-granular and inter-granular nucleation sites. Prior β grain

boundaries constitute the inter-granular nucleation sites for β. The intra-granular nucleation sites of α are at or near ω precipitates, β‟ precipitates, dislocations and other dispersoids like oxides and carbides [1, 5]. The density of nucleation sites for α can be increased by achieving a greater thermodynamic driving force by faster cooling rates and lower ageing temperatures [5]. Alloying elements like Al, Ga, B, Sc, La, Ce, Ge, C, O and N raise the β transus temperature and hence are called as α stabilizers [4]. These are simple metals or interstitial elements. Except N and O, all elements given above, form peritectoid systems with Ti. N and O form simple peritectic system with Ti. Al is the most commonly used α stabilizer. Hence the effectiveness of α stabilizers is calculated using an Al equivalency as given in the following equation [1, 4, 6].

$$[Al]eq = [Al] + 0.17\,[Zr] + 0.33\,[Sn] + 10\,[O]$$

2.3.2 Metastable and Equilibrium ω Phase

The equilibrium ω phase has been reported to form in pure elemental Ti and Zr at high pressures [1]. Metastable ω phase forms on rapidly cooling Ti and Zr alloys containing a critical concentration of β stabilizing elements from the high temperature single β (body centered cubic, BCC structure) phase field and on subsequent isothermal annealing [1, 2, 4]. These multiple phases encountered in Ti and Zr alloys (or in general Group IV elements) can be attributed to the competing structural and compositional instabilities, inherent within the BCC β phase of these alloys, on quenching from high temperatures. This metastable ω phase has intrigued researchers and has been the subject of considerable study over many years, not only due to the complexity associated with its mechanism of formation but also due to its influence on the mechanical and superconducting properties [4, 7-9]. The space group of ω phase can be either p6/mmm or p-3m1 depending on the extent of transformation [1, 10, 11]. In the early stages of transformation ω phase assumes a trigonal symmetry with atoms at (0, 0, 0) and (±2/3, 1/3, μ) with μ = 0.48±0.01

[11]. On complete transformation ω phase has a hexagonal symmetry with atoms located at (0, 0, 0) and (± 2/3, 1/3, 1/2) positions [11]. The trigonal symmetry of ω phase on early stages of the phase transformation is postulated to generate diffuse intensity spots in selected area electron diffraction instead of sharp ω spots [12]. Based on the lattice misfits, the morphology of ω phase can either be cuboidal or ellipsoidal in Ti-Transition metal alloys [13, 14]. Hence the high misfit binary alloys of Ti-V, Ti-Cr, Ti-Mn, and Ti-Fe are reported to have a cuboidal morphology driven by a reduction in matrix elastic energy. The low misfit binary alloys of Ti-Mo and Ti-Nb are reported to form ω precipitates with ellipsoidal morphology facilitating a minimization of anisotropic surface energy [13, 14]. The critical misfit value is quoted to be 0.5% below which the morphology will be ellipsoidal and higher misfit values will lead to cuboidal morphology of ω phase [15, 16]. As expected the temperature stability of ω phase is also directly related to the lattice misfit. The ω phase in low misfit alloys are expected to be stable to higher temperatures and the ω phase in high misfit systems are expected to decompose to α phase at comparatively lower temperatures [13]

2.4 Phase Transformations in β Titanium Alloys

2.4.1 Diffusional β to α Transformation

The final mechanical properties exhibited by a β titanium alloy is directly dependent on the morphology, size scale, volume fraction and distribution of the α phase .The α phase in β titanium alloys can be classified into three types based on the nucleation site [1, 4].

1. Allotriomorph α that precipitates at the β/β grain boundaries.
2. Inter-granular α that form as lath shaped precipitates growing from grain boundary α into the β grains.

3. Intra granular α that nucleate and grow within β grains at ω precipitates, dislocations and inclusions [17].

In precipitation reactions an orientation relationship (OR) is usually found between the precipitate and matrix phase. These orientation relationships are preferred due to minimization of interfacial energy possible in such inter-phase orientations. The orientation relationships between α and β are given below.

Burgers: $(0001)\alpha \parallel \{011\}\beta$; $<11\bar{2}0>\alpha \parallel <1\bar{1}1>\beta$; $\{1\bar{1}00\}\ \alpha \parallel \{121\}\beta$

Pitsch-Schrader: $(0001)\ \alpha \parallel \{011\}\beta$; $<11\bar{2}0>\ \alpha \parallel <100>\ \beta$; $\{1\bar{1}00\}\ \alpha \parallel \{0\bar{1}1\}\beta$

Potter: $(0001)\ \alpha\ 2^{o}$ from $\{011\}\beta$; $<11\bar{2}0>\ \alpha \parallel <1\bar{1}1>\ \beta$; $\{1\bar{1}01\}\ \alpha \parallel \{0\bar{1}2\}\beta$

Rong-Dunlop: $(0001)\ \alpha \parallel \{021\}\ \beta$; $<11\bar{2}0>\ \alpha \parallel <100>\ \beta$; $\{1\bar{1}00\}\ \alpha \parallel \{0\bar{1}2\}\beta$

Burgers OR is the most commonly observed orientation relationship between HCP and BCC phases [18] however others are also observed in some cases [19, 20, 21]. Each of the different orientation of α is called as a different variant [1].

Allotriomorph α is postulated to be formed by kink-on-ledge mechanism by one of the early works by Furuhara and Aaronson [22]. Inter granular α can be observed to have either the same orientation as the grain boundary α or can be a different variant. Both of these conditions are postulated to be formed as the result of two distinctly different mechanisms. The inter granular α of same orientation is expected to be formed due to the instability of grain boundary α/β interface formed by perturbation wavelength [23,24].In such a case the subsequent development of α boundary between grain boundary α and inter granular α is attributed to a „pinch off" mechanism. The inter granular α of same orientation is expected to be formed by a sympathetic nucleation mechanism [25].

One of the detailed works on intra granular nucleation of α was performed by Furuhara et al. by ageing Ti-10, 20, 30, and 40% Mo alloys at lower temperatures. The difference in morphology, habit plane, growth kinetics and volume fraction of α formed at different temperatures were used as a measure to postulate the influence of a β phase separating tendency on α phase precipitation in Ti-Mo alloy system [26]. The effect of ω phase on nucleation of α during low temperature ageing of Ti-10V-2Fe-3Al was studied by Duerig et al. and Ohmori et al. [27, 28]. In their works, low temperature ageing below 400^{o}C resulted in the formation of fine platelets of α, possibly nucleated by ω phase.

2.4.2 β to ω Phase Transformation

The metastable ω phase has been classified into athermal and isothermal (or thermally-activated) types. The athermal ω precipitates have typically been observed in alloys quenched from the high-temperature β phase-field, retaining the composition of the parent β matrix, and form by a diffusionless, pure displacive, collapse of the {111} planes of the BCC phase via a shuffle mechanism [29-31]. In contrast, the isothermal ω precipitates have been postulated to form via a thermally-activated process involving diffusion-based compositional partitioning followed by the collapse of {111} bcc planes in the regions depleted in β destabilizing elements [15,29, 30, 32]. The schematic diagram of the atomic collapse resulting in β to ω phase transformation is given in Fig. 2.2. Therefore, from the viewpoint of instabilities in the β phase, the athermal ω results from a pure structural instability while the isothermal ω results from concurrent compositional and structural instabilities. Eventually, on annealing for long periods of time these metastable ω precipitates are replaced by the equilibrium α phase, the former having a significant influence on the morphology, size scale and distribution of the latter [33].

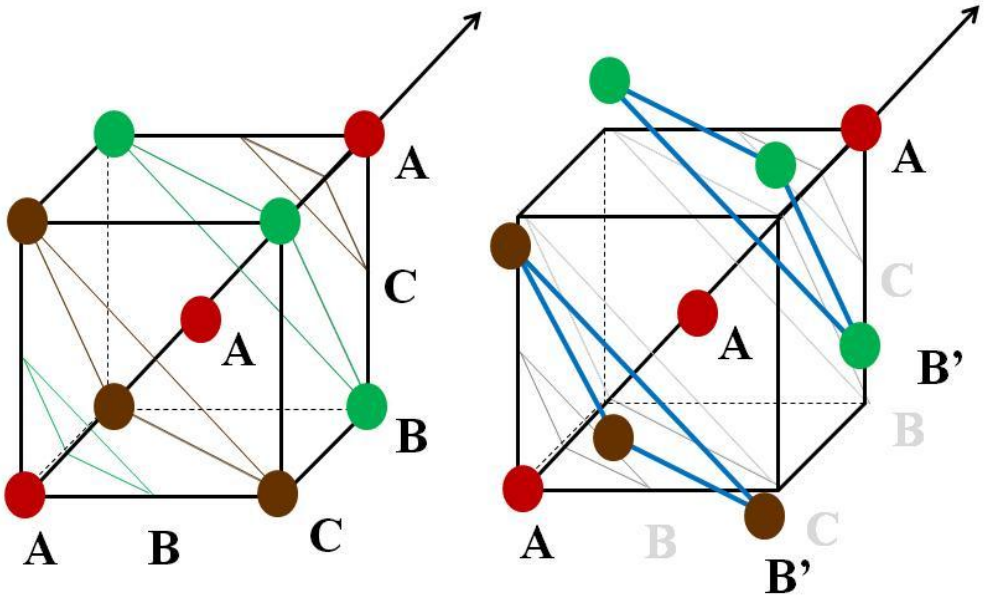

Fig. 2.2 Schematics of β to ω transformation (a) The ABCABC stacking of (222) planes in initial BCC β phase (b) The final AB‟AB‟ stacking in ω phase.

The orientation relationship between β and ω can be defines as

$$(0001)\omega//(111)\beta;\ <11\bar{2}0>\omega//<110>\beta$$

This orientation relationship can be clearly visualized in the schematics of β to ω phase transformation shown in Fig. 2.3.

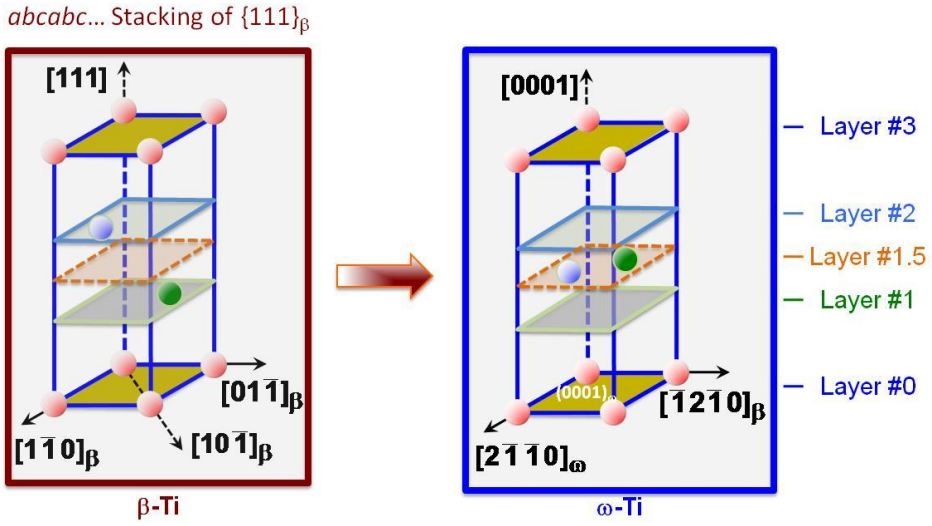

Fig. 2.3. The schematics of β to ω transformation.

Therefore a_ω can be defined as $\sqrt{2}a_\beta$ and c_ω is $(\sqrt{3}/2)a_\beta$. Four variants of ω can be formed along four nonequivalent <111> directions in the β matrix [4]. The presence of ω phase precipitates in β matrix can be found by electron diffraction patterns along [113] and $[10\bar{1}]$ zone axis as shown in Fig 2.4 (a) and (b) [29, 34]. All the four variants of ω contribute to the diffraction pattern formed along [113]β zone axis.

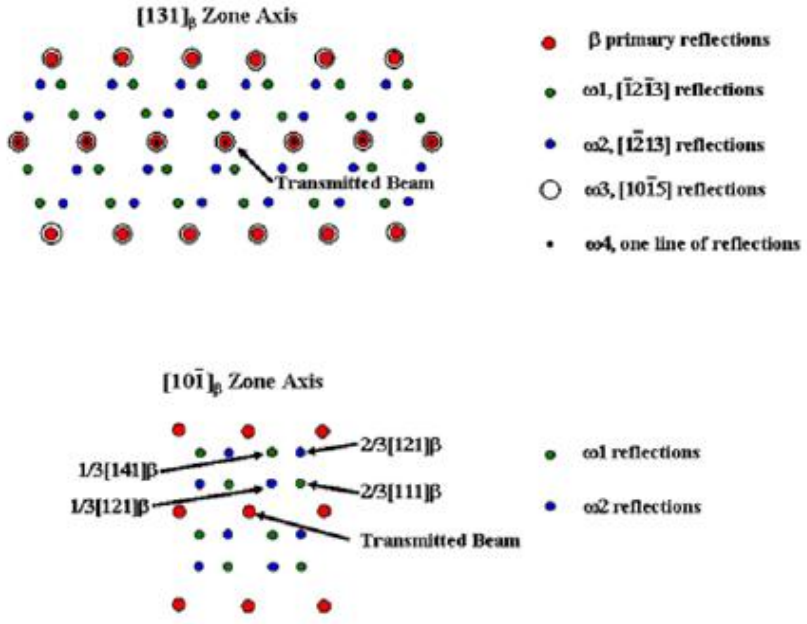

Fig 2.4 (a) [113]β zone axis selected area diffraction showing the additional reflections from four variants of ω phase. (b) $[10\bar{1}]$ β zone axis selected area diffraction pattern showing additional reflections from two ω variants [29, 34].

Overall there has been two mechanistic models postulated for β to ω phase transformation. Both of these models were developed to explain the effects of diffuse intensity development in electron diffraction patterns. The initial „Linear fault mechanistic model" was followed by a „phonon mechanistic model". Each of these mechanisms will be briefly described below [4].

1. Linear fault mechanistic model: Theoretically the ω phase transformation can be viewed to form as a result of a two dimensional ordering of one dimensional linear displacive defects along [111] closed packed direction in the bcc β phase of transition metals and their alloys [35]. This linear defect can either be considered as a displaced segment of close packed [111] atomic rows flanked by a compressive and dilatational defect pair or a vacancy–defect pair where a vacancy is associated with the displaced [111] row of atoms [35, 36]. Such a geometrical model was later proven using frozen phonon calculations by Ho et al. where a pronounced lowering of the ground state energy of Zr was shown for a 2/3<111> phonon, corresponding to the displacement required for forming an ideal ω structure from the parent BCC phase [37]. Subsequent neutron scattering experiments in β Ti also showed instabilities corresponding to the 2/3<111> wave vector in the phonon spectra [38]. The weak restoring force for [111] line segment displacements in Zr was attributed to electronic effects based on ab initio calculations [9]. This linear defect can also be viewed as collapsing every alternate (111)β planes by a distance of 1/6th of <111> direction. The movement of atoms on such a collapse is shown schematically in Fig. 2.5 using hard sphere model [4].

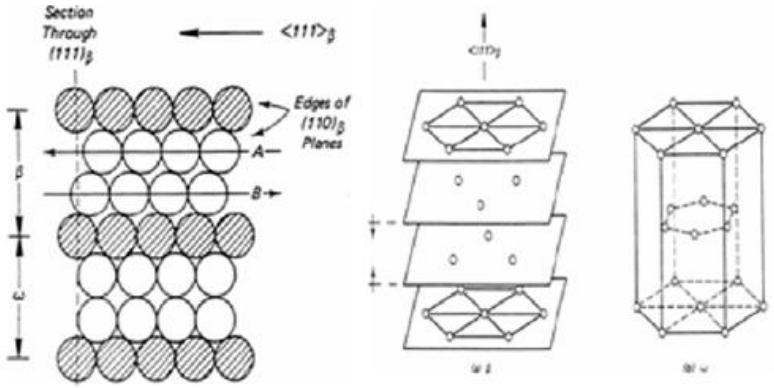

Fig. 2.5 Linear fault mechanism of β to ω phase transformation [4].

As per such a mechanism the trigonal symmetry of β lattice along <111> direction is maintained on partially transformed situations. On completion of the collapse a hexagonal symmetry is developed along <111> β direction. This transformation can happen either along a single row of atoms or an entire region of neighboring rows can be transformed. This model could explain the formation of sharp spots or straight lines of intensity formed in electron diffraction patterns since diffuse ω reflection can originate from rows of particles or isolated particles. However this mechanism could not prove the reversibility of β to ω transformation with temperature [39]. Several HRTEM works by sukedai et al. in Ti-Mo alloys also provided proof of linear fault mechanism of β to ω transformation [34, 40, 41]. In chapter 4 further details on past characterization efforts for investigating β to ω phase transformation is compared and contrasted with the current work performed.

2. Phonon mechanistic model: This model was developed by De. Fontaine et al. to explain the dependency of temperature and composition on the diffuse ω reflection and reversible athermal ω formation [29]. This model assumes the parent β lattice to be a stack of (111) planes in ABCABC stacking order along <111> direction. The β to ω transformation is proposed to be the result of a longitudinal phonon with a maximum amplitude of 2/3<111>β propagating along the <111>β direction. The local amplitude of the planes is indicated by the point of intersection of the plane with the sinusoidal wave in such a way that the planes intersecting the wave at zero or 1 amplitude remains stationary and the planes intersecting the wave at 1/3 or 2/3 move to 1/2. This mechanism and final ω structure is given in Fig. 2.6. Effectively such a transformation would transform the ABCABC stacking of (111)β lattice planes to an AB‟‟AB‟‟ packing in the final ω structure [35]. This mechanism explains the diffuse streaking observed in electron diffraction to be the result of intermediate trigonal, partially transformed ω structures due to

effect of composition and temperature. Also this mechanism can explain the reversibility of electron diffraction from curvilinear diffuse streaking to straight lines of athermal ω reflection [29].

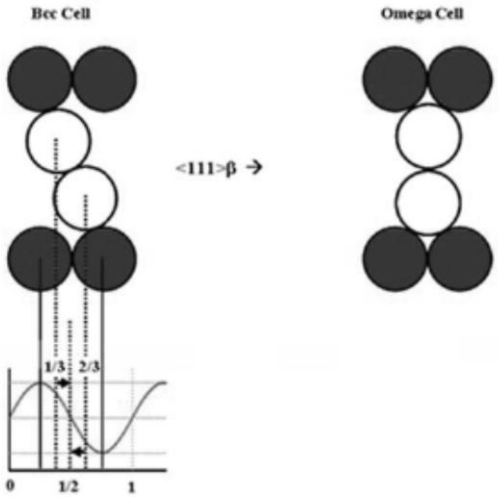

Fig. 2.6(a) Schematic of phonon mechanistic model (b) Final ω structure formed after transformation [4].

Although there have been multiple studies conducted on ω phase formed during both quenching and subsequent isothermal aging, the details of the $\beta \rightarrow \beta + \omega$ transformation on quenching, followed by partitioning of elements across the β/ω interface on isothermal aging remain incompletely understood [15, 30, 31, 32, 42]. The morphology and composition of ω precipitates in alloys involving multiple alloying elements (i.e. commercial engineering alloys) can be substantially more complex in nature. The nature of and interactions between the β-stabilizing elements present, as well as the paths and rates employed when cooling from the high temperature single β phase-field, can play a dominant role. The nanometer size scale (< 20nm) of early-stage ω domains has traditionally made it rather difficult to determine the composition and 3D morphology accurately. Recently, by coupling atom probe tomography (APT) with

transmission electron microscopy, the accurate 3D morphology, dimensions, and composition of ω precipitates in a binary, low misfit Ti-Mo alloy have been reported [43].

2.4.3 α Nucleation from ω

Uniformly distributed fine scale α phase formed in β titanium alloys on low temperature ageing studies are usually associated with an ω assisted nucleation event. Such fine scale uniform distribution of α cause considerable strengthening of β titanium alloys [1, 4]. As given above, there are two types of morphology of ω phase observed based on the lattice misfit. A variation is observed in the nucleation mechanism of α from these two different morphologies of ω. Through several past research works, the nucleation site of α in high misfit systems have been identified as the dislocations and ledges at the ω/β interface [13, 44, 45, 46]. However there has been considerable controversy regarding the nucleation of α from low misfit systems with ellipsoidal ω. Two distinct versions of thought on this matter have been developed over years.

1. α nucleates inside the ω particles and consumes the latter during its growth
2. α nucleates coherently at the ω/β interface with an orientation relationship with both β and ω phases.

Recently using high resolution transmission electron microscopy (HRTEM) imaging Prima et al. showed the nucleation of an α particle in the core of ω phase followed by dissolution of ω on coarsening of the nucleated α [47]. Through their work a model of displacive transformation of ω core to α was proposed as the mechanism of nucleation of α from ω. The α plate growth is proposed to be limited in the coherent direction and faster in the incoherent direction. However there has also been some experimental works showing nucleation of α at or near β/ω interface [48, 49]. Azimdazeh et al. postulated the nucleation of α at a distance from

β/ω interface based on atom probe results in Ti-6.8Mo-4.5Fe-1.5Al low cost β alloy [48]. One another recent work by S. Nag et al. showed coexistence of β, ω and α in Ti-5Al-5Mo-5V-3Cr-0.5Fe alloy after ageing for 350^{o}C for 2hours [33].

2.4.4 β Phase Separation (β->β_1+β_2)

Phase separation is a consequence of positive enthalpy of mixing of two elements in a solid solution. A positive enthalpy of mixing introduces a hump in the free energy composition plot at lower temperatures which translates to a region of miscibility gap in the phase diagram [50]. Fig. 2.7(a) shows a schematic phase diagram of the miscibility gap region of a β titanium alloy with positive enthalpy of mixing between components. Fig. 2.7(b) shows the corresponding free energy-composition diagram (G-X plot) at temperature T within the chemical spinodal region of the phase diagram. The composition boundary of the miscibility gap at temperature T is defined by the lowest free energy points in the G-X curve denoted by the $X^{o}_{\beta 1}$ and $X^{o}_{\beta 2}$ in Fig. 2.7(b). The point of inflection of the curve satisfying the condition of $\frac{\partial G^2}{\partial X^2} = 0$; will define the chemical spinodal region within which an alloy will phase separate by spinodal decomposition mechanism. If the alloy composition lies outside the inflection point in the free energy-composition plot, it will phase separate by nucleation and growth mechanism [42]. However In real alloy system there is an additional positive contribution of elastic strain energy and interfacial free energy to the final free energy term. Such a free energy term was proposed by Cahn and Hillert [51, 52]. The resulting Cahn free energy (Φ) curve will be positioned higher in the free energy-composition plot due to the addition interfacial energy term. The red curve in Fig. 2.7(b) shows the variation in Cahn free energy with composition. As a consequence an additional coherent miscibility gap region is introduced within the chemical miscibility gap region of phase diagram.

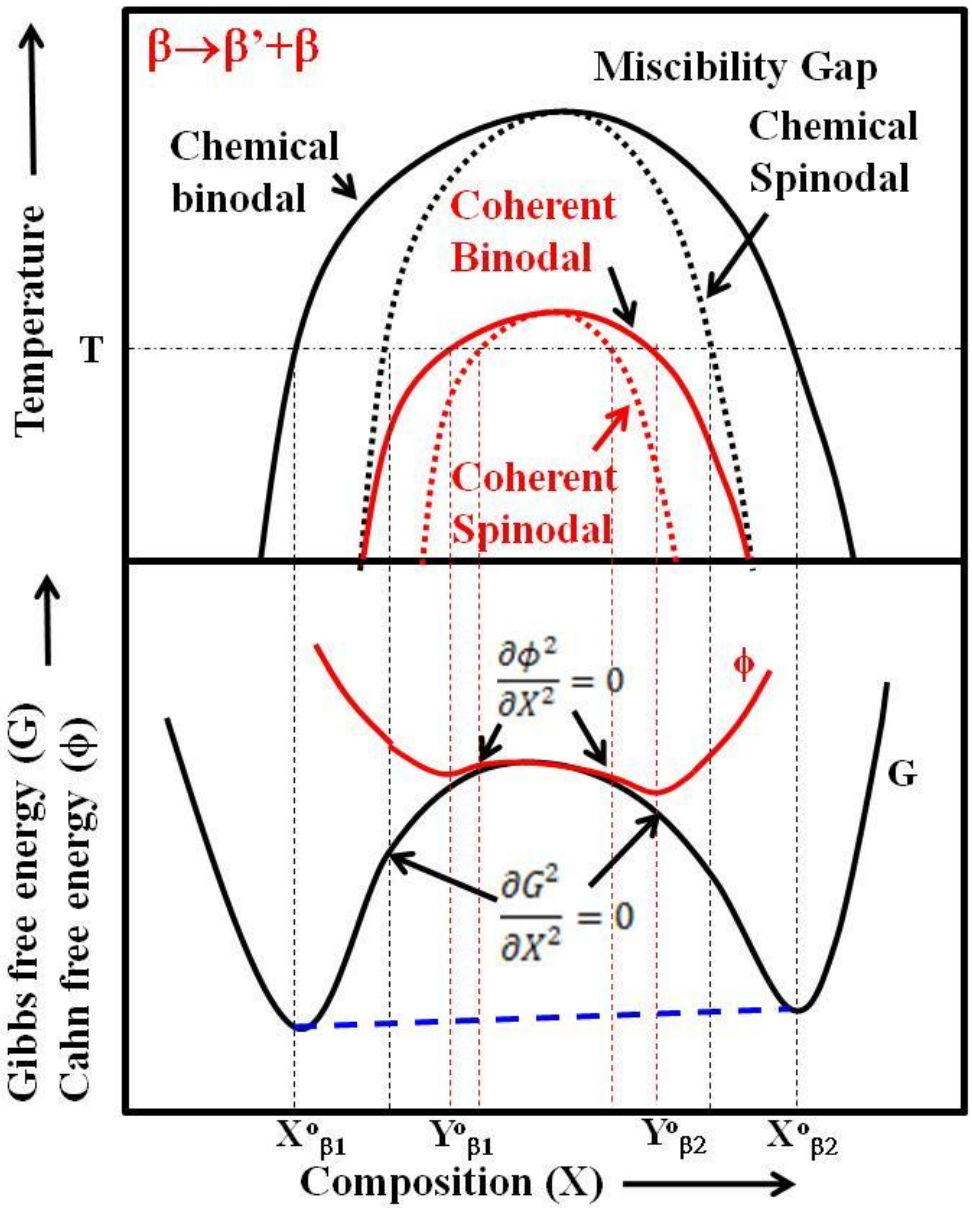

Fig. 2.7(a) The miscibility gap region of a hypothetical alloy with positive enthalpy of mixing of components. (b) The Gibbs free energy vs composition plot and Cahn free energy vs composition plot for temperature T.

For real systems coherent phase separation would happen if the average composition of the alloy lie within the coherent miscibility gap region. The point of inflection of Cahn free energy curve i.e. $\frac{\partial \phi^2}{\partial X^2} = 0$; would define the outer limits of observing a coherent spinodal decomposition in real alloy systems [53]. The phase separation mechanism operative in alloys

will determine the resulting microstructure evolution and properties of the system. Hence over the ages considerable research activity has been focused in understanding the mode of phase separation in metallic systems [54, 55, 56]. Historically the experimental methods to analyze if spinodal decomposition is operative in alloy systems are small angle X-ray scattering, microstructure-time evolution method [57, 58] and analysis of high resolution transmission electron microscopy images for variations in lattice spacing [59]. Presence and progressive development of satellite reflection or peak splitting in electron diffraction and X-ray diffraction data from the initial stage of the transformation is pointed to be a strong indication of spinodal decomposition operating in the system [57].

Phase separation in binary β titanium alloys leads to the formation of a coherent mixture of solute lean and solute rich β structure (β->β1+β2). In past the phase separation tendency in different commercial and model β titanium alloys have been studied by several researchers [16, 26, 60-63]. Phase separation reaction has been reported in Ti-16V-2.5Al [65, 66], Ti-8Al-1V-1Mo [68], Ti-20V [65], Ti-9Mo-7Mn (1-2Al) [68], Ti-13V-11Cr, Ti-13V-11Cr-3Al [69] alloys. A detailed account of the past research efforts in phase separation reaction in model binary alloy systems are presented in chapter 6.

2.4.5 α Nucleation from β_1

The phase separated „solute lean - solute rich" β structure is expected to nucleate α phase on long term ageing. The nucleation site for α phase is postulated to be either β_1/β_2 interface or the solute lean β_1 phase [1, 4]. Furuhara et al. performed a survey of the morphology, kinetics and volume fraction of α formation in Ti-Mo binary alloys to investigate the presence of the monotectoid reaction at lower temperatures [26]. Nucleation of α phase on the solute lean lean β phase of Ti-40% Mo was reported on ageing at temperatures below 550^{o}C. Such α precipitates

were reported to have plate shaped morphology and {013}β habit planes [26]. In another work by Narayan et al. α phase was shown to nucleate in between or near the β_2 particles formed as a result of phase separation reaction during long term ageing of Ti-13V-11Cr-3Al at 400^{o}C [69].

2.5 β Titanium Alloys in Aerospace Industry

The first use of a β titanium alloy on an aerospace application was on the Lockheed SR71 Blackbird [70]. 93% of the aircraft was Ti and the majority of it was a β alloy B120VCA with a composition of Ti-13V-11Cr-3Mo. The high strength levels as high as 1170MPa with only 2% elongation and high temperature stability of this alloy made it the only candidate material for this application available in those times. So its difficulty to melt and fabricate did not act as a hindrance for its usage on this application [70] . Beginning from 1970, the same alloy Ti-13V-11Cr-3Mo was used on McDonnel Douglas DC-10 commercial aircrafts for the titanium springs [71]. These applications were in limited quantities until 1980s in the North American Rockwell B-1B bomber in which about 250 parts were fabricated from Ti-15V-3Cr-3Al-3Sn sheet. Certain advantages like production in strip form and improved formability of this alloy over Ti-6Al-4V along with the heat treatability to higher strength levels upto and higher than 1034Mpa justified the selection of this alloy on a reduced cost basis. The nacelles, sinewave spars and empennage of the B-1B bomber were extensively made from this alloy [2].

In early 1990s Boeing 777 acted as the launch pad for application of several new β titanium alloys for different structural applications. High strength forgings of Ti-10V-2Fe-3Al with minimum ultimate tensile strength levels upto 1193 MPa were used to replace the HSLA steel (4340 or 300 M) on landing gear application resulting in weight savings and extended life due to the improved corrosion resistance of the β titanium alloy in comparison to the HSLA steel parts. Over 200 parts of Boeing 777 were fabricated from the above alloy. Airbus also used the

same alloy for upper links, struts and truck beams of A340-500/600 landing gears. Formed Ti-15V-3Cr-3Al-3Sn sheets were used for environmental control system ducting, clips and brackets and floor support structure in Boing 777. The castings of the same alloy were also used at the strength levels of 1138MPa. Clock type springs with minimum ultimate tensile strength (UTS) level of 1034Mpa were also manufactured from the same alloy. Ti-3Al-8V-6Cr-4Mo-4Zr named β-C was used for coil springs at minimum UTS levels of 1240MPa [2]. A newer generation β titanium alloy β21S with excellent oxidation resistance with improved creep properties and good resistance to attack by thermally decomposed hydraulic fluid was used for the high temperature applications on boeing 777. Later on several other aircraft manufacturers also started using β titanium alloys for different applications following the Boeing 777 design, for weight savings and improved life cycle of various applications like springs and landing gear, reducing the refurbishing and maintenance costs for these parts [2].

Later on β titanium alloys started finding application in helicopters and smaller passenger jet construction. Ti-10V-2Fe-3Al has been used to replace Ti-6Al-4V in rotating applications like disc, sleeve and mast forgings of the Westland Lynx helicopter for superior fatigue performance. In Russia and former Soviet Union an alloy named VT-22 (Ti-5Al-5Mo-5V-1Fe-1Cr) developed at VIAM the All-Russia Institute of Aviation materials has been used extensively for landing gear applications by the aircraft manufacturers due to superior weldability of this alloy [2].

More recently β alloys have been finding wide spread usage as springs due to their high strength, low modulus, low density and high corrosion resistance in comparison to steel. More than 70% weight reduction and cost savings related to maintenance for mitigating corrosion justified the usage of β titanium alloys in applications up and down-lock springs on landing

gear, door counter balance springs, flight control springs for limits and overrides, feel and centering springs for the yoke, pedal returns (brakes) and hydraulic return springs in airframes. Commuter and regional aircraft manufacturers also used β titanium alloy springs for different applications. Some of the examples are Bombardier uses β-C springs for up-lock and down-lock springs, Cessna jet fleet uses Ti-15V-3Cr-3Al-3Sn clock type springs, Embraer uses B120VCA alloy at 1380 Mpa minimum tensile strength for torsion bars in their passenger flights [2].

2.6 References

[1] Collings, EW, The Physical Metallurgy of Titanium Alloys. ASM Series in Metal Processing, ed. H.L. Gegel. 1984, Metals Park, OH: American Sociey for Metals.

[2] Boyer RR, Briggs RD. Journal of mat eng and performance, 2005; 14(6):681

[3] Nyakan SL, Fanning JC, Boyer RR, Journal of mat eng and performance, 2005; 14(6):799

[4] Boyer RR, Welsch G, Collings EW. Materials Properties Handbook: Titanium Alloys, ASM Handbook; 1994.

[5] Bein S, Bechet J. Journal De Physique Iv, 1996;6(C1):99.

[6] Rosenberg HW, "The science, Technology and Application of Titanium" Pegamon press, Oxford, UK, 851 (1970)

[7] Frost PD etal., Trans. Amer. Soc. Metals, 46 (1954), 231.

[8] Bakonyi I, Ebert H, Liechtenstein AI, Phys. Rev. B, 1993;48:7841.

[9] Grad GB, Blaha P, Luitz J, Schwarz K, Fernandez Guillermet A, Sferco SJ. Phys. Rev. B2000;62.

[10] Silcock JM, Davies MH, Hardy H.K. "The Mechanism of Phase Transformations in Solids", Inst. of Metals, 93 (1956).

[11] Bagariatskii, Yu A, Nosova GI, Tagunova TV, Doklady. Akad. Nauk. SSSR, 105, 1225

[12] Sass SL. J. Less-Common Met 1972;28:157.

[13] Williams JC, Blackburn MJ. Trans. TMS-AIME 1969;245:2352

[14] Blackburn MJ. The Science, Technology and Application of Titanium 1970:633

[15] Hickman BS. Trans. TMS-AIME, 1969;245:1329.

[16] Blackburn MJ, Williams JC. Trans. TMS-AIME, 1968;242:2461.

[17] Duerig TW, Williams JC. "Overview: Microstructure and Properties of B Titanium Alloys", B Titanium alloys in the 80‟s: Proceedings of the Symposium, Atlanta, GA, United States, 19-67 (1984)

[18] Burgers WG. Physica 1934;1:561.

[19] Pitsch W, Schrader A. "Arch. Eisenhutt Wes." 1958;29:715.

[20] Potter DI, Jour. Less common Metals 1973;31:299.

[21] Rong W, Dunlop GL. Acta Metall 1984;32:1591.

[22] Furuhara T, Aaronson HI. Acta Metall Mater 1991;39(11):2887.

[23] Mullins WW, Sekerka RF. Jour. Appl. Phys.1963;34(2):323.

[24] Mullins WW, Sekerka RF. Jour. Appl. Phys. 1964;35(2):444.

[25] Aaronson HI, Spanos G, Masamura RA, Vardiman RG, Moon DW, Menon ESK, Hall MG. Mater. Sci. & Engg. B 1995;32:107.

[26] Furuhara T, Makino T, Idei Y, Ishigaki H, Takada A, Maki T. Mater trans, JIM 1998;39(1): 31.

[27] Duerig TW, Terlinde GT, Williams JC. Metall. Trans. 1980;11A:1987.

[28] Ohmori Y, Natsui H, Nakai K. Mater.Trans, JIM 1998;39(1):49.

[29] De Fontaine D, Paton NE, Williams JC. Acta Met 1971;19:1153.

[30] Williams JC, De Fontaine D, Patton NE. Metall. Trans. A 1973;4:2701.

[31] Silcock JM. Acta Metall Mater 1958;6:481.

[32] Duerig TW, Terlinde GT, Williams JC, Titanium „80: Science and Technology 1980:1299.

[33] Nag S, Banerjee R, Srinivasan R, Hwang JY, Harper M, Fraser HL. Acta Met. 2009;57:2136.

[34] Sukedai E, Hashimoto H, Tomita M. Phil. Mag. 1991;64A(6):1201.

[35] De Fontaine D, Buck O. Phil. Mag 1973;27(4):967.

[36] Kuan TS, Sass SL. Acta Metall 1976;24:1053.

[37] Ho KM, Fu CL, Harmon BN. Phys. Rev. B 1983;28:6687; 1984;B 29:1575. Chen Y, Fu CL, Ho KM, Harmon BN. Phys. Rev. B 1985;31:6775.

[38] Petry W, Heiming A, Trampenau J, Alba M, Vogl G. Physica B 1989;156 &157:56.

[39] Williams JC. Titanium Science and Technology 1973:1433.

[40] Sukedai E, Hashimoto H, Hida M. Japan Jour. of Applied Phys 1987;26:L961.

[41] Matsumoto H, Sukedai E, Hashimoto H. Mater Trans, JIM 1999;40(12):1436.

[42] Hickman BS. Jour. Mater. Sci 1969;4:554.

[43] Devaraj A, Williams REA, Nag S, Srinivasan R, Fraser HL, Banerjee R. Scripta Mat 2009;61(7):701.

[44] Takemoto Y, Hida M, Sakakibara A, J. Jpn. Inst. Metals 1993;57:261.

[45] Campagnac MH, Vassel A, The Institute of Metals, London 1986:261.

[46] Feeney MJ, Blackburn MJ. Met. Trans. A 1976;1:3309.

[47] Prima F, Vermaut P, Texier G, Ansel D, Gloriant T. Scripta Mater 2006;54:645.

[48] Azimzadeh S, Rack HJ. Met. and Mater. Trans. A 1998;29:2455.

[49] Ohmori Y, Ogo T, Nakai K, Kaobayashi S. Met. Sc. and Engg. A 2001;312:182.

[50] portor and easterling book

[51] Cahn JW. Acta Metall 1962;10:907.

[52] Hilliard JE. Spinodal decomposition, in: Aaronson HI(eds.). Phase Transformations. Ohio: Am. Soc. Metals.; 1970.

[53] Robert B Heimann. Classic and advanced ceramics; From fundamentals to application, Willey-VCH; 2010.

[54] Merica PD. Trans. AIME 1932;99:13.

[55] Bradley AJ. Proceedings from the Royal Soc. of London (Ser. A), 1943;181:368.

[56] Becker R. Z. Metallk 1937;29:245.

[57] Laughlin DE, Cahn JW Acta Metallurgica, 1975;23:329.

[58] Piers PK Smith. American Mineralogist 1980;65:1038.

[59] Wu CK, Sinclair R, Thomas G. Metallurgical Trans 1978;9A:381.

[60] Kaufman L, Bernstein H. The Science Technology and Application of Titanium 1970:361.

[61] Koul MK, Breedis JF. Acta Met 1970;18:579.

[62] Hoch M, Viswanathan R. Met. Trans 1971;2:2765.

[63] Chandrasekaran V, Taggart R, Polonis DH. Metallography 1972;5:393.

[65] Harmon EL, Troiano AR. Trans. ASM 1961;53:43.

[66] Tanner LE. Trans TMS:AIME 1961;221:74.

[67] Blackburn MJ. Trans ASM 1966;59:694.

[68] Ageyev NE, Novik PK. Russian Metallurgy 1965;5:46.

[69] Hari Narayan G, Archbold TF. Met trans 1970;1:2281.

[70] Boyer RR. Applications of Beta Titanium Alloys in Airframes, in: Eylon D, Boyer RR, Koss DA (Eds.). Beta Titanium Alloys in the 1990"s. The Materials Society.; 1993.

[71] R.R. Boyer. Ti-10V-2Fe-3Al Properties, in: Boyer RR, Rosenberg HW (Eds.). Beta Titanium Alloys in the1980"s. Metallurgical Society of AIME; 1984.

CHAPTER 3

EXPERIMENTAL PROCEDURES

3.1 Introduction

This chapter discusses the different processing and characterization tools used for the work presented in this dissertation. The chapter begins with an introduction to the fabrication and thermal processing of the three fundamental b titanium alloys (Ti-18Mo, Ti-20Mo-5Al and Ti-10V-6Cu) used in the study. Thereafter the discussion is focused on the novel characterization tools and softwares used in characterizing the microstructure of the alloys studied. The first principle computational tools used in this dissertation work are discussed in Chapter 5.

3.2 Processing of β Titanium Alloys

3.2.1 Ti-18wt% Mo Binary Alloy

Ti-18Mo alloy was provided in the form of a 250gm sample from TIMETAL® company, Hederson, NV. The „as received" sample was already homogenized by multiple remelting operations in arc melting furnace followed by rolling at 1100^{o}C after Argon encapsulating in Cp-Ti packaging. The as received sample was again homogenized in the vacuum furnace at 1100^{o}C for 168 hours followed by furnace cooling. Toothpic samples of 1.5mmx 3mm x 40 dimension were made using wire electric discharge machining. The time-temperature cycle of the subsequent heat treatment process are given in Table 3.1. Initially the samples were β solutionized at 1000^{o}C for 30 minutes in electro-thermo mechanical test system (ETMT 8800^{TM}) held in vacuum. Subsequently these samples were rapidly quenched by introducing Ar into the furnace chamber for obtaining a cooling rate of about 10^{o}C/sec. The rapidly cooled samples were subsequently reheated to 475^{o}C and held for 30 minutes and 48 hours followed by water quenching. All the heat treatments of the samples were performed at the

Center for the Accelerated Maturation of Materials, Ohio State University, Columbus, Ohio, USA.

3.2.2 Ti-20wt% Mo-5wt% Al Ternary Alloy

The Ti-5Al-20Mo alloy was fabricated using Laser Engineered Net Shaping (LENS^{TM}). The process of LENS^{TM} has been discussed else were [1]. The oxygen content in the glove box was maintained below 10ppm for the entire deposition. The premixed Ti-5Al-20Mo powder was loaded into the powder feeder hoppers of LENS^{TM}. A mill annealed plate of Ti-6Al-4V was used as the substrate for the deposition. A cylindrical deposit of approximately 4mm height and 10mm diameter was fabricated. The LENS^{TM} deposit was sectioned along the axis of the deposit and was subjected to β solutionizing at 1000^{o}C for 30minutes in an atmosphere controlled Thermcraft tube furnace followed by water quenching. Subsequently the water quenched alloy sample was further sectioned to make two sample pieces. One sample section was subjected to in-situ High Energy X-ray Diffraction (HEXRD) during ageing for 10hours at 400^{o}C at the 11IDC beam line of advanced photon source (APS) of Argonne National Lab. The other sample section was subjected to sequential ex-situ ageing at 400^{o}C for 6hours, 10 hours and 72 hours. Further the 400^{o}C 72hours aged sample was again up-quenched to 620^{o}C and aged for 1hour. All the exsitu heat treatments were done in atmosphere controlled Thermcraft tube furnace. The in situ heat treatment at advanced photon source, Argonne National Lab was performed in an atmosphere controlled Linkam TS 1500 furnace. The time temperature schedule of the heat treatments performed for Ti20Mo5Al is given in Table 3.1.

3.2.3 Ti-10wt% V-6wt% Cu Ternary Alloy

High-purity elemental components were used to melt an alloy of nominal composition Ti-10V-6Cu (wt%) using arc melting under argon atmosphere. The residual oxygen and nitrogen

gas in the chamber was removed by melting a titanium getter before alloy preparation. The alloy was homogenized by six remelting operations. The final alloy button was subjected to heat treatments after encapsulating in quartz tube, back-filled with 0.33 atmos. pressure of argon. The alloy sample was solutionized in an air furnace at 1100°C for 48h, followed by either a water quench (WQ) or air cooling (AC) to room temperature. The cooling rate in air was measured to be an average 8.5°Cs^{-1} in the range of 1100°C to 500°C and significantly less than 1°Cs^{-1} below 500°C. The water quench rate was estimated to be in excess of 500°Cs^{-1}. Subsequent aging treatments were carried out in a salt bath at 500°C. The time-temperature schedules used for Ti-10V-6Cu samples are given in table 3.1. All the water quenched, air cooled and aged samples were received from Australian Research Council, Center of Excellence for Design in Light Metals, Monash Univerity, Clayton, Australia.

Alloy (wt%)	Sample name	Heat treatment 1			Heat treatment 2			Heat treatment 3		
		Temperature (C)	time	cooling	Temperature (C)	time	Cooling	Temperature (C)	time	Cooling
Ti-18Mo	RQ	1000	30min	RQ	-	-		-	-	-
	30 min	1000	30min	RQ	475	30min	WQ	-	-	-
	48hrs	1000	30min	RQ	475	48hrs	WQ	-	-	-
Ti-20Mo-5Al	WQ	1000	30min	WQ	-	-		-	-	-
	6hrs	1000	30min	WQ	400	6hrs	WQ	-	-	-
	10hrs	1000	30min	WQ	400	10hrs	WQ	-	-	-
	72hrs	1000	30min	WQ	400	72hrs	WQ	-	-	-
	620C 1hr	1000	30min	WQ	400	72hrs	WQ	620	1hr	WQ
	insitu	1000	30min	WQ	400	10hrs	WQ	-	-	-
Ti-10V-6Cu	WQ	1100	48hrs	WQ	-	-	-	-	-	-
	AC	1100	48hrs	AC	-	-	-	-	-	-

Table 3.1: Heat treatment temperature- time schedules. Heat treatment 3 and 2 were done sequentially on the same samples after heat treatment 1.

3.3 Characterization Tools and Software

3.3.1 Mechanical Polishing

All the metallic samples were prepared using metallographic procedures before SEM or FIB inspection. The heat treated alloy samples were machined by Mitsubishi wire electroc discharge machining or Beuhler isomet diamond saw for making smaller representative samples

for electron microscopy analysis. The sectioned samples were mounted in 2" mounts using Beuhler simplimet® 1000 mounting machine with conductive phenolic hot mounting resin. After mounting the samples where polished mechanically on 240, 400, 600, 800 and 1200 grit SiC papers. Subsequently the samples where polished using 1, 0.5, 0.3 and 0.05 microns colloidal alumina solution on velvet sheets from beuhler. After polishing the samples were cleaned in methanol and acetone for 15 minutes using Cole-Parmer sonicator. Subsequently the samples were baked in a hot plate at 200^{o}C for 5 minutes to remove any volatile cleaning solution remnants. There after the samples were either immediately loaded in scanning electron microscope (SEM) or focused ion beam (FIB) for imaging or stored in vacuum desiccators till the time of analysis.

3.3.2 Scanning Electron Microscopes

Two SEMs were used for the analysis. The FEI Nova 230 FEG SEM and Quanta 200 environmental SEM. The FEI Nova SEM has a field emission gun electron column where as Quanta SEM has a tungsten filament based electron column. Both the SEMs are equipped with Everhardt Thornley Secondary electron detectors (ETD), Charge coupled detectors (CCD), detachable solid state back scatter electron detectors (BSED) and SiLi energy dispersive spectrometer detectors (EDS). Genesis software was used for EDS data analysis. Both the SEMs were also equipped with the TSL Digiview III Back scatter electron diffraction detectors (EBSD) with TSL OIM^{TM} software for crystallographic analysis.

3.3.3 Focused Ion Beam

FEI Nova 200 nano lab system with a high resolution field emission gun electron column and a Gallium ion liquid metal ion source (LIMS) focused ion beam column was used for site specific transmission electron microscopy (TEM) and atom probe tomography (APT) sample

preparation. The TEM-APT coupling samples were also made using the same system. The FEI Nova nano lab system is equipped with an Omniprobe Autoprobe^{TM} nano manipulator and gas injection system for depositing Pt. The schematic diagram of the focused ion beam (FIB) system is given in Fig 3.1. The electron beam column is normal to the sample surface and the Ga ion beam column is at an angle of 52^{o} to the sample normal. The details of individual sample preparation techniques will be described below.

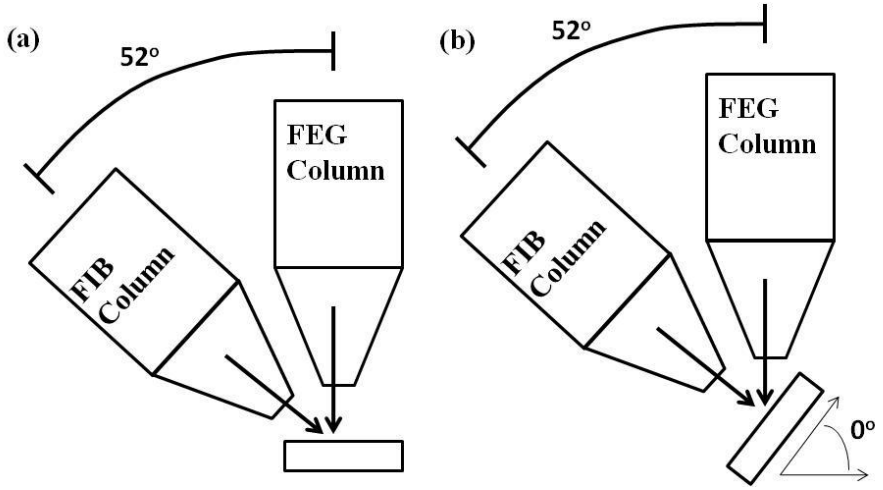

Fig. 3. 1. Schematic diagram of focused ion beam system. (a) Showing the geometry of e beam imaging (b) Showing the geometry for trenching at 52^{o}.

3.3.3.1 Site Specific TEM Sample Preparation

TEM sample preparation using in situ Lift-out procedures are well documented in literature [2, 3]. Electron transparent TEM samples of less than 100nm foil thickness were made using the customized lift-out procedure as described below.

1. The sample was aligned to concentric and eucentric height of the FIB nova nano lab 200 system and obtain a good image of the specific site in the electron beam and ion beam windows.
2. Pt layer of 15 to 20 microns length (x), 1 micron width (y), 100nm thickness (z) was deposited using electron beam patterning.

3. A 500nm thick Pt layer of same x and y dimension as electron beam Pt was deposited using ion beam pattern after tilting the sample to 52 degrees.
4. Two regular cross section trenches of same x dimension as the Pt layer with 3.5 microns y dimension and 8 microns depth was made on either side of the Pt layer with the deepest part of both trenches aligned close to the Pt deposited area.
5. A „U" shaped cut including the undercut, one vertical side of the lamella and partial portion of the opposite vertical side was done at 0^{o} sample tilt.
6. Omniprobe Autoprobe^{TM} needle was inserted and attached to the fully cut vertical side of the lamella by ion beam Pt deposition.
7. The opposite uncut edge was also cut and the Omniprobe nano-manipulator with the attached lift-out sample was moved to Omniprobe TEM lift-out grid
8. The Omniprobe nano-manipulator needle was disconnect after attaching the lift-out lamella on to the side of the TEM grid post.
9. Sample lamella was milled using successively lower currents from 0.5 nano Amps to 50 Pico Amps at 30KV in 48 and 56 degrees tilts alternatively to facilitate a uniform removal of thickness from opposite sides.
10. An electron transparent thickness was attained by final milling at 5KV, 70pico amps current at 48 and 56 degree tilts.

After all the steps given above the Omniprobe TEM lift-out grid with the site specific sample was cleaned in 30 watt argon plasma for 5 minutes before TEM analysis.

3.3.3.2 Site Specific APT Sample Preparation

The quality of the atom probe samples dictate the survivability and success rate of atom probe analysis. Atom probe samples have be in the form of sharp needles with a tip diameter less

than 100nm and slow increase of cross section from the very end of the tip to at least 1 micron depth. Author tried to optimize the normal annular milling procedure already provided in the literature for FIB based sample preparation for atom probe [4]. The procedure given in literature was followed up to attaching the wedge shaped samples on silicon micro tip posts. The optimized annular milling procedure used for subsequent sample preparation is given below.

1. Stage was tilted to 52^{o} and the microtip with attached wedged sample is viewed in the ion beam window with a magnification where the top surface of the wedge takes up about $1/4^{th}$ of the screen display area.
2. The sample was milled to form 1micron diameter cylinder using 1nano amp current, 30 KV ion beam with a circular pattern (1 micron inner diameter, 4 micron outer diameter, 1 micron depth) kept centered at the top surface of wedge sample.
3. The ion beam image was magnified to 80000 times in a way that the top 1 micron diameter region of the sample occupies $1/4^{th}$ of the ion beam window using a 50 pico amp current for viewing.
4. Stream file 3 was used for 30 seconds at 50 pico amp, 30 KV to mill a sharp tip with less than 50nm tip diameter
5. Subsequently the sharp tip was subjected to 1 minute milling using the 5KV 70 pico amps ion beam.

This optimized procedure reduced the time of annular milling to less than 15 minutes per sample and improved the survivability of Ti alloy samples during atom probe analysis.

3.3.3.3 TEM-APT Coupling Sample Preparation

The procedure for making TEM-APT coupling sample was same as FIB based atom probe sample preparation, except the usage of a half cut Cu or Ni TEM grid in place of the

silicon microtip as a sample holder. The half cut Cu/Ni grids can be either in electroliticaly polished form or low thickness slim bar grids that can be FIB milled to form sample posts. Such Cu/Ni grids were kept mounted on a special custom designed TEM-APT coupling holder from Honeywell Scientific throughout the sample preparation, TEM analysis and atom probe analysis. The schematic diagram of a TEM-APT coupling holder is given in Fig 3.2. The individual posts were milled to a 2 micron end diameter on which the wedge shaped samples were attached as per the procedures of APT sample preparation given in 3.4.3.2. The finished samples were in the form of sharp needles with less than 50nm tip diameter. After FIB based sample preparation the grid holder and the grid were plasma cleaned in 30 watt Ar plasma for 4 minutes and loaded on to a special single tilt TEM holder from Honeywell for subsequent TEM analysis. After TEM analysis the sample holder was mounted on an APT sample puck for subsequent APT analysis.

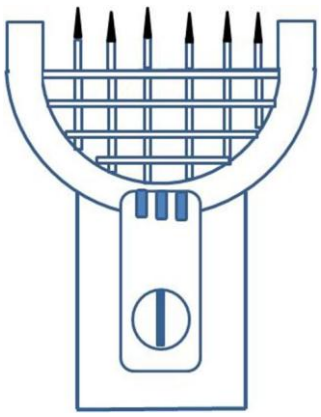

Fig. 3.2. Schematic diagram of a TEM-APT coupling holder.

3.3.4 Transmission Electron Microscope

Transmission electron microscope (TEM) analysis was done on two different TEMs, 200KV FEI Tecnai G^2 F20 S-Twin (S)TEM and FEI Titan^{TM} 80-300. Tecnai is a 200 KV TEM with a high current Shotkey field emitter electron gun with a point to point resolution of 0.24 nm and 0.14nm information limit. The energy spread of the electron gun is 0.7 eV or lesser at 200 KV. The microscope has a Super-Twin objective lens with 1.2mm Chromatic (C_c) and spherical

aberration (C_s) coefficients. Sample holders were capable of going upto $\pm 40^o$ eucentric tilt. It also has a fishione High sensitivity high angle annular dark field (HAADF) detector as an attachment for scanning transmission electron microscopy (STEM) imaging. The high resolution STEM imaging resolution was 0.19nm. It was also equipped with a low system background EDS detector for microanalysis. The fully computer controlled specimen holder permitted usage of a variety of holders from single tilt, double tilt and tomography holders. The basic diffraction, dark field and bright field imaging, STEM, and Energy dispersive spectrometry of samples were done mainly using the FEI Tecnai microscope [5].

Some of the more detailed High resolution TEM and STEM imaging were performed on FEI Titan™ 80-300 microscope. Titan is fitted with a Cs corrector and a monochromator. The Cs correctors are of dual hexapole type and they over compensate the positive Cs of lens system and thereby limit the third order spherical aberration. The chromatic aberration is also reduced by the 300KV Wein filter monochromator resulting in a beam energy spread less than 0.1 eV. Also titan is made with a high speed digital search and view camera replacing the conventional fluorescent viewing screen. The microscope has a 0.2nm point resolution and information limit of 0.07nm. The High resolution STEM (HRSTEM) resolution is 0.13nm. HRSTEM studies are done using the axis Fischione® HAADF STEM detector [6].

Conventional TEM samples were made from 3mm diameter discs punched out of thin foils of the alloy prepared by mechanical polishing. The mechanical polishing of the electric discharge machined (EDM) thin slices of alloy samples were performed using 240, 400, 600, 800 and 1200 grit SiC papers to attain a final thickness of 50-70 μm before punching. The punched 3mm disks of the alloy samples were subjected to dimple grinding on Gatan Dimple Grider™ using 1 μm diamond paste to attain a dimpled region thickness of 20 μm. Subsequently these

dimpled samples were subjected to Ar ion milling in either Gatan Precision Ion polisher (PIPS) or Fishione 1010. Ion milling in Gatan PIPS™ system was done initially using two 5KV Ar ion guns oriented at an angle of 4^{o} from top and bottom surface of the sample followed by a final milling at 2KV at 0.5 degrees from top and bottom of the sample. The milling in Fishione 1010 ion milling unit was performed by using two 5 -2 KV Ar ion beams at angles from 10^{o} to 6^{o}. For TEM samples used to perform aberration corrected HRSTEM and HRTEM imaging an additional low energy milling of the samples were performed in Fishione 1040 nanomill™. In that process a 50-2000V Ar ion beam is selectively rastered on the region of interest facilitating a removal of the amorphous damage that can be caused during high KV milling stages of prior sample preparation steps.

3.3.5 Advanced Photon Source

The Advanced Photon Source (APS) is a national user facility funded by Department of Energy. High brilliance X-rays generated by APS was used for performing the in-situ High energy X-ray Diffraction experiments given in this dissertation [7]. The production of such high brilliance X-rays begin from the electrons emitted from a heated cathode at 1100^{o}C. The electrons are subsequently accelerated to 450 MeV, travelling at 99.999% of speed of light in a linear accelerator before injecting then into a booster synchrotron. In booster synchrotron the electrons are further accelerated by a series of electromagnets to 7 GeV when they will be travelling at a speed greater than 99.999999% of the speed of light. Subsequently these electrons are injected to a 1104m circumference storage ring where these electron beams are bent and focused to a narrow beam travelling in circular path using electromagnets. The storage ring has several straight and curved regions. A series of powerful alternating pole magnets that is inserted in the straight section of the storage ring undulates the electron beams leading to emission of

high brilliance X-rays on a tangential direction of the storage ring. Such devices are known as insertion devices. Such X-ray beams emitted are further collimated and directed to experimental halls in the beam line [7]. The sample analyzed in this work was kept in the beam path of 11IDC beamline in an atmosphere controlled TS1500 Linkam furnace. A schematic diagram of the experimental set up is given in Fig 3.3. The 0.5mm by 0.5mm sized 115KeV X-ray beam passed through a background free window before interacting with sample under study. The diffraction patterns were collected on a Perkin Elmer 2D detector. The time-temperature cycling of TS1500 Linkam furnace and data acquisition was remotely controlled through scripts. The temperature of the furnace was recorded in a time-temperature file and also was remotely monitored through a video camera focused on the temperature controller display. 2D Circular ring diffraction patterns from the sample were recorded in one minute intervals. For better statistics multiple images were integrated during each exposure. After the completion of the heat treatment the integrated images were processed using Fit2D, a 2D data analysis program. Batch processing was used for processing all images at once. Subtraction of spurious peaks from background was done using a standard mask file. Subsequently the data was integrated to generate intensity vs theta plot. The sample to detector distance was kept at 1788.165 mm. The wavelength of the X-ray beam was given as 0.107980 angstroms corresponding to beam energy of 115KeV. The X and Y pixel of the direct beam were given as 1026.583 and 997.0520 respectively. The radial integrated data was sent to output as a bitmap image and a chi file. The theta vs intensity data from chi file was copied and pasted in an Microsoft excel file for further detailed analysis. Subsequently the time evolution of [110] and [200] β peaks and [10-10] and [11-20] α peaks were studies from the selected data files after specific intervals from the beginning of the ageing experiment to end of ageing.

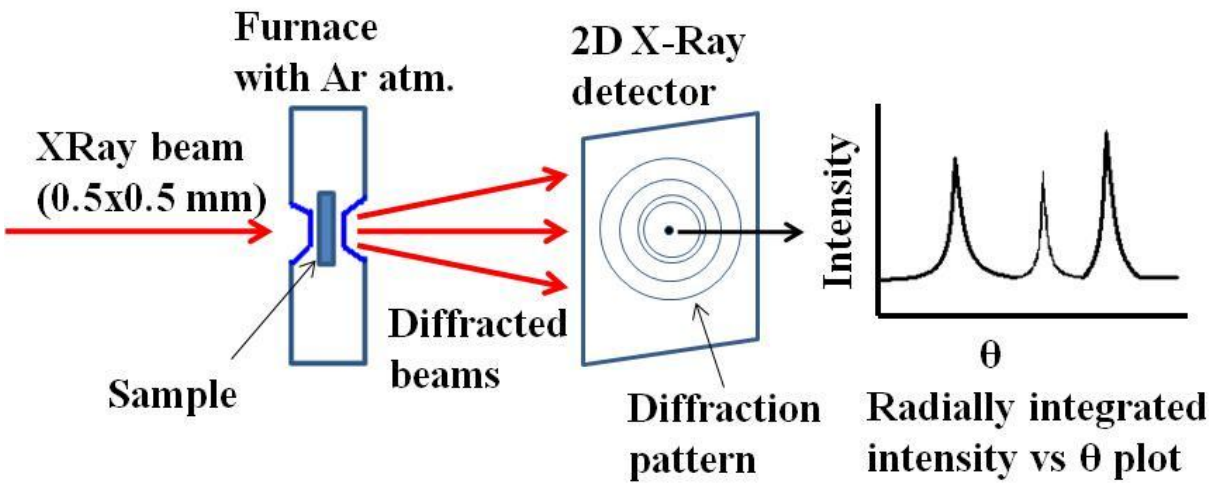

Fig. 3.3 . The experimental set up for in situ High energy X-ray diffraction performed at Advanced Photon Source.

3.3.6 Three Dimensional Atom Probe

A new generation, local electrode atom probe (LEAP^{TM}) 3000X HR three dimensional atom probe tomography (APT) from Imago Scientific Instruments (Now CAMECA) was used for all the analysis presented in the current work. This APT system is equipped with voltage and laser pulsed mode of evaporation. High mass to charge spectrum resolution was able to be attained due to the advanced reflectron lens system. A brief theoretical idea of field evaporation in atom probe tomography will be presented in the following section.

3.3.6.1 Theoretical Background of Atom Probe Analysis

During atom probe analysis, individual atoms from the tip of a sharp needle shaped specimen with less than 100nm tip diameter are field evaporated by application of either a pulsing voltage or a pulsed laser beam in addition to an applied stead state standing voltage across an electrode and the sample. These field evaporated ions are accelerated towards a position sensitive single atom detector. The single atom position sensitive detector is made of a microchannel plate with cross delay line detector. The time of flight of individual ions are recorded from the time difference of the applied pulse to atom detection at the position sensitive

detector [8]. A schematic of the experimental set up for atom probe tomography is given in Fig. 3.4.

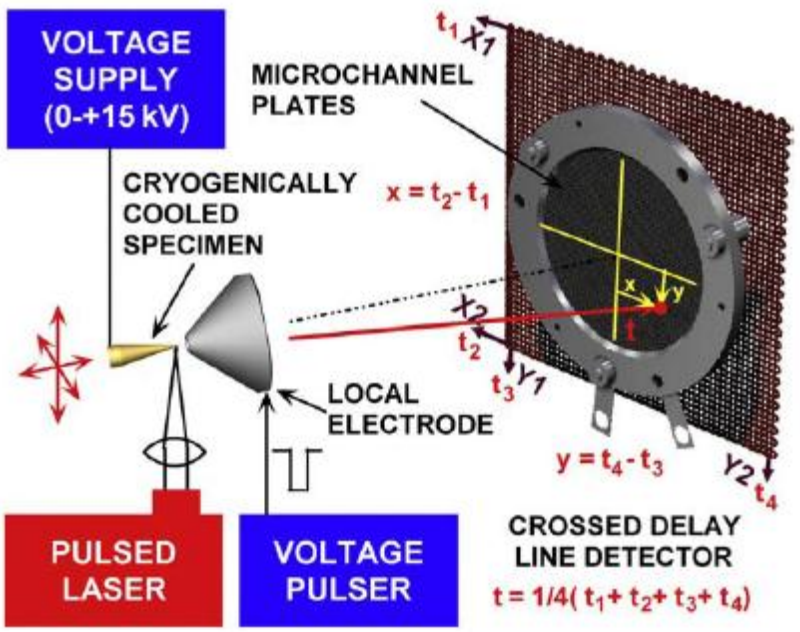

Fig. 3.4. Schematic diagram of a three dimensional atom probe [8].

Field evaporation of the atoms are done by applying about 10-40 V nm^{-1} , which cause to breakage of surface atoms causing an ionization. The initial stage of field evaporation is a thermally activated ion escape over an activation barrier followed by a second stage of post field ionization. From the first stage to second stage the ionic charge can go from 1-3e to ne, where e is a single electron charge. The field emission rate constant (k) can be given by the following equation [8].

$$k = A \exp[-Q(F)/k_b T]$$

Where A is a constant, Q(F) is the activation energy for field evaporation which is a function of applied field (F). T is temperature and k_b is the Boltzmans constant.The field F at which the activation energy Q(F) is zero is known as the zero Q evaporation field. The practical values of Q(F) is slightly greater than zero. The pulsed voltage or laser beam provides the initial

"jump start" required by providing the excess activation energy for start of field evaporation [8]. The field F at the tip of a sample of radius R on application of voltage V is given by

$$F = V/Kr_t$$

K is a numerical constant with a value between 2 to 5. Hence sharper needles cause higher field amplification [9]. Due to this reason individual atom probe sample tips are made to be less than 100nm diameter to attain the evaporation fields required even at lower applied voltages (typically 500V to 11000V) Mass to charge ratio (m/n)of ion can be derived by equating potential energy of ion just before field evaporation (neV) to kinetic energy just after field evaporation ($1/2*mv^2$) to obtain the following relationship [9].

$$\frac{m}{n} = \text{Constant} * V * (\frac{t^2}{d^2})$$

The constant has been estimated as 0.1929796 for V in KVs, time(t) in nano seconds, d in millimeters and m in amu. The time of flight is estimates by the field free drift tube situated between the sample and position sensitive detector called as "time of flight spectrometer". Using the cross delay line detector the x and y coordinates of the ion impact is located. A schematic diagram of a cross delay line detector is given in Fig 4(a). The real atom coordinates on the sample is determined by

$$X = \frac{x}{M}; Y = \frac{y}{M};$$

Where M is magnification given by $(d/\beta r_t)$ where d is specimen to detector distance, β is the image compression factor, and r_t is the tip radius [9]. The image compression factor is a projection parameter with a default value of 1.65. A schematic diagram of the projection geometry is shown in Fig. 3.5 [10].

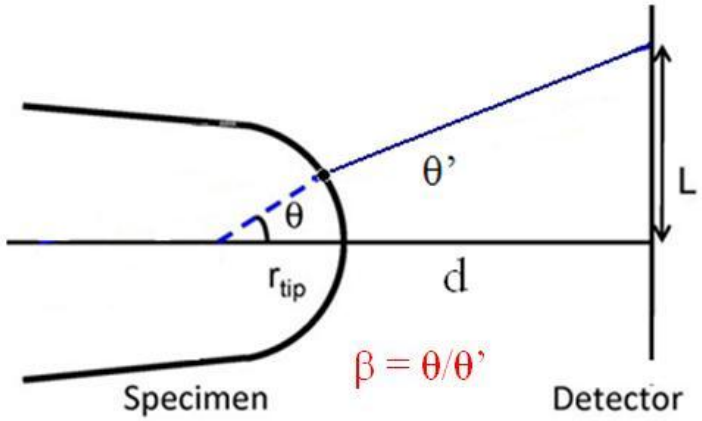

Fig. 3.5. The projection geometry of an atom probe sample [10].

A straight flight path three dimensional atom probe typically has 50-60% detection efficiency due to loss of ions striking the inter-channel space of microchannel plate. The detection efficiency reduces to 37% in a reflectron based high resolution three dimensional atom probe due to additional loss of ions hitting the mesh infront of the reflectron lenses, on entry and exit points[9].

3.3.6.2 Field Compensating Reflectron Lens

The straight flight path APT systems have an energy differential to the applied pulsing voltage. This causes a slight variation in the time of flight for elements because of a spread in the evaporation time of ions within a single pulse. This aberration leads to a reduction of mass to charge spectrum resolution. Hence an energy compensating electromagnetic lens assembly named as a reflectron lens is introduced to improve the mass to charge spectrum resolution [8-10]. The reflectron lens consists of a series of annular ring of electrodes with a reflecting plate at the end that causes the deceleration and reflection of ions from the sample towards the single atom detector. The maximum peak resolution is achieved by maintaining an optimized ratio of the applied voltage (V) and reflectron voltage (V_r) along with a ratio of flight path outside reflectron (d_f) to be four times of the flight path inside reflectron lens (d_r). This energy

compensating reflectron lens makes the time of flight of ions independent of slight variations in energy of pulsing voltage resulting in a higher resolution in mass to charge spectrum [8-10].

3.4 References

[1] Collins PC, Banerjee R, Banerjee S, Fraser HL. Matsc and Engg A 2003;352:118.

[2]Ohnishi T, Koike H, Ishitani T, Tamimatsu S, Umemura K, Kamino T. A New Focused-Ion-Beam Microsampling Technique for TEM Observation of Site-Specific Area's. in:Proceedings of Symposium for Testing and Failure of analysis. Ohio: ASM Materials park, :1999.

[3] Rogers M, Kothleitner G, Berendes A, Bock W, Kolbesen BO. Pract. Metallogr 2005;42:172.

[4] Miller MK, Russel KF, Thompson K, Alvis R, Larson DJ. Microscop. Microanal 2007;13:428.

[5] FEI Tecnai G2 F20 series Product data sheet

[6] FEI TitanTM Product Brochure

[7] http://www.aps.anl.gov/About/APS_Overview/

[8] Miller MK, Forbes RG. Materials characterization 2009;60:461.

[9] Miller MK. Atom probe tomography. New York: Springer publications; 2000.

[10] Emanuelle A. Marquis, Jonathan M Hyde. Material science and engg. R 2010;69:37.

CHAPTER 4
NUCLEATION AND GROWTH OF OMEGA PRECIPITATES IN TITANIUM-MOLYBDENUM ALLOYS

4.1 Introduction

Several attempts have been made in past to experimentally determine the structure of ω-like instabilities that are present in quenched and annealed Titanium and Zirconium based alloys. Chang et al. [1] used high-resolution, single and two beam diffracting, dark-field imaging in a TEM to image the atomic defect rows in Zr-Nb alloys containing 15 and 30 wt% Nb. However only one dimensional information of the ω structure was obtained in this study. Subsequently, Kuan et al. [2] also studied the structure and morphology of ω precipitates in Zr-Nb alloys based on diffraction patterns and dark field images, focusing on a better understanding of the diffuse intensity observed in electron diffraction patterns and the contrast of bright spots appearing in TEM images. More recently, higher resolution images of the ω structure, in as-quenched Ti-14 wt% Mo alloy, were obtained by Sukedai et al. [3] using high resolution transmission electron microscopy (HRTEM), performed with an aberration free focus imaging condition (AFF), coupled with post-processing of images using advanced routines. In the same study, inverse Fourier transform images constructed by using only the diffuse scattered reflections in the Fourier transform patterns along with the transmitted spot, showed the coexistence of regions with ω structure as well as regions with two dimensionally ordered linear defects, similar to that proposed by Kuan et al. [4]. Subsequently, in a detailed work on quenched and aged Ti-11.1at% Mo alloy single crystals, Sukedai etal. compared the HRTEM images obtained in a 400KV microscope with simulated images generated using the multi-slice method as a function of defocus values and position of ω phase crystals in the matrix [5]. In his more recent work, during in-situ annealing of the Ti-15Mo-5Zr alloy in the TEM, the formation of linear arrangements of

bright spots along the <111> β direction was experimentally observed and these were postulated to be embryos of early stages of ω phase [6]. It should be noted that these previously reported HRTEM results [3, 5, 6] were unable to resolve the collapsed atom pairs along [111] direction individually due to the resolution limit of the microscope used. However recent developments in aberration-corrected (C_s corrector for the condenser lens) high resolution scanning transmission electron microscopy (HRSTEM) carried out using a high-angle annular dark field (HAADF) detector permits direct imaging of lattice columns separated by sub-Å distances [7, 8]. Therefore, in the present study, such imaging technique has been used to record the early stages of formation of the ω phase in a binary Ti-Mo alloy. It is well understood that the contrast observed in HAADF-HRSTEM images is incoherent and proportional to the square of the atomic mass [8]. Therefore, the observed contrast in the STEM mode can be qualitatively correlated to differences in the masses of the probed atomic columns, unlike those obtained in the HRTEM mode where phase contrast introduces uncertainties in such an interpretation [9-11]. The comparison between the two techniques would be taken up later in this paper.

There have only been a limited number of previous investigations addressing the composition of ω precipitates in titanium alloys. The relatively refined size scales (usually in the 5 – 50 nm scale) of these precipitates coupled with the limited spatial and compositional resolution of previous generation characterization tools, made it rather difficult to measure their composition accurately. Hence, some of the previous studies attempted to either indirectly determine the ω composition by volume fraction measurements from TEM dark field images [12, 13] or directly measure the composition within limited sampling volumes using one-dimensional atom probe [14]. More recently, the composition and morphology of well-developed

ω precipitates in a binary Ti-Mo alloy have been investigated in detail using atom probe tomography (APT) [15].

The present study couples aberration-corrected high resolution HAADF-STEM and APT to investigate the early stages of ω formation in a binary Ti-9at%Mo alloy as well as the subsequent growth and coarsening of these precipitates on isothermal annealing. One of the salient features presented in this paper is direct experimental evidence of concurrent compositional and structural instabilities within the β phase of a titanium-molybdenum (Ti-Mo) alloy leading to the formation of ω embryos.

4.2 Experimental Procedure

Samples of forged and annealed Ti-9at%Mo (18wt% Mo) alloy were provided by the TIMETAL® company. The as received samples were solution heat-treated in the single β phase field at 1000°C for 30 minutes in a vacuum furnace (~ 1 x 10^{-6} torr) followed by rapid cooling in Ar gas that was introduced into the furnace. The average cooling rate encountered by these samples was ~ 10°C/sec. A few of these quenched samples were subsequently annealed at 475°C for 30 minutes and 48 hours. Subsequently TEM lift-out specimens were prepared for transmission electron microscopy via the FEI Nova Nanolab 200 system. The TEM samples were subjected to low kV cleaning in Fishione 10-40 nanomill to remove the amorphous damage on the surface before analysis. The TEM samples were analyzed in a FEI Tecnai F20-FEG TEM. The FIB was also used to prepare samples for atom probe tomography (APT) studies using procedures discussed in section 3.4.3.2. Subsequently the AP analysis was carried out in a local electrode atom probe (LEAP™) system from Cameca Instruments Inc. The samples studies were carried out in electric-field evaporation mode at a temperature of 70K, with an evaporation rate of 0.2 – 1.0 % and a voltage pulse fraction at 20% of the steady-state applied voltage. Atomic

resolution, Z-contrast, imaging (through High Angle Annular Dark Field (HAADF)-HRSTEM) was performed on a FEI Titan 80-300 microscope, operated at 300 kV, equipped with a CEOS probe aberration corrector.

4.3 Results and Discussion

4.3.1 Investigation of the Nucleation and Growth of ω in Ti-9Mo Using TEM-based Electron Diffraction and Dark-field Imaging

A selected area electron diffraction pattern, recorded along the <011> zone axis of the bcc β phase of the rapidly cooled Ti-9at%Mo alloy is shown in Fig. 4.1(a). In addition to the primary {110} β, {002} β, and {112} β reflections from the bcc matrix, reciprocal lattice streaking (RLS) and secondary intensity maxima are clearly visible in this diffraction pattern at the 1/3 and 2/3 {112} β locations, indicating the presence of ω precipitates in this sample [16]. A dark-field TEM image recorded from one of the secondary intensity maxima (marked by a circle in Fig. 1(a)) is shown in Fig. 4.1(b). Homogeneously distributed, nanoscale precipitates of the ω phase, with an average size <10nm, are clearly visible in this dark-field image. Electron diffraction patterns and corresponding dark-field images from this alloy, after isothermal annealing at 475°C for 0.5 and 48 hrs, are shown in Figs. 4.1(c) – (h). The intensity maxima corresponding to the ω phase, at the 1/3 and 2/3 {112}β locations, have become substantially stronger and more pronounced after isothermal annealing at 475°C for 0.5 hrs, as shown in Fig. 4.1(c). Dark-field images from the reflections marked 1 and 2 in this diffraction pattern, corresponding to two different crystallographic variants of the ω phase, are shown in Figs. 4.1(d) and (e) respectively. The ω precipitates are substantially coarser in these images with an average size ~ 40 nm, based on the two-dimensional measurements afforded by the dark-field TEM images. The orientation relationship between the ω precipitates and the β matrix is {111}β //

{0001}ω and <110>β // <11-20>ω, as commonly suggested in literature [17]. Longer periods of isothermal annealing for 48 hrs at 475°C leads to further growth and coarsening of the ω precipitates, as clearly shown in the dark-field images in Figs. 4.1(g) and (h). The corresponding electron diffraction pattern after 475°C/48hrs annealing is shown in Fig. 4.1(f) with the specific ω spots used for recording the dark-field images marked as 1 and 2. The average size of the ω precipitates after 475°C/48hrs annealing is ~ 80 nm.

4.3.2 High Resolution Characterization of Rapidly Cooled Ti-9Mo

High resolution microscopy was conducted in rapidly cooled Ti-9at%Mo alloy in order to determine the atomic-scale rearrangements or shift in the atomic columns required to nucleate ω embryos within the β matrix. Fig. 4.2(a) shows an HRTEM image, obtained in Tecnai F20-FEG TEM, taken along the <110>β zone axis. The top right region in this image represents a pure β phase where the (002) and (1-10) β atomic planes are clearly visible (perpendicular to the corresponding directions, as marked by arrows). However the region at the bottom left of the same Fig. 4.2(a) is not very clear and the blurryness in the atomic columns does indicate a definite departure from pure β structure. In fact such blurryness can be associated with shift of atoms along opposite <111> β directions, in order to form ω within the β matrix [3, 5, 6]. Although the rectangular box drawn in this ω-transformed region helps in identifying the ω motif, it is evident that the shift in the atomic columns is not very clearly resolved in this region. This is probably due to the fact that the probed region in the HRTEM mode encompasses the ω particle along with the β matrix present either above or below it, which convolutes the interpretation of exit wave intensities. This is all the more confusing considering the fact that HRTEM images are not directly interpretable as they are essentially generated due to interference effect of mutiple waves that interact with the crystal potential. Such phase contrast

images are thus dependent on several microscope related factors such as defocus value and spherical aberration coefficient, as well as on specimen dependent parameters such as overall sample thickness, and size and position of ω particle.

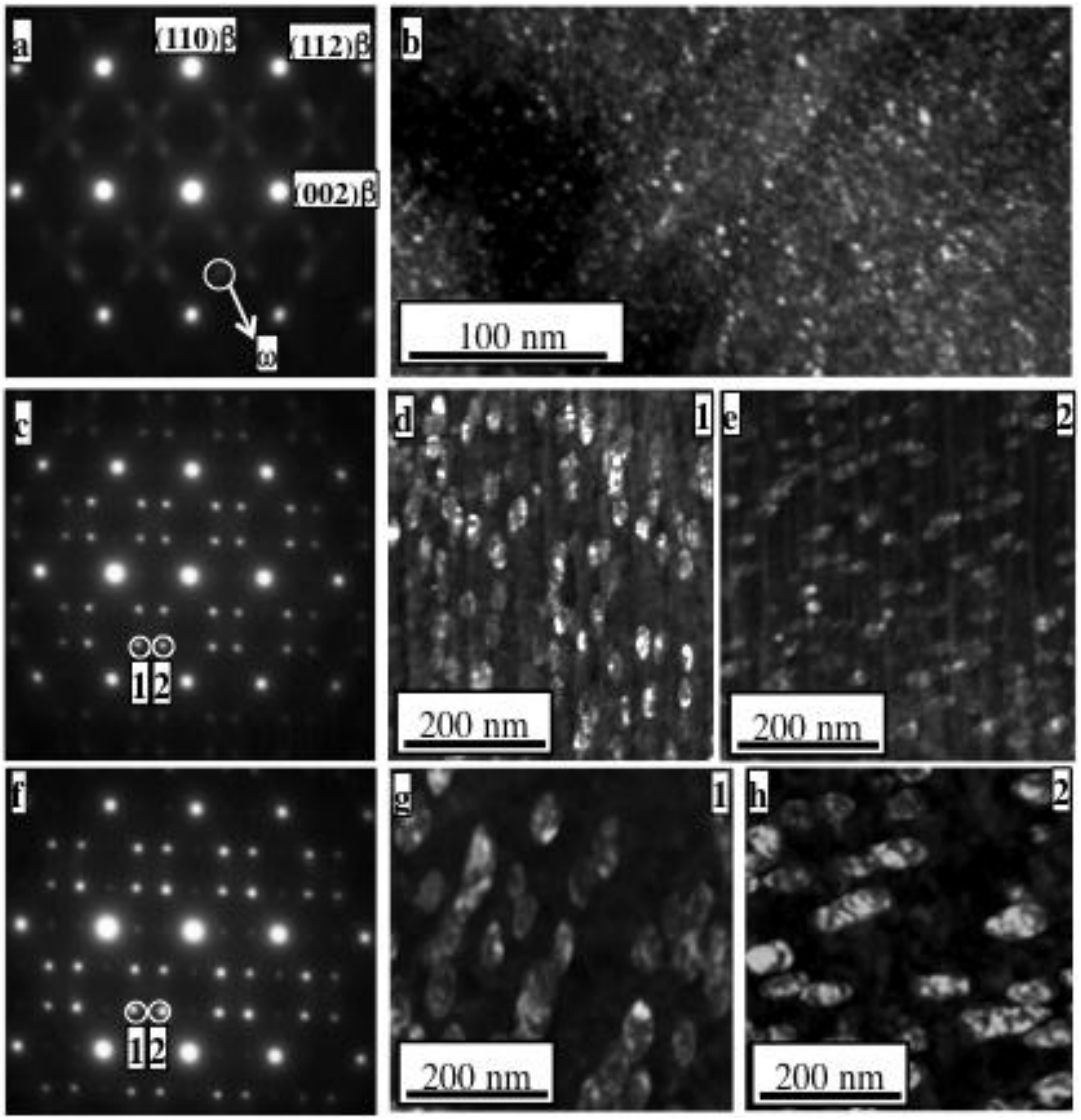

Fig. 4.1(a) shows the SAD pattern of <011>β zone axis with ω reflections at 1/3 and 2/3 {112}β positions of rapid cooled Ti-9Mo. (b) Dark field image formed using the ω reflection shown by the circle in Fig. 1(a). (c) shows the SAD pattern of <011>β zone axis with sharper ω reflections at 1/3 and 2/3 {112}β positions for the 475C 30 minutes aged Ti-9Mo.(d), (e) Dark field image formed using ω reflections marked 1 and 2 in Fig.1(c) showing fully developed ω structure within the β matrix. (f) shows the SAD pattern of <011>β zone axis with sharper ω reflections at 1/3 and 2/3 {112}β positions and double diffractions spots for the 475C 48hrs aged Ti-9Mo. (g), (h) Dark field image formed using ω reflections marked 1 and 2 in Fig.4.1(f).

In fact, as mentioned earlier, Sukedai et al. in one of his studies did conduct multislice calculations to simulate the effect of defocus value and position of omega phase crystals within the beta matrix [5]. The results in few of the cases match very closely to the experimental observations as shown in Fig. 4.2(a), where the doublet of atoms within the ω motif is difficult to resolve.

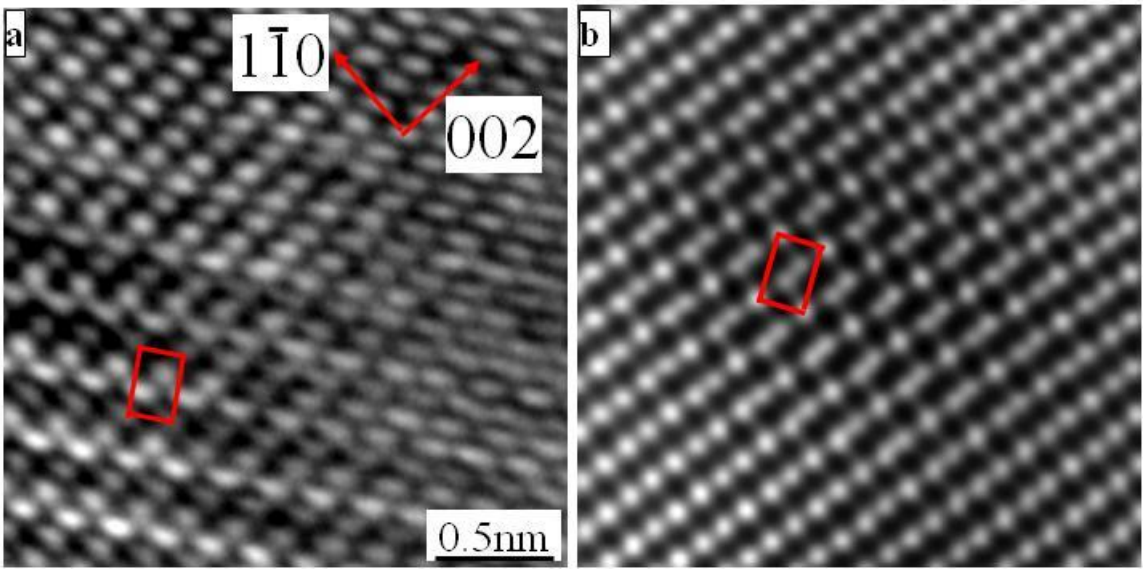

Fig. 4.2 (a) HRTEM image of rapidly cooled Ti-9Mo recorded along <110>β zone axis showing the β and ω regions. (b) HAADF-HRSTEM image of the same sample recorded along <110>β zone axis.

The ω regions identified by the displaced atomic columns are much more distinguishable in (b). In contrast, the high-resolution HAADF-HRSTEM image recorded along the same <110> axis of the β matrix (Fig. 4.2(b)), highlighting a different ω transformed region of the rapidly cooled Ti-9at%Mo alloy, can be directly interpreted. This is because the column intensities of the incoherent image obtained in the STEM mode is dependent solely on overall atomic mass (Z) of the probed column and not on the phase contrast generated by interfering waves [7]. Also the highly reduced TEM foil thicknesses (~ 10 nm) coupled with the fact that the HAADF-STEM information is only confined to the top ~ 5 nm of the sample, substantially reduces the influence

of sample thickness on these contrast features, consequently making the interpretation in terms of atomic mass differences more reliable**.** Thus even though Figs. 4.2(a) and (b) are of similar magnification, the shift in atomic columns resulting in the ω structure is much more clearly distinguishable and discernable in case of the HRSTEM image shown in Fig. 2(b).

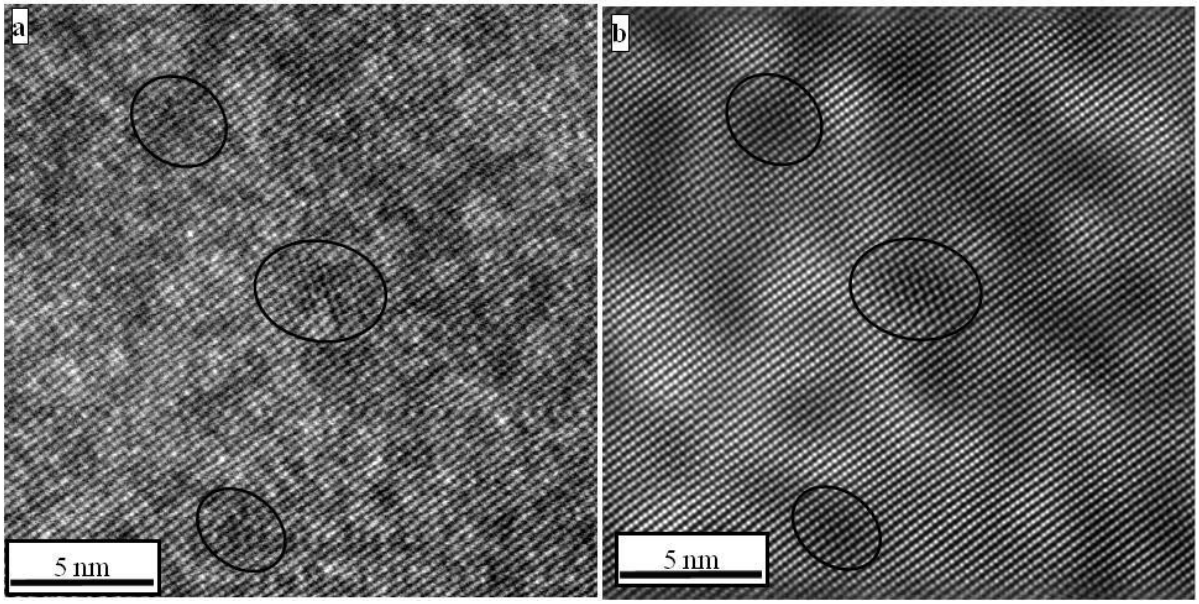

Fig. 4.3(a) HAADF-HRSTEM image of rapidly cooled Ti-9Mo recorded along <110>β zone axis showing the atomic columns within the bcc matrix as well as marked regions corresponding to the ω embryos. (b) Fourier filtered HAADF-HRSTEM image corresponding to the same region showing the dark and bright contrast pockets.

A relatively lower magnification high-resolution HAADF-STEM image (Fig. 4.3(a)), recorded under similar condition as in Fig. 4.2(a), exhibits regions of relatively brighter and darker contrast indicative of differences in atomic masses between these regions (Z-contrast). The contrast between the darker and lighter pockets is more clearly visible in the background-subtracted (Fourier-filtered) HAADF-STEM image shown in Fig. 4.3(b), that corresponds exactly to the one shown in Fig. 4.3(a). Three specific regions exhibiting a darker contrast (lower atomic mass) have been marked in both Figs. 4.3(a) and (b). These darker regions clearly exhibit shifts in the atomic columns with respect to the parent β matrix structure and are likely to be

nanoscale embryos of the ω phase. While the contrast variations observed in these HAADF-STEM images are indicative of compositional partitioning (differences in Ti and Mo contents) within the β phase, it is rather difficult to conclusively establish such a difference purely based on the contrast in these images. Therefore, APT studies have been carried out on the same rapidly cooled Ti-9Mo sample, the results of which have been summarized in Fig. 4.4. Fig. 4.4(a) shows an atom probe reconstruction from this sample, exhibiting the Ti atoms in blue and the Mo atoms in red. Based on the raw data presented in this reconstruction of 2.1 million atoms, it is not possible to resolve any compositional partitioning. However a statistically relevant measurement of the compositional partitioning in this sample has been calculated using the proximity histogram (or proxigram) methodology [18]. For this purpose, initially the Ti-rich regions have been delineated by computing an iso-concentration surface (will be referred in short as iso-surface subsequently) for Ti = 92 at%. Subsequently the compositional partitioning across this iso-surface interface has been calculated and plotted as a proximity histogram of Mo content, as shown in Fig. 4.4(b). This proxigram clearly shows that there is Mo partitioning across this interface with 5.5 ± 0.11at% and 10.5 ± 0.47at% Mo in the solute-depleted and solute-rich regions respectively. The corresponding Ti iso-surface is shown as an inset in the same Fig. The chemical clustering tendency (preferential formation of Ti-Ti versus Ti-Mo bonds) in the rapidly cooled Ti-9Mo alloy, can also be represented using an analysis procedure, similar to a radial distribution function (RDF) of the atom probe data [19, 20], as shown in Fig. 4.4(c). Though this representation lacks the spatial resolution of RDF analysis carried out using other techniques such as synchrotron-based extended X-ray absorption fine structure (EXAFS), it is still a useful representation to show relative clustering or ordering tendencies within solid-solutions. Fig. 4.4(c) shows the radial distribution function (RDF) for the β phase obtained by plotting the bulk-

normalized concentration as a function of distance from the Ti center. The solid curve corresponds to Ti-Ti bonds and the dashed one to Ti-Mo bonds, with a value of one for the normalized concentration corresponding to a perfectly random solid solution [19, 20]. Evidently, there are a higher number of Ti-Ti bonds as compared to Ti-Mo bonds within a radial distance of ~2 nm from the Ti center (more apparent in the magnified view shown as an inset in Fig. 3(d)). Thus, the RDF curves corroborate the phase separation within the β matrix resulting in the formation of ~ 4 nm Ti-rich pockets, which is in excellent agreement with the size of the pockets of darker contrast (lower atomic mass) clearly visible in the HAADF-HRSTEM image shown in Figs. 4.3(a) and (b).

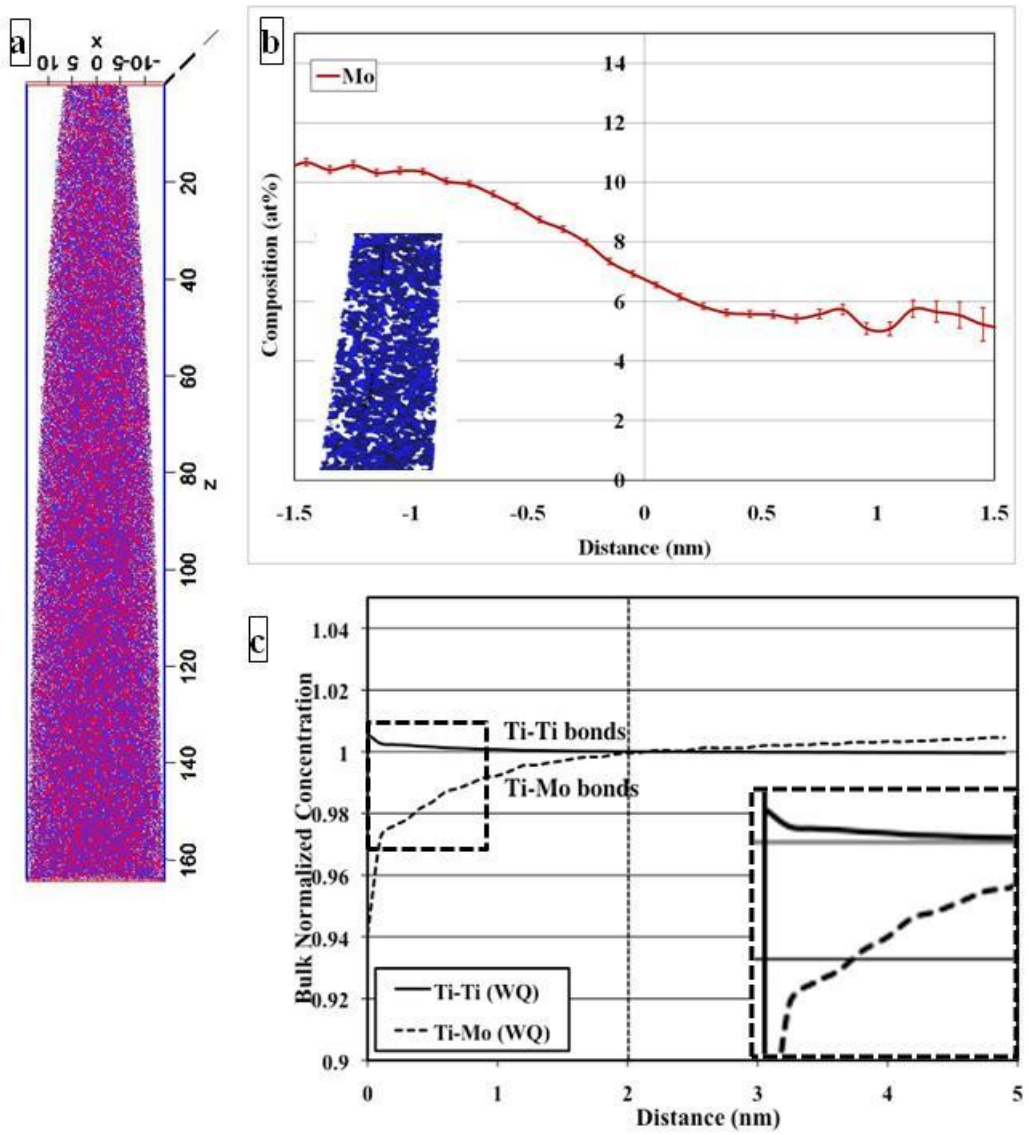

Fig. 4.4(a) APT atomic reconstruction of rapidly cooled Ti-9Mo alloy showing Ti atoms in blue and Mo atoms in red. (b) Proximity histogram for Mo showing the Mo partitioning across a 92% Ti iso concentration surface. The 92% Ti isoconcentration surface view given as an inset. (c) Radial distribution function (RDF) for the beta phase from a Ti center. Solid curve corresponds to Ti-Ti bonds and dashed line corresponds to Ti-Mo bonds. A zoomed image of the dashed square is given as an inset for cleared representation of predominance of Ti-Ti bonds over Ti-Mo bonds.

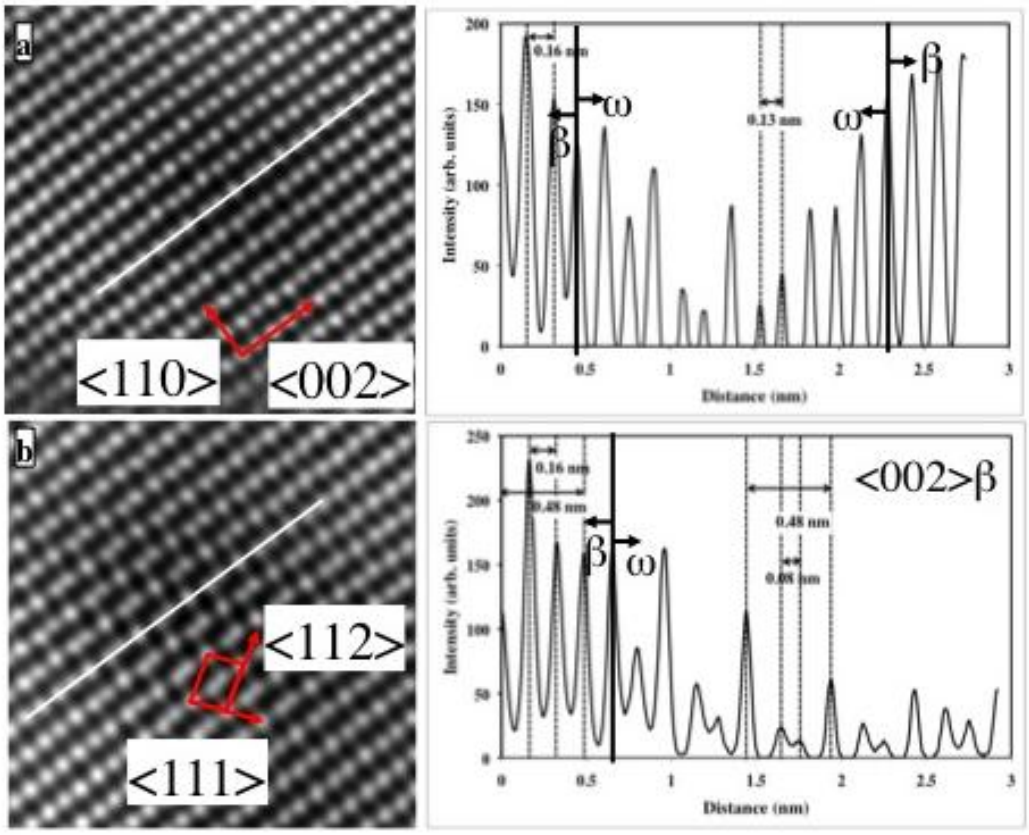

Fig. 4.5(a) and (b) Enlarged HAADF-HRSTEM images of rapidly cooled Ti-9Mo sample showing two specific ω embryos which exhibit distinctly different stages of collapse of the {111} planes of the bcc (β) matrix. The atomic displacements was calculated using an intensity profile along <002> direction marked by the white lines in (a) and (b). The intensity profile given on right shows only very small degree of displacement of atomic planes in (a) but a substantially larger and yet partial collapse is seen in (b).

Enlarged HAADF-HRSTEM images of two specific ω embryos are shown in Figs. 4.5(a) and (b). They capture two distinctly different stages of collapse of the {111} planes of the bcc (β) matrix within these embryos. Thus, while Fig. 4.5(a) shows an early stage of ω formation with only a very small degree of displacement of the atomic planes, Fig. 4.5(b) exhibits a much more advanced stage of ω formation with a substantially larger degree of plane collapse. Nevertheless, in both these cases, the collapse is only partial. A simple way to compare the relative displacements of the atomic columns in both cases is by plotting intensity profiles along the

<002> directions, marked by the white lines on Figs. 5(a) and (b). Thus, in case of Fig. 4.5(a), while the distance between adjacent {002} planes in the β region is 0.16 nm (equal to the expected interplanar spacing based on a lattice parameter of 0.32 nm), within the embryonic ω region the spacing between every first and fourth column equals 0.16 x 3 = 0.48 nm, but the spacing between the second and third columns is only 0.13 nm. This indicates that the projected distance between the second and third atomic columns reduces due to the initiation of collapse of the atomic planes. In case of Fig. 4.5(b), the same analysis reveals that within the embryonic ω region, the projected distance between the second and third atomic columns reduces to 0.08 nm indicating a larger degree of collapse as compared with the region shown in Fig. 4.4(a). Even though this measurement gives us an overall idea of the degree of collapse of the atomic planes, it has to mentioned that the calculation along the <002> direction is just a projection of the actual <111> displacement of the atoms (refer to the directions marked in Figs. 4.5(a) and (b)). Thus, even though displacement along <002> direction is easier to understand, for a more quantitative analysis of the extent of collapse within these ω embryos, it is necessary to measure the collapse of the {111} planes or the displacement of atomic columns along the <111> direction.

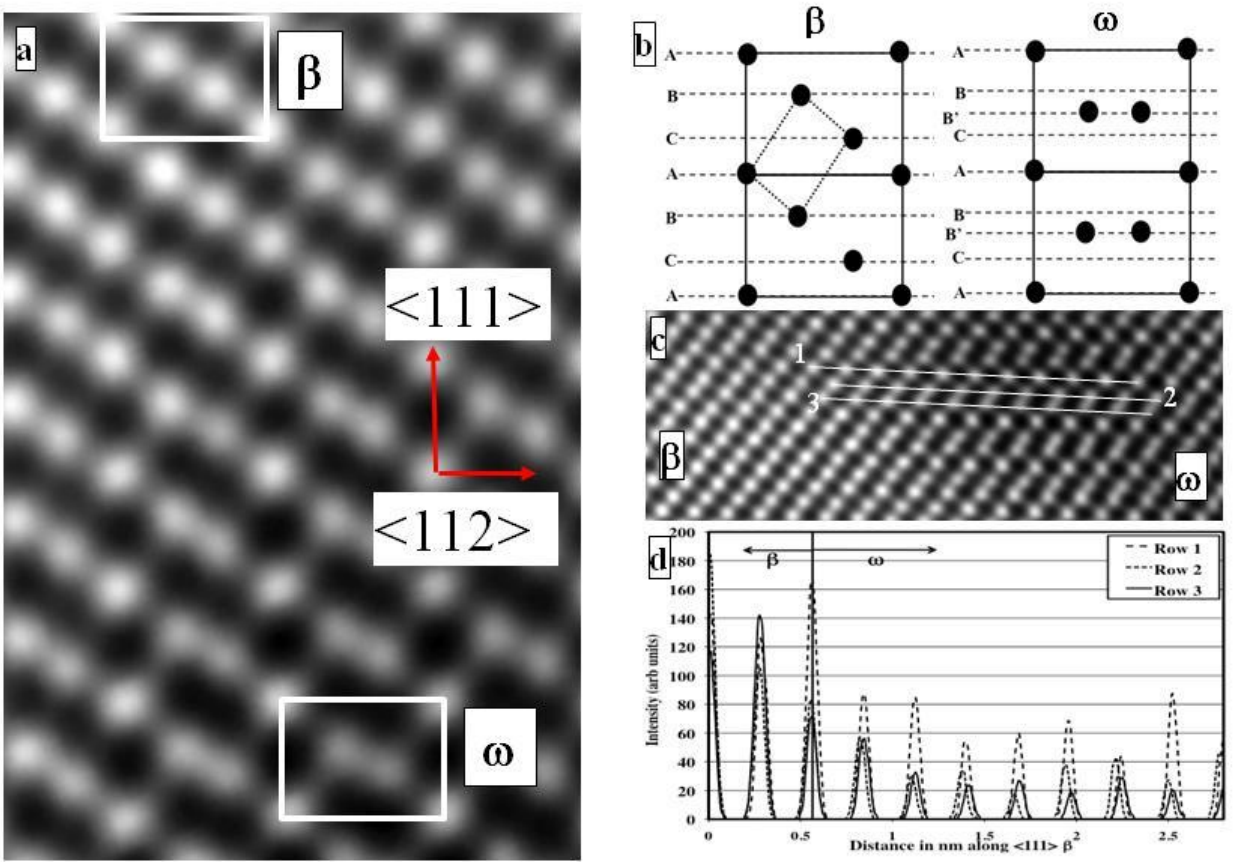

Fig. 4.6(a) Enlarged HAADF-HRSTEM image showing the transition from untransformed β structure on top to the transformed ω like structure in the bottom side of the image. The motif of β and ω are highlighted with white rectangles. (b) Shows the schematic Figs. for the ideal motif of β and ω. The ABCABC stacking of 222 planes in the β and AB‟AB‟ stacking in the transformed ω structures are highlighted. (c) Shows the HAADF-HRSTEM image showing the ω nuclei previously shown in Fig. 4 (b) with 3 parallel <111> directions marked as 1, 2 and 3. The origins of each row are transposed to overlap. (d) The intensity profile along the three parallel <111> directions going from β to ω nuclei showing the displacement of atomic columns.

An enlarged view of the ω embryo in Fig. 4.5(b) is shown in Fig. 4.6(a) with the super cell or motif corresponding to the untransformed β structure shown at the top of the HAADF-STEM image and the partially transformed ω-like structure shown at the bottom. For convenience the image has been rotated such that the <111> (direction of collapse of atomic columns) and <112> vectors lie parallel to the orthogonal axes bounded by the Fig. Also for reference, the ideal motifs corresponding to the β and ω phases have been shown in the schematic Figs. in Fig. 4.6(b). To

quantify the atomic displacements within the ω region with respect to the β matrix, the column intensities along rows 1, 2, and, 3 (marked in the low magnification HAADF-HRSTEM image in Fig. 4.6(c)) have been plotted as a function of distance along the <111>β direction in Fig. 4.6(d). Again for simplicity, the origin for each row has been transposed to overlap, and moving along the distance axis from left to right, the structure transitions from β to ω-like. The atomic spacing between adjacent atomic columns along row 1 is $3d_{222}$ where d_{222} is the inter-planar spacing between the {222} planes of the bcc structure. The ordered collapse of the {111} planes leading to the β to ω transformation can be described as a displacement wave with a wavelength $\lambda = 3d_{222}$ with the corresponding wave vector being 2/3 <111>* (reciprocal space) [21, 22]. Based on this formalism, complete β to ω transformation will correspond to a longitudinal displacement wave with an amplitude equaling $0.5d_{222}$. With reference to Fig. 4.6(c), such a complete transformation would require a displacement of the atoms in row 2 to the left, and those in row 3 to the right, by $0.5d_{222}$, while the row 1 remains stationary. Consequently, the partial collapse of the {111} planes, observed in the present case, indicates smaller amplitude of the displacement wave as compared to that required for full collapse. Based on the plot shown in Fig. 4.6(d), the displacements for the atoms in rows 2 and 3 have been calculated as a fraction of d_{222} and the values were found to lie in the range $0.16d_{222}$ to $0.2d_{222}$, progressively increasing moving from left to right along the distance axis corresponding to Fig. 4.6(c) (from β to ω region).

4.3.3 Growth of ω in Ti-9Mo after Isothermal Annealing at 475°C for 0.5 Hours

The fully developed ω structure is clearly visible in case of the same Ti-9at%Mo sample, that was isothermally annealed for 30 minutes at 475°C, as evidenced by both the dark-field TEM images shown in Figs. 4.1(d) and (e), as well as the high-resolution TEM image as shown in Fig. 4.7(a). The structurally-sharp β/ω interface, viewed along the <110>β // <11-20>ω

direction, can be clearly seen at atomic resolution in this image. Interestingly, distinct ledges, as marked via straight lines, are visible at this interface. The dimensions of these ledges appear to be ~ 1 nm and since the ω precipitates are fully coherent with the β matrix, these ledges are likely to be growth ledges [23]**.** However, a detailed crystallographic analysis of these ledges has not yet been carried out. An atom probe reconstruction of this sample, with the Ti-rich regions revealed by plotting a 92at% Ti iso-concentration surface together with Mo atoms in red, is shown in Fig. 4.7(b). Ellipsoidal-shaped ω precipitates of different sizes and orientations, similar to those reported by Blackburn et al. [13], are clearly visible in this reconstruction. The compositional partitioning across the β/ω interface was determined via a proximity histogram (proxygram) analysis of interfaces created from a 92at% Ti iso-concentration surface. The Mo proxigram plotted in Fig. 4.7(c) was calculated by averaging across ten ω precipitates with a bin size of 0.1 nm [18]. The large difference between the Mo contents of the β and the ω regions in this image indicates a substantial rejection of Mo from the growing ω precipitates during isothermal annealing at 475°C. The average Mo content on the β side in this case is ~ 12 at% while that on the ω side is ~ 4 at%. Therefore, the growth of the ω precipitates has resulted in enhanced partitioning of Mo between the β and ω phases as compared to the as rapidly cooled condition.

After the isothermal annealing treatment at 475°C for 0.5 hours the ω precipitates are not only coarser, but also exhibit a complete collapse of the {111}β planes. This is more clearly visible in the magnified view of the high-resolution TEM image, shown in Fig. 4.8(a). The displacements of the atomic columns have been analyzed in a manner similar to that described previously in case of Fig. 6(d) for the partially transformed ω embryos. Fig. 4.8(b) shows a plot of the atomic column intensity as a function of distance along the <111>β axis, and the

corresponding displacements were calculated to lie in the range $0.27d_{222}$ to $0.5d_{222}$, which would indicate a complete collapse of the {111}β planes.

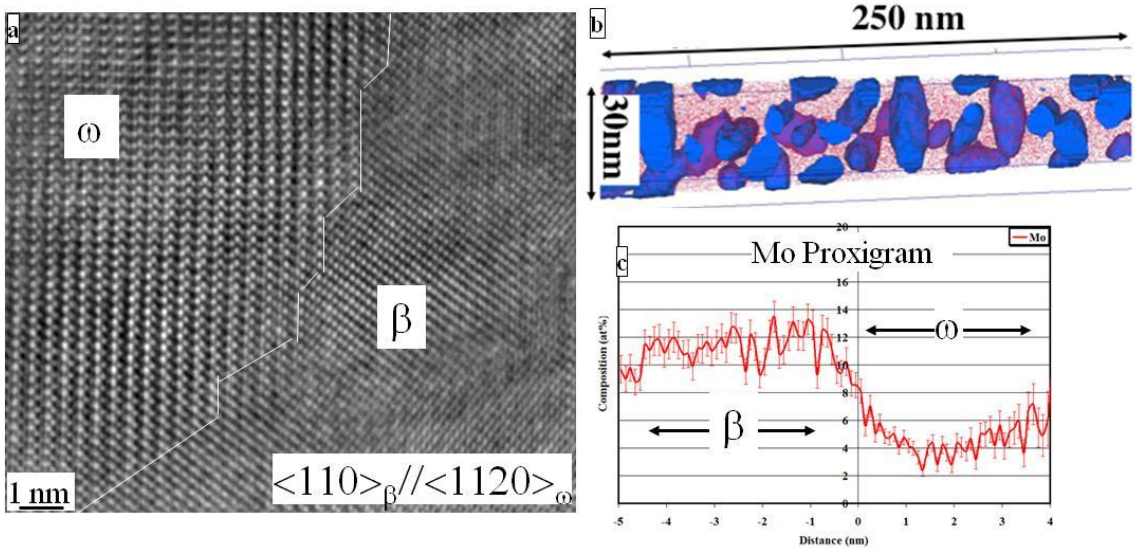

Fig. 4.7(a) HRTEM image recorded along <011>β zone axis showing the interface between a well developed ω region and β matrix [23]. The ledges at the interfaces are marked with white lines. (b) An atom probe reconstruction of Ti-9Mo 475C 30min aged sample revealing the Ti enriched region by a 92% iso-concentration surface with Mo atoms in red (c) Mo proximity histogram plotted across the 92% Ti iso-concentration surface revealing the Mo portioning between the Mo depleted ω and Mo rich β phase.

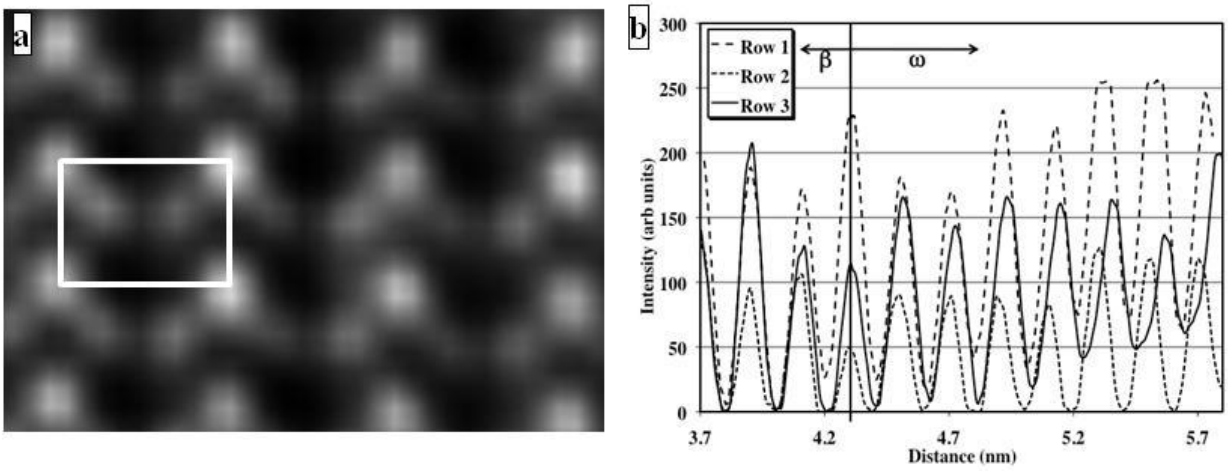

Fig. 4.8(a) Enlarged HRTEM image showing the complete collapse of atomic planes in ω precipitates of Ti-9Mo aged for 30 minutes at 475C with the white rectangle showing the final ω motif. (b) The intensity profile along 3 parallel <111> directions going from β on the left to ω in right with a collapse extent varying from 0.27 d222 to 0.5 d222 in the core of ω.

4.3.4 Growth of ω in Ti-9Mo after Isothermal Annealing at 475°C for 48 Hours

Prolonged isothermal annealing of the Ti-9at%Mo for 48 hours at 475°C results in further growth of the ω precipitates as clearly shown in both the dark-field images in Figs. 4.1(g) and (h), as well as in the atom probe reconstructions shown in Figs. 4.9(a) and (b). Fig. 4.9(a) shows a basic 3D rendition of both Ti (blue) and Mo (red) ions reconstructed from the atom probe data. The Ti-rich ω precipitates are clearly visible in this 3D rendition [23]. An iso-surface corresponding to Ti=92at% has been plotted in Fig. 4.9(b), clearly demarcating the interfaces between the ω precipitates and the β matrix. The corresponding Mo proximity histogram, averaged across all the β/ω interfaces shown in Fig. 4.9(b), is plotted in Fig. 4.9(c) together with the corresponding statistical error bars. Based on the compositional profile shown in Fig. 4.9(c) it can be concluded that after annealing for 48 hours at 475°C, there is more pronounced partitioning of Mo between the β (~13at% Mo) and ω (~2at% Mo) phases, as compared with the 30 minutes annealed condition at 475°C [23]. Thus it is evident that the growth and coarsening of the ω precipitates is coupled with the compositional partitioning of Mo, which diffuses out of these precipitates into the surrounding β matrix.

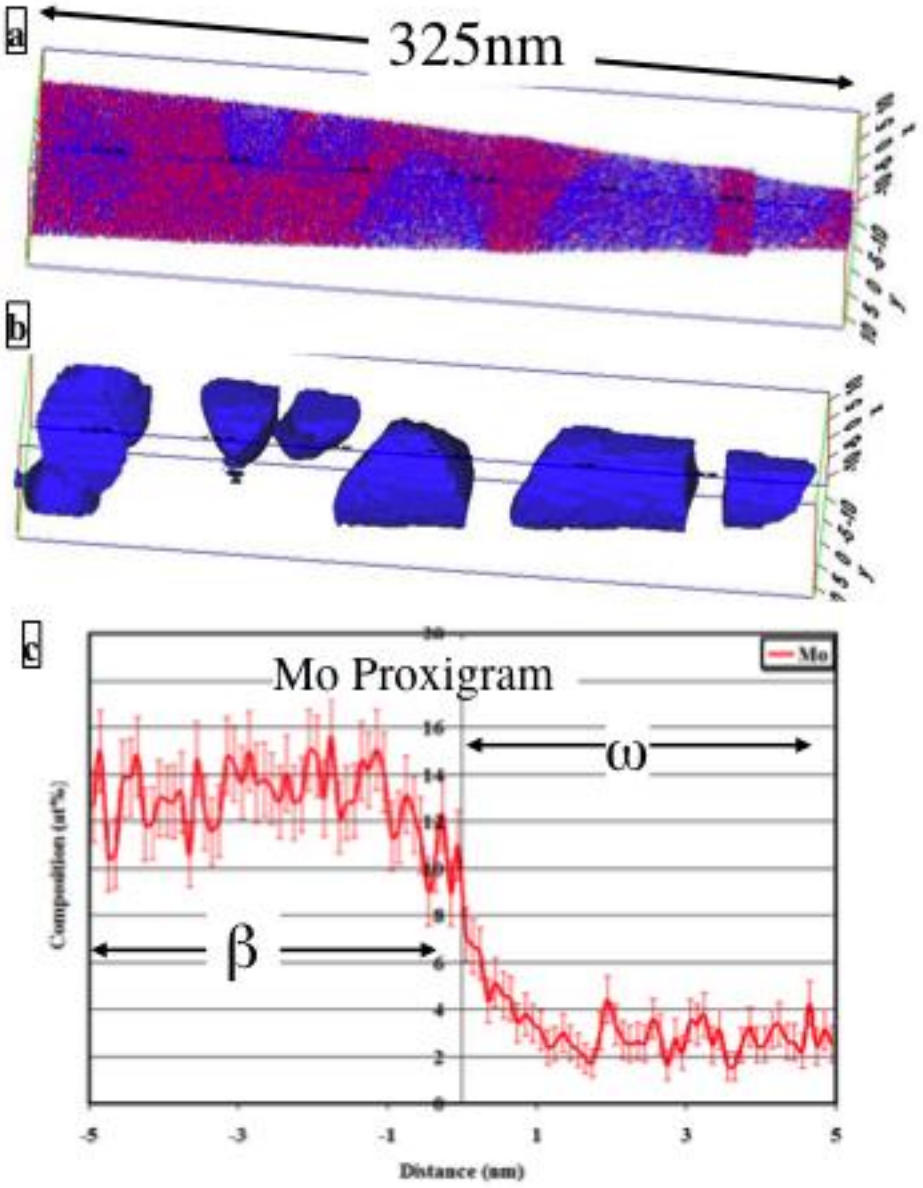

Fig. 4.9(a) An atom probe reconstruction of Ti-9Mo aged for 48hrs at 475 C, with Ti atoms in blue and Mo atoms in red showing the well developed ω precipitates. (b) Ti enriched regions highlighted by 92% Ti iso-concentration surface. (c)The Mo proximity histogram using Ti=92 at% iso-concentration surface showing more pronounced partitioning of Mo between β and ω phases in comparison to Fig 4.6(c) [23].

Fig. 4.10 shows a compilation of the radial distribution functions (RDF) for all three heat-treated conditions of the Ti-9Mo alloy, as-cooled (solid lines), annealed at 475ºC for 30 minutes (dotted lines), and annealed at 475ºC for 48 hours (dashed lines), obtained by plotting the bulk-

normalized concentration as a function of distance from the Ti center. The progressively increasing Ti-Ti clustering within the alloy (as observed from the radial distance up to which the normalized value of Ti-Mo bonds become equal to one, as for a random solid solution) is clearly visible as a function of increasing annealing time at 475°C. The rapidly decreasing number of Ti-Mo bonds indicates the rejection of Mo from the growing and coarsening ω precipitates in the alloy.

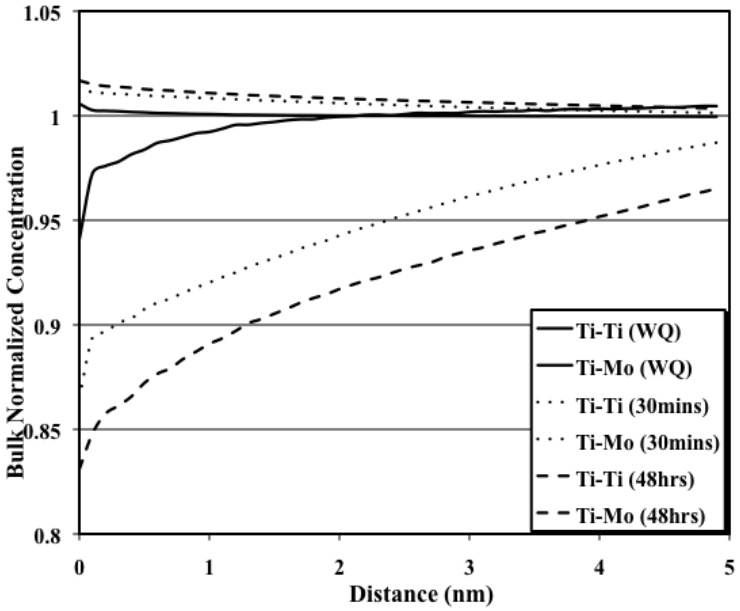

Fig. 4.10 A compilation of radial distribution functions (RDF) of all the heat treatments of the Ti-9Mo alloy, plotting the bulk normalized concentration from a Ti center. The rapidly cooled condition is shown in solid lines, 475^{o}C 30 minutes in dotted lines and 475^{o}C 48hrs in dashed lines.

4.3.5 Mechanism of ω Nucleation and Growth in Ti-9Mo

Based on these experimental observations a mechanism for the formation for embryonic ω within the bcc β matrix can be proposed. Thus, during rapid cooling of the Ti-Mo alloy from the high temperature single β phase field by forced argon cooling, the compositional instability within the bcc matrix manifests itself via compositional clustering (phase separation) into nano-scale Mo-enriched and Mo-depleted regions. This is evident from the HAADF-HRSTEM image

showing the high Z and low Z pockets, that can be associated with increased and depleted regions of Mo respectively (in Figs. 4.3(a) and (b)). Also atom probe iso-concentration surface measurements provide a quantitative value of these clustering tendencies (Fig. 4.4(c)), which presumably occurs via a second order spinodal decomposition process. Subsequently, a structural instability manifests within the Mo-depleted regions, where it is energetically favorable, resulting in initiation of collapse of the {111} bcc planes forming embryonic ω regions. Chapter 5 explains the first principle electronic structure based calculations conducted to determine the increased likelihood (or driving force) for such displacive transformation to occur in Mo depleted regions. The thermodynamic basis for this mechanism can be simply illustrated using a set of schematic free energy versus composition (Mo content) plots for the β and ω phases at lower temperatures (larger undercoolings), as shown in Fig. 4.11. An undercooled alloy of composition Ti-9at%Mo presumably has a free energy lying within the miscibility gap (also within the spinodal) of the β phase, and consequently is unstable to compositional fluctuations. As these compositional fluctuations grow in amplitude and wavelength, eventually the solute (Mo) depleted regions within the β phase cross the T_0(c) point of intersection of the β and ω free energy curves. These solute-depleted regions now become metastable (or unstable) with respect to the structural instability causing the partial collapse of the {111} β planes leading to the formation of ω embryos. It should be noted that while the initiation of collapse of {111} β planes takes place within the embryonic ω regions, the extent of this collapse does not reach completion (=0.5 d_{222}), as was evident from the atomic displacement measurements in Fig. 4.6(d). Additionally, the composition of these embryonic ω regions is also far-from equilibrium and they contain an excess amount of Mo (refer Fig. 4.4(c)). More detailed analysis of the correlation between the extent of displacive collapse and the composition of the solute-depleted regions in

Ti-Mo alloys carried out using first-principles electronic structure based calculations are provided in the next chapter.

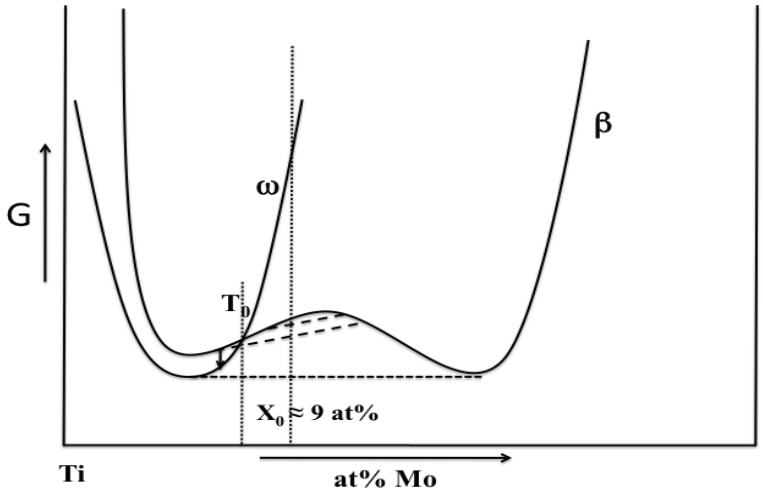

Fig. 4.11 Schematic free energy versus composition plots for the β and ω phases in Ti-9Mo alloy under lower temperatures that illustrate the transformation mechanism. A miscibility gap is shown in β free energy curve and the average alloy composition is marked by the vertical dotted line. The T_0 point where the β and ω free energy curves intersect is also marked in the Fig. The sequential phase separation in β and subsequent structural transformation of Mo depleted β regions to βω are shown in the Fig. using dashed lines and arrow.

Isothermal annealing of the Ti-9Mo alloy at 475°C leads to growth of the embryonic ω regions (as observed in Fig. 4.1) accompanied with two major changes; increase in the extent of collapse of {111}β planes to completion (= 0.5 d_{222}) leading to the fully-developed structure of the ω phase (Fig. 4.8(b)) and rejection of Mo from the growing ω precipitates (Fig. 4.7(c)). After annealing at 475°C for 30 minutes, the structural change from β to ω is complete, but the composition of these well-developed ω precipitates (~ 4 at%Mo) does not still reach equilibrium (more specifically the end of the tie line within the metastable β+ω phase field on the Ti-Mo binary phase diagram). On more extended periods of annealing at 475°C for 48 hours, the ω precipitates reject more Mo reaching a composition of ~ 2 at%Mo (Fig. 4.9(c)). While it is not possible to conclude that the ω precipitates have achieved their equilibrium composition,

especially considering the relatively slow diffusivity of Mo within the β matrix of Ti at 475°C, it is expected that after 48 hours annealing, these precipitates achieve a near-equilibrium composition. The ω precipitates also grow (and coarsen) to large sizes ~80 nm after the 48 hours annealing.

4.4 Summary

This chapter presents direct experimental evidence of phase separation (or compositional clustering) within the bcc β matrix of a Ti-9at%Mo alloy, leading to initiation of collapse of the {111} β planes within Mo-depleted pockets resulting in formation of ω embryos. Coupling aberration-corrected HAADF-HRSTEM with atom probe tomography, the atomic scale structure and nano-scale composition of these ω embryos has been conclusively established. It has been shown that in as-quenched state the beta to omega transformation is not only partial in terms of structural changes associated with shift of <111>β atomic columns, but also the composition of these nano-scale particles are far from their so called thermodynamic equilibrium. Thus these precipitates are in metastable "frozen" state both structurally as well as compositionally. Subsequent isothermal annealing of the Ti-9at%Mo alloy at 475°C, results in increase in the extent of collapse of the {111} β planes leading to a fully-developed ω structure accompanied by rejection of Mo from the growing ω precipitates, even though equilibrium composition is not achieved (~ 4at%Mo). Finally after aging at 475ºC for 48hrs the Mo content in ω particles are further reduced, reaching a composition of ~ 2 at%Mo. This still might not be the equilibrium composition of ω particles; however they are much closer to equilibrium as compared to the rapidly cooled condition. Also it could be deduced that structurally the ω transformation is complete after 30 minutes of aging, but the compositional aspect of the transformation is quite sluggish, most probably due to the presence of heavy element like Mo. These results provide

novel insights into the mechanisms of β to ω transformations in metallic systems by capturing the earliest stages at atomic to near atomic spatial and compositional resolution.

4.5 References

[1] Chang ALJ, Sass SL, Krakow W. Acta Metall 1976;24:29.

[2] Kuan TS, Sass SL. Phil. Mag 1977;36(6):1473.

[3] Sukedai E, Hashimoto H, Hida M. Japan Jour. of Applied Phys 1987;26:L961.

[4] Kuan TS, Sass SL. Acta Metall 1976;24:1053

[5] Sukedai E, Liu W, Awaji M, Horiuchi T. Ultramicroscopy 1994;54:192.

[6] Sukedai E, Kitano Y, Ohnishi A. Micron 1997;28 (4):269.

[7] Van der Stam M, Stekelenburg M, Freitag B, Hubert D, Ringnalda J. Microscopy and Microanalysis 2005;19(4):9.

[8] Nellist PD, Chisholm MF, Dellby N, Krivanek OL, Murfitt MF, Szilagyi ZS, Lupini AR, Borisevich A, Sides Jr. WH, Pennycook SJ. Science 2004;305:17.

[9] Pennycook SJ, Nellist PD. Impact of Electron Microscopy on Materials Research, sKluwer Academic, Dordrecht; 1999.

[10] Pennycook SJ, Jesson DE. Phys. Rev. Lett 1990; 64:938.

[11] Nellist PD, Pennycook SJ. Ultramicroscopy 1999;78:111.

[12] Hickman BS. Trans. TMS-AIME, 1969;245:1329.

[13] Blackburn MJ, Williams JC. Trans. TMS-AIME, 1969;242:2461.

[14] Vassel A. Beta Titanium in the 1990‟s. TMS, Warrendale, PA; 1990.

[15] Devaraj A, Williams REA, Nag S, Srinivasan R, Fraser HL, Banerjee R. Scripta Mat 2009;61(7):701.

[16] De Fontaine D, Paton NE, Williams JC. Acta Met 1971;19:1153.

[17] Silcock JM. Acta Metall Mater 1958;6:481.

[18] Hellman OC, Vandenbroucke JA, Rusing J, Isheim D, Seidman DN. Microscop. Microanal 2000;6:437.

[19] Sudbrack CK, Noebe RD, Seidman DN. Physical Review B 2006;73:4.

[20] Haley D, Petersen T, Barton G, Ringer SP. Philosophical Magazine 2009;89:925.

[21] De Fontaine D, Buck O. Phil. Mag 1973;27(4):967.

[22] De Fontaine D, Acta Met 1970;18:275.

[23] Williams REA. Development and application of advanced microscopy characterization techniques to binary titanium-molybdenum alloys, PhD dissertation, Ohio; 2010.

CHAPTER 5

FIRST PRINCIPLE COMPUTATION TO ESTIMATE THE ENERGETICS OF β TO ω TRANSFORMATION IN Ti-Mo ALLOYS

5.1 Introduction

This chapter primarily focuses on the first principle computational work to understand the thermally activated (isothermal) ω precipitation within the β (body-centered cubic or bcc) matrix of simple model binary Titanium-Molybdenum (Ti-Mo) alloys. Preceding chapter presented the direct experimental evidence of the formation of embryonic ω from competing compositional and structural instabilities arising in the bcc lattice of Ti-Mo alloys during rapid cooling from the high temperature single β phase field. Through the experimental results obtained using aberration corrected high resolution scanning transmission electron microscopy and three dimensional atom probe a possible correlation between the extent of displacive collapse and composition of the parent β phase was postulated.

Following three questions were raised from the experimental efforts presented in the previous chapter.

1. Is phase separation in β phase of Ti-9at%Mo mandatory for β to ω phase transformation?
2. Why is the collapse of {111}β planes arrested in partial extent during β to ω transformation? Is the extent of collapse a function of local composition near the transformation region?

This chapter summarizes the attempt to analyze the existence of such a correlation between the extent of displacive collapse and the composition of the solute-depleted regions in Ti-Mo alloys by first-principles electronic structure based calculations using Vienna ab-initio simulation package (VASP).

An understanding of the potential energy landscape of the β and ω phases of Ti and the Ti-Mo alloy compositions are needed to answer these questions. This can be defined as a problem of finding the existence of any local minima within the transformation pathway from β phase to ω phase. Such local minima can be a possible reason for the stabilization of such experimentally observed partially transformed structures. First principle computations using VASP is a powerful tool to understand such energy pathways for phase transformations of elements and alloys [1-4]. Initially 24 atom super cells of pure Ti β and ω were created based on the experimentally observed crystallographic orientation relationship with a direct correspondence of the atomic coordinates between the initial β and final ω structures. Subsequently these initial and final structures were relaxed using energy minimization with Vienna ab-initio simulation package (VASP) [1-4]. Thereafter Mo substitution was performed to obtain the β and ω structures for 8.33, 12.5 and 16.66 at% compositions equivalent to 2, 3 and 4 Mo atoms. The energies of the initial and final structures for these compositions were also estimated after structure optimization calculations using VASP. Thereafter 10 intermediate images were linearly interpolated between the untransformed initial β and fully transformed final ω structure. Nudged Elastic band method was used to relax the intermediate mages to find the minimum energy pathway for the phase transformation [5]. Finally the minimum energy pathways for 0at%, 8.33at%, 12.5% and 16.33 at% Mo were compared to investigate the dependency of composition on the extent of transformation.

For the VASP DFT computations projected augmented wave (PAW) potentials [6, 7] and generalized gradient approximation (GGA-PBE) [8, 9] was used. Initially convergence test was done to determine the optimal parameters such as energy cut off and k mesh spacing for integration. 400 eV energy cut off was used for all the calculations and the computations were

converged up to 0.1meV/atom. Theoretical background of the computational methodology and results of the computations are discussed in the subsequent sections of this chapter.

5.2 Crystallography of β to ω Transformation

The BCC lattice of β titanium can be considered to have a pseudo closed ABCABC packing of {222} planes [10]. The view along <110> and <111> directions of pure Ti, 24 atom super cell of β and ω are given in Fig. 5.1(a), (b), (c) and (d) respectively. This is in accordance to the past studies that have determined the β-ω orientation relationship, given as following [10].

$$(0001)\omega//(111)\beta \; ; \; <11\bar{2}0>\omega//<110>\beta$$

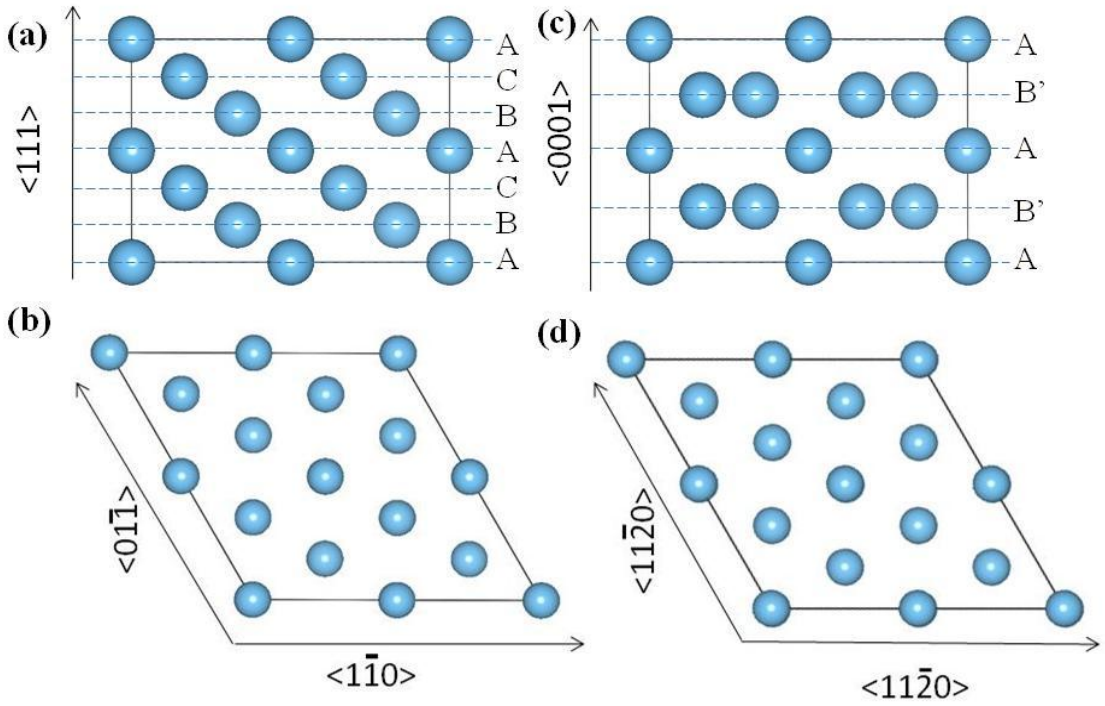

Fig. 5.1 view of the 24 atom pure Ti β super cell along (a) <1$\bar{1}$0> direction (b) <111> direction; View of the pure Ti 24 atom ω super cell along (c) <11$\bar{2}$0> direction (d) <0001> direction.

In order to transform the β super cell to an ω super cell, certain formalism has to be followed. The β super cell was made by defining the BCC unit cell such that the <1$\bar{1}$0> and <01$\bar{1}$> axes represents the „a" and „b" axes and <111> was denoted as the „c" axis. Thus the

angles α and β were chosen as 90^o and γ as 120^o. The ‚a", ‚b" and ‚c" axes in the ω super cell represented the <11$\bar{2}$0>, <1$\bar{2}$10> and <0001> directions respectively. This super cell structures had a direct correspondence between atomic coordinates as per the experimentally determined orientation relationship. Subsequently the Ti atoms in the collapsing planes were substituted with Mo atoms to obtain 8.33at%, 12.5at% and 16.33 at% Mo super cells. Thus 2 out of 24 Ti atoms were substituted by Mo to achieve the 8.33at% Mo super cell. Again when 3 and 4 Mo atoms were substituted in place of Ti, the super cells having 12.5 at% Mo and 16.66at% Mo respectively were created. Care was taken to substitute Mo atoms in corresponding atomic coordinates in both the β and ω configurations of each composition such that only a movement of $\pm\frac{1}{2}d(222)$ spacing was required for the atom from the initial β structure to transform into the final ω structure. The theoretical background on ab-initio VASP DFT computational methods used for the current study is given below.

5.3 Computational Approach

5.3.1 Density Functional Theory (DFT)

Ab-inito stands for “from scratch” in Latin, which means that everything is done by mathematical principles. Just by using the atomic number and some constants as the input many properties of the material can be calculated using ab-initio methods. In the first principle calculations an attempt is made to solve the Schrödinger equation. Schrodinger equation is the mathematical equation of wave function which in turn is related to the probability of finding an electron at some specific location near an atom or molecule [11]. The Schrödinger equation is given as

$$\hat{H}\Psi = E\Psi \qquad \text{Eqn. 1}$$

Where $\hat{H}$ is the Hamiltonian operator Ψ is the wave function and E is the total energy of the system. This is an eigen function since by applying the Hamiltonian operator ($\hat{H}$) on the original wave function we obtain the total energy and the original wave function.

The Hamiltonian operator $\hat{H}$ can be given as the following [11].

$$\hat{H} = \frac{-\hbar^2}{2m}\sum_i \nabla^2 + \sum_i V_{ext}(r_i) + \frac{1}{2}\sum_{i\neq j}\frac{e^2}{|r_i - r_j|} \qquad \text{Eqn. 2}$$

The individual terms are

Term 1: $-\frac{\hbar^2}{2m}\sum_i \nabla^2$ calculates the kinetic energies of the electrons as a function x, y and z coordinates

Term 2: $\sum_i V_{ext}(r_i)$ calculates the summation of all external potential due to the presence of atomic nuclei

Term 3: $\frac{1}{2}\sum_{i\neq j}\frac{e^2}{|r_i - r_j|}$ calculates all the inter electron interactions.

For a system with many electrons, solving Schrodinger equation exactly for the wave function and total energy of the system becomes highly computationally demanding, since many body wave function is a 3N variable problem where N is the number of bodies in the system. Hence several approximations were used to reduce the computational challenge of dealing with the „many body problem" to one of „many one-body" problems. Even such approximations were useful and feasible to solve only problems with smaller system sizes [11]. Subsequently in 1964 Hohenberg and Kohn found that the many body wave function and thereby all the properties derived from it can be defined as a functional of electron density at ground state [12]. In mathematical terms at the ground state electron density, the total energy is at its minimum and is not susceptible to changes on first order variations in electron density [13].

i.e. at $n(r) = n(r)_0$

$$\frac{\delta E(n(r))}{\delta n(r)} = 0 \qquad \text{Eqn. 3}$$

This essentially reduced the problem with 3N variables of solving for the wave function ($\Psi(r_1, r_2, r_2 \ldots r_N)$) of N particles to a 3 variable problem of solving for electron density n(r). This offered an enormous simplification and time saving for computational resources [11]. This computational breakthrough was fully realized in practical form after the methodology of DFT was given by Kohn and Sham [14]. They introduced a new way of a calculating the total energy which is function of electron density as per the equation given below.

$$E[n(r)] = T[n(r)] + E_C[n(r)] + E_{XC}[n(r)] \qquad \text{(Eqn 4)}$$

The individual terms of this equation are explained below

$\boldsymbol{T[n(r)]}$ is the kinetic energy of electrons. In a real system the motion of one electron will be correlated with the motion of all the other electrons in the system. It is computationally a cumbersome problem to solve. Hence in density functional theory this many body real electron problem is replaced by the summation of the kinetic energies of many individual independent, effective electrons moving in an effective potential created by all other electrons. $T[n(r)]$ is defined as following [11, 13].

$$T[n(r)] = \sum_i n_i \int \psi_i^* \left[-\frac{\hbar^2}{2m}\nabla^2\right] \psi_i(r) dr \qquad \text{Eqn. 5}$$

Where ψ_i describes the single particle wave function of an individual effective electron.

$\boldsymbol{E_C[n(r)]}$ is Columb energy including the three columbic contributions of electron-electron repulsion (E_{ee}), electron-nuclei attraction (E_{en}) and nucli-nuclei repulsion (E_{nn}). For an atom α with atomic number Z_α these terms can be written as following.

$$E_{ee} = e^2 \iint \frac{n(r)n(r')}{|r-r'|} dr dr' \qquad \text{Eqn. 6}$$

$$E_{en} = -e^2 \sum_\alpha Z_\alpha \iint \frac{n(r)}{|r-R_\alpha|} dr \qquad \text{Eqn. 7}$$

$$E_{nn} = e^2 \sum_{\alpha\alpha'} \frac{Z_\alpha Z_{\alpha'}}{|R_\alpha - R_{\alpha'}|} \qquad \text{Eqn. 8}$$

$\boldsymbol{E_{XC}[n(r)]}$ is the electron exchange correlation energy. As the name implies this term has two parts exchange energy and correlation energy. Exchange energy is a consequence of Pauli‟s exclusion principle by which each electron gains an effective +e charge due to the absence of any electrons with same spin around its immediate surroundings. This +e charged surrounding around an electron was called as an exchange hole [13]. All other many body interactions possible between the electrons of opposite spin are included in the correlation energy term.

All terms except exchange correlation energy in Eqn. 4 can be precisely defined but exchange correlation energy is unknown. Hence approximations are made for this value and these approximations determine the accuracy of the results of the DFT calculation [11, 13]. One of such simple and yet widely used approximation is local density approximation (LDA) where it is approximated that the exchange correlation energy only depends on the local electron density [14]. Mathematically representation of exchange correlation energy as per LDA can be given as.

$$E_{XC}[n(r)] = \int n(r)\varepsilon_{XC}[n(r)]dr \qquad \text{Eqn. 9}$$

Where $\varepsilon_{XC}[n(r)]$ is the exchange correlation energy per electron in a volume element „dr‟.

A better approximation was provided by Gradient Corrected Exchange correlation energy or general gradient approximation (GGA). GGA includes additional terms that depends on the gradient of electron density in addition to the local electron density at each point [8, 9]

Now the complexity of the computation is still dependent on the choice of basis set for $\{\psi_i\}$ which is the single, effective electron wavefunction used in eqn. 5. In crystallography, a unit cell is defined as the smallest repeating cell that has all the properties that are enough to describe the space by replicating it in three dimensions. In a similar manner the computational simulations are also defined within smaller periodic boundary condition which when repeated can represent

macro scale bulk characteristics of materials. Even on exiting the super cell, the wave function is made to be continuous by letting them reenter the periodic boundary through the opposite facet of the parallelepiped super cell [11]. Even in such a condition evaluating the wave function for all reciprocal lattice vectors (k vectors) inside such a super cell is not possible. Also it is impossible to include all the Fourier expansion terms of the Kohn Sham orbital. The problem of choosing k vectors are solved by employing a finite three dimensional grid of k points as per Monkhorst and Pack scheme [15] The Fourier series expansion terms to be considered are limited by a kinetic energy cut off value where the total energy of the system is converged within a certain energy tolerance set by the scientist [11]. Hence for the work given in this dissertation, initial convergence test were done to find out optimum k mesh spacing and kinetic energy cut off value to obtain an energy convergence of 0.1meV/atom.

The computational burden is further reduced by choosing pseudo potentials to describe the wave functions of electrons closer to nuclei. Such electrons are subjected to rapid oscillations in wave function near the atomic nuclei. But those effects can be neglected since only valence electrons take part in deciding the interactions between atoms. The replacement of the rapidly oscillating wave function with smooth pseudo wave functions within the core radius of atom helps to reduce the number of plane waves needed to describe the electron density. This was initially proposed in the form of ultra soft pseudo potentials [16, 17]. Later on it was further developed in the form of projected Augmented Wave (PAW) potentials which combined the computational efficiency of pseudopotentials and accuracy of all electron methods [6, 7]. In this dissertation work PAW potentials were used for the computation.

5.3.2 Nudged Elastic Band Method for Finding Minimum Energy Pathways for Phase Transformation

Nudged elastic band method generates a number of intermediate transition state images between two end point structures by using linear interpolation of the order parameter. Subsequently the intermediate chain of images is relaxed computationally to obtain the minimum energy path way of the transformation [5, 18]. One of the conditions for applicability of nudged elastic band method is that the entire transformation can be described in terms of changes in some distinct order parameter values. In case of β to ω transformation the order parameter can be specified to change from 0 in the initial β to $\pm\frac{1}{2}d(222)$ for the atoms in the collapsing planes of the final ω structure.

The image interpolation and the advantages of nudged elastic band methodology are explained using the schematic 2D example given in Fig. 5.2. Image 01 and 05 are the initial and final structures for the transformation. Initially the distance of motion of two atoms in the middle are quantified and assigned as an order parameter for the transformation. Subsequently 3 images are interpolated linearly between the initial and final structure having partially transformed structure. On relaxation of the chain of these images using nudged elastic methodology an accurate estimation of the energy barrier for the transformation can be found out as shown by the black curve in Fig 5.2(b). The positions of individual images are shown by the black markers. Such a method of energetic relaxation using nudged elastic band methods avoid other problems like corner cutting and image sliding to minima observed while using plain elastic band calculations. Corner cutting is shown by the red curve in Fig. 5.2(b) where the pathway stays away from the minimum energy pathway for the transformation. Image sliding is shown by the blue curve given in Fig. 5.2(b) where the individual images represented by markers essentially slide down to the minima giving a wrong estimate of the energy barrier for the transformation. High spring constant values (k) cause the springs connecting the images to pull them away from

the minimum energy pathway causing corner cutting. Whereas low spring constant value will cause the images to slide down to the energy minima due to inter atomic forces at the saddle point. These two opposing trends of k values make it difficult to estimate the minimum energy pathway of phase transitions accurately by plain elastic band calculations [5, 18].

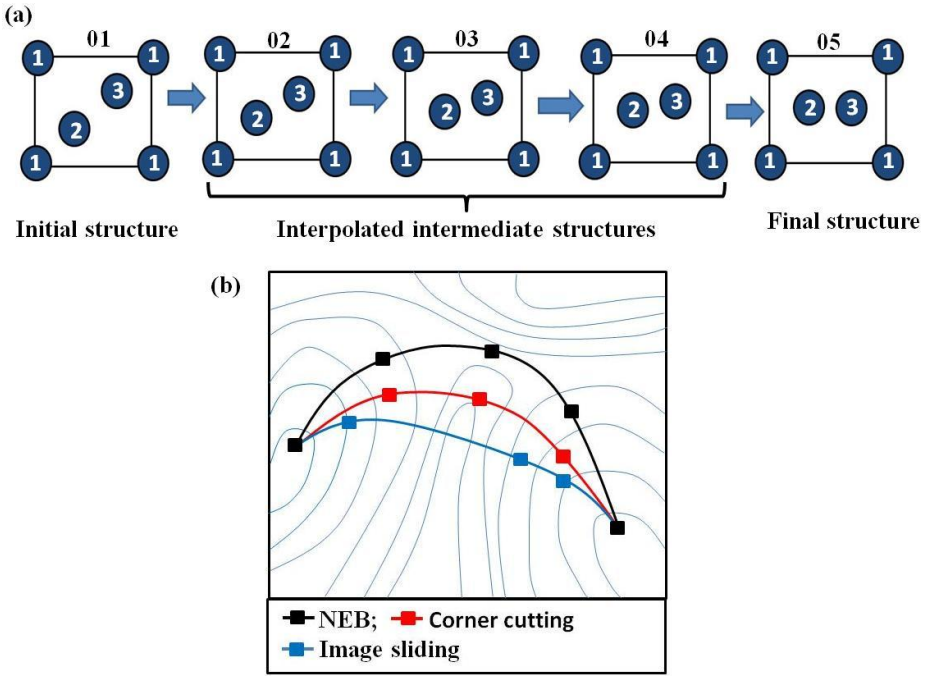

Fig. 5.2 (a) a simple 2D model for a structural transformation from initial structure 01 to final structure 05 through interpolated 02 to 04 intermediate states with partial displacement of atoms (b) Black curve showing the closest estimation of minimum energy pathway obtained by nudged elastic band (NEB) super imposed on the potential energy contour curve; Red curve showing the problem of corner cutting; Blue curve showing the problem of image sliding.

The nudged elastic method evolved from initial plain elastic band methodology calculations for finding transition states. In NEB the elastic bands are used to keep the images equally spaced. Then "zeroing" out of the perpendicular and longitudinal force on images helps to confirm the relaxation of intermediate states to the minimum energy pathway. Every j^{th} atom in an image I is considered to be connected with the j^{th} atom in the images I+1 and I-1. The position of an atom j in image I is $\overrightarrow{R_{I,j}}$. Then the tangent of the pathway can be defined as follows [5].

$$\hat{t} = \frac{\overrightarrow{R_{I+1,J}} - \overrightarrow{R_{I-1J}}}{||\overrightarrow{R_{I+1,J}} - \overrightarrow{R_{I-1J}}|}$$

Then force on the j^{th} atom of image I is defined as

$$F_{I,j} = F_{Ij}^{Atom}(\text{Perpendicular to path}) + F_{Ij}^{Spring}(\text{Parallel to path})$$

$$F_{I,j} = (F_{Ij}^{Atom} - (F_{Ij}^{Atom}.\hat{t}_{Ij})\hat{t}_{Ij}) + (F_{Ij}^{Spring}.\hat{t}_{Ij})\hat{t}_{Ij}$$

This make sure that the minimum energy path way has zero force and makes the predicted path independent of spring constant (k) unlike plain elastic band calculations[5].

After calculating the forces on all individual images the atoms of the images are allowed to relax using steepest descent until they converge to the minimum energy pathway of the transformation [18].

5.4 Computational Results and Discussion

5.4.1 Structure Relaxation

Initially super cells of β and ω structures were made for pure Ti with the following orientation.

β super cell orientation: a <1$\bar{1}$0>; b <01$\bar{1}$>; c <111>; α, β = 90^o; γ = 120^o.

ω super cell orientation: a <11$\bar{2}$0>; b <1$\bar{2}\bar{1}$0>; c <0001>; α, β = 90^o; γ = 120^o.

These super cells satisfy the experimentally observed orientation relationship given in section 5.2. Initial structural relaxation studies were done in 6 atom super cells of pure Ti β and ω. Subsequently 24 atom super cells were created to accommodate a wider compositional range. The view of 24 atom β super cell along <1$\bar{1}$0> and <111> directions are given in Fig. 5.1(a) and (b). The view of 24 atom ω super cell along <1$\bar{2}\bar{1}$0> and <0001> directions are given in Fig. 5.1(c) and (d). The ABCABC stacking of {222} planes in β super cell (highlighted in Fig. 5.1(a)) transforms to the AB‟‟AB‟‟ stacking sequence in ω super cell (highlighted in Fig. 5.1(c)). The

atoms at B and C planes of the β super cell move by ±1/2d(222) distance to form the atoms in plane B‟ in the final ω super cell. However the atoms in the A plane of beta and w structures remain stationary across the entire transformation. In this work the atoms on B and C planes of β phase that move during the transformation are named as „œllapsing atoms‟ considering that they are collapsing to an intermediate plane B‟. The complete structure relaxation was performed using VASP 4.6 to find the fully relaxed energy and structure of β and ω phases. During the relaxation ISIF tag in VASP INCAR file was kept to be 3 to allow a full relaxation of the structure by allowing relaxation of ion positions, cell shape and cell volume. The resulting lattice dimensions and energy without entropy values obtained for a 6 atom super cell of pure Ti β and ω structures are given in table 5.1.

Composition & structure	Supercell dimensions (nm)			Energy/atom eV/atom
	a	b	c	
Pure Ti Beta	4.5995	4.5995	2.81675	-7.7822
Pure Ti Omega	4.5773	4.5773	2.82975	-7.8968
Change in dimension & energy (%)	**-0.48**	**-0.48**	**0.46**	**-0.1146**

Table 5.1. Full relaxation results for 6 atom super cell pure Ti β and ω structures.

From these values it can be said that β to ω phase transformation can result in a contraction of 0.48% along „a‟ and „b‟ axis with an expansion of 0.46% along the c axis of super cells. Also for pure Ti the energy of ω super cell was found to be 114.6 meV/atom lower than the energy of the β super cell.

Subsequently the super cell size was increased from 6 to 24 atoms to have an option of attaining multiple composition values by substitution of Mo. Thereafter 2, 3 and 4 Mo atoms were substituted for Ti atoms in B and C planes of 24 atom, pure Ti β and ω super cells to obtain 8.33, 12.5 and 16.66 at% Mo compositions respectively. All the 24 atom super cells for pure Ti,

Ti-8.33at %, Ti-12.5at% and Ti-16.66at% Mo were relaxed using VASP. Table 5.2 shows the β and ω lattice parameters and energies after complete structure relaxation of all the 24 atom super cells. From table 5.2 it can be seen that the pure Ti ω phase still had an energy value which is 114meV/atom lower than the β phase . On addition of 8.33 at% Mo the energy difference between ω and β phase was lowered to 22.1 meV with still a lower energy for ω phase than β phase. However on further addition of Mo to 12.5% the energy of ω phase became 22.1meV higher than the β phase. This energy differential further increased to 73.3meV/atom in 16.66at% Mo composition with ω phase having a higher energy than β phase. In the nudged elastic band (NEB) calculations the 0.48% difference in lattice parameter was ignored to facilitate a linear path definition between the initial and final images. Hence the β cell dimensions were used for both β and ω phase.

Composition & structure	Supercell dimensions (nm)			Energy/atom eV/atom	delta (Eomega-Ebeta) eV/atom
	a	b	c		
Pure Ti Beta	4.598017	4.591971	2.822593	-7.7823	-0.1140
Pure Ti Omega				-7.8964	
Ti- 8.3% Mo Beta	4.58367	4.577642	2.813785	-8.0908	-0.0277
Ti- 8.3% Mo Omega				-8.1186	
Ti- 12.5% Mo Beta	4.598017	4.591971	2.822593	-8.2520	0.0221
Ti- 12.5% Mo Omega				-8.2298	
Ti- 16.6% Mo Beta	4.598017	4.591971	2.822593	-8.4125	0.0733
Ti- 16.6% Mo Omega				-8.3392	

Table 5.2 Lattice parameter and energy of ω and β structures used for 24 atoms super cell nudged elastic band method calculation.

5.4.3 NEB Results of 24 Atom Super Cells.

Ten intermediate images of partially transformed structures were generated for pure Ti, Ti- 8.33at%, Ti-12.5at% and Ti-16.66at% Mo. All these intermediate structures were relaxed using NEB method to obtain the minimum energy path for the transformation. The energetic path obtained for β to ω transformation is plotted in the graph given in Fig. 5.3.

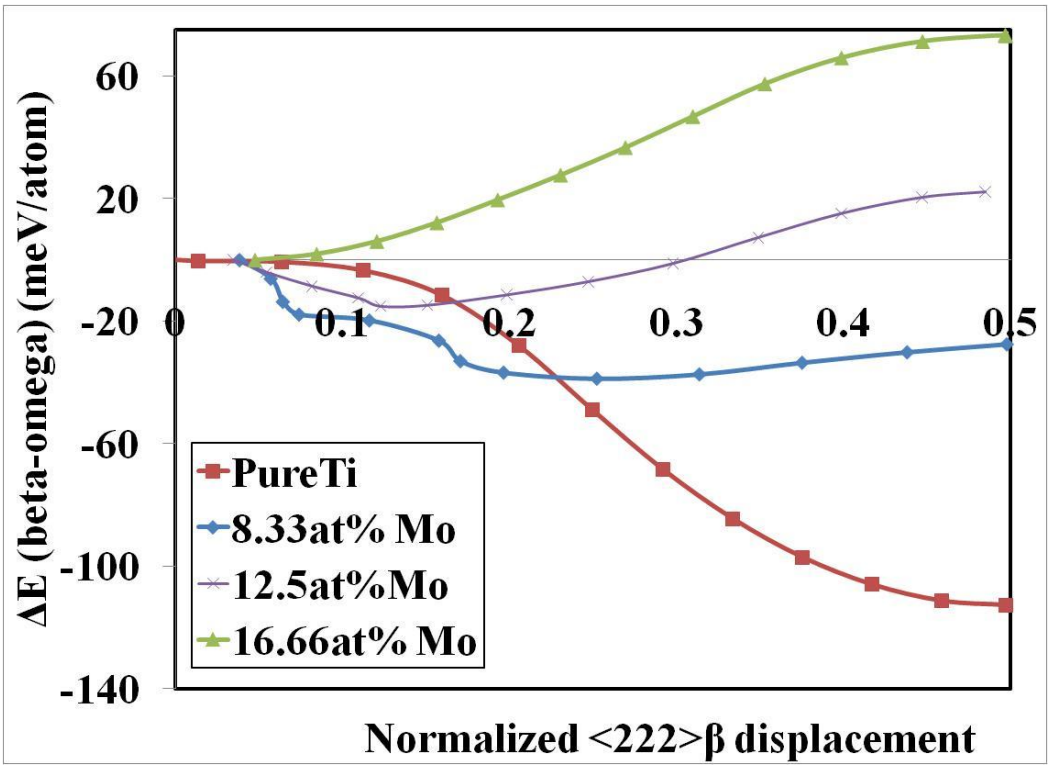

Fig. 5.3 Nudged elastic band results for 24 atom super cell systems with 0 at%, 8.33 at%, 12.5at% and 16.66 at% Mo. X axis is average collapse distance normalized with inter planar spacing of <222> planes of β phase. Y axis is the difference in energy, taking β phase as the reference.

The x coordinate of the graph correspond to average displacement of all 16 collapsing atoms, normalized with d(222) spacing. Hence 0.5(d222) spacing would correspond to a fully transformed ω structure of pure Ti. The y axis of the graph is the energy differential considering β phase of each composition as the reference point. For pure Ti a barrier less roll down transformation can be seen based on the energetic vales observed. However for 16.66 at% Mo the omega transformation is leading to an increase in energy. In an intermediate composition of 8.33at% Mo and 12.5at% Mo local energy minima with energy values lower than either of the end point β or ω configurations can be observed. For Ti-8.33at% Mo composition the local minima can be seen at $0.25d_{222}$ spacing. For Ti-12.5at% Mo the local minima correspond to a displacement of $0.12d_{222}$.

5.5 Novel Insights Towards β to ω Phase Transformation

Based on atomic column intensity measurements along <111> direction in HRSTEM image, presence of ω embryos with 0.16-0.2 d(222) displacement was shown in rapidly quenched Ti-18wt% (Ti-9at%) Mo. This HRSTEM atomic column intensity is an average intensity obtained through the thickness of sample. Due to the averaging along the sample thickness it is very difficult to obtain the exact atomistic nature of the atomic displacements within the ω precipitates by HRSTEM. VASP calculations using NEB can give a true atomistic picture of the atomic displacements and energetic of β to ω phase transformation.

The Ti-8.33at% Mo composition was obtained by substitution of 2 Mo atoms in a super cell of 24 atoms of Ti. These two Mo atoms were substituted in one of the 16 collapsing atoms present in B or C planes in the super cell. The 8 of the 12 images of the structures along the minimum energy pathway obtained by NEB calculation of Ti-8.33at%Mo are shown in Fig. 5.4. The Ti atoms are shown in blue and Mo atoms are shown in purple color. The ABCABC stacking of (222) planes in initial β structure are marked in the Fig. 5.4(a). The direction of atomic movements is shown in Fig. 5.4(b) with arrows. The 9th image of the structure corresponding to the local minima in NEB energy curve shows a variation in the extent of collapse for the 16 collapsing atoms as shown in Fig. 5.4(f). In Fig. 5.4(f) it can be seen that the Mo atoms appear to constrain the collapse of Ti atoms that are directly aligned in the same <111> direction. The average of the displacements (collapses) of all the 16 atoms of B and C planes for the minimum energy structure correspond to 0.25 d_{222}. This value of the average displacements is very similar to the average displacement value obtained from the experimental HRSTEM intensity measurements.

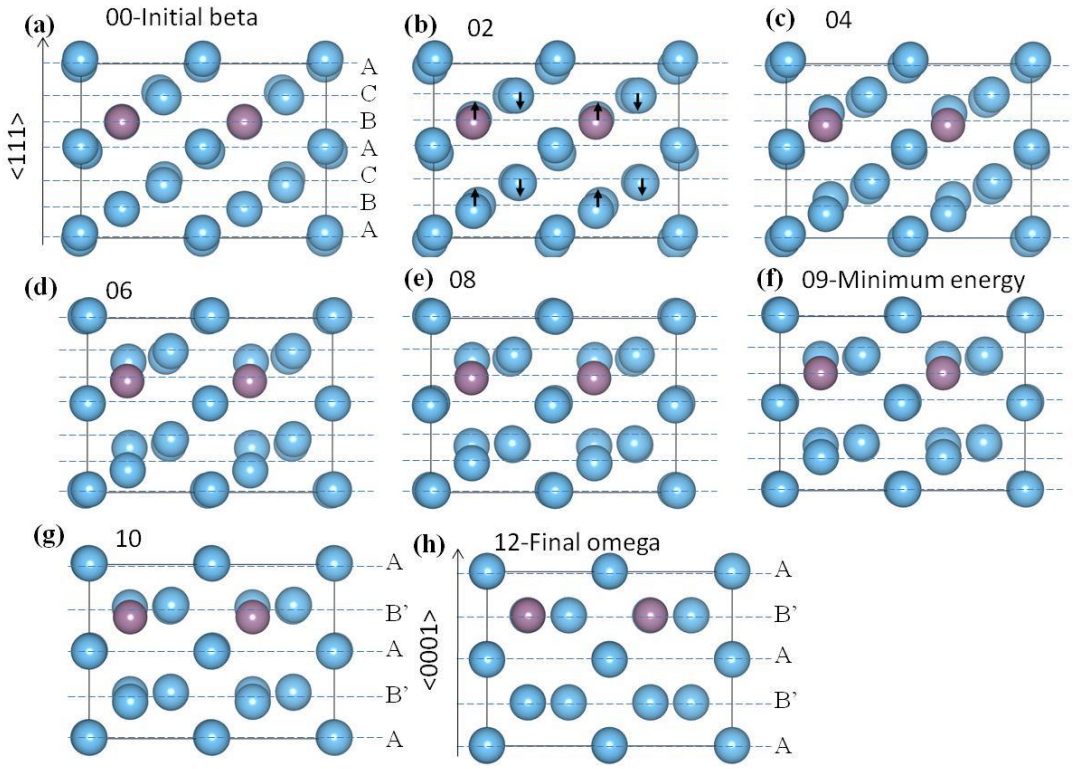

Fig. 5.4(a) view of 24 atom Ti-8.33at% Mo β super cell along <1$\bar{1}$0> direction (b) 2nd image in NEB pathway showing the direction of collapsing atoms with arrows (c)-(e) 4th, 6thand 8th intermediate transition state (f) The minimum energy configuration for Ti-8.33at%Mo composition (g) Intermediate structure in between minimum energy structure and final w structure (h) view of 24 atom Ti-8.33at% Mo ω super cell along <11$\bar{2}$0> direction showing final AB‟AB‟ stacking.

From energy values of β and ω end points given in Fig. 5.3, it can be said that for Ti-16.66at%Mo, β structure will be more stable than ω structure. For Ti-12.5at% Mo and Ti-8.33at% Mo, a structure with an average collapse of 0.12 and 0.25 d_{222} have the lowest energy and will be more stable in comparison to β or ω structures.

The experimental HRTEM observation of complete collapse in 475^{o}C 30 minutes aged sample and corresponding atom probe investigation showing an increased partitioning of Mo atoms between β and ω phases points to the possibility of an inverse proportionality between Mo content and extent of collapse. All previous theoretical and experimental studies in β to ω phase

transformation did not point to any variation or spread in extent of collapse within the omega precipitate. Also a dependency of Mo composition on extent of atomic displacements has not been highlighted by any prior investigations in literature.

5.6 Summary

The atomic level mechanism of β to ω transformation was investigated in detail by coupling the experimental information obtained from high resolution scanning transmission electron microscopy (HRSTEM) and atom probe tomography with first principle calculation. The dependency of composition and stabilization of partially transformed intermediate structures were investigated using VASP Nudged elastic band method calculations. From the computational results it can be seen that a partially transformed structure with an average plane collapse of $0.25d_{222}$ offer a local minima in energy for Ti-8.33at% Mo alloy. This extent of collapse is similar to the experimentally observed partially transformed ω embryo structures in rapidly quenched Ti-9at% Mo alloy.

5.7 References

[1] Kresse G, Hafner J. Phys. Rev. B 1993;47:558.

[2] Kresse G, Hafner J. Phys. Rev. B 1994;49:14251.

[3] Kresse G, Furthmüller J. Comput. Mat. Sci 1996;6:15.

[4] Kresse G, Furthmüller J. Phys. Rev. B 1996;54:11169.

[5] Jónsson H, Mills G, Jacobsen KW: Nudged elastic band method for finding minimum energy paths of transition. in: Berne BJ, Ciccotti G, Coker DF (eds.). Classical and Quantum Dynamics in Condensed Phase Simulations. ;1997.

[6] Blochl PE. Phys. Rev. B 1994;50:17953.

[7] Kresse G, Joubert D. Phys. Rev. B 1999;59:1758.

[8] Perdew JP, Burke K, Ernzerhof M. Phys. Rev. Lett 1996;77:3865.

[9] Perdew JP, Burke K, Ernzerhof M. Erratum. Phys. Rev. Lett 1997;78:1396.

[10] Banerjee S, Mukhopadhyay P. Phase transformation: examples from titanium and zirconium alloys; Oxford, UK: Pergamon Press; 2004.

[11] Heikki Pitkanen; First principle modeling of metallic alloys and alloy surfaces; PhD dissertation, Lappeenranta; 2009.

[12] Hohenberg P, Kohn W. Phy. Rev 1964:136;B864.

[13] MedeA user guide

[14] Khon W, Sham L. Phys. Rev 1965;140:A1133.

[15] Monkhorst HJ, Pack JD. Phys. Rev B 1977;13:5192

[16] Vanderbilt D. Phys. Rev. B 1990;41:7892.

[17] Kresse G, Hafner J. J. Phys.: Condens. Matter 1994;6:8245.

[18] Dallas Trincle, PhD Dissertation; 2003.

CHAPTER 6

PHASE SEPARATION AND α PHASE PRECIPITATION IN Ti-20Mo-5Al ALLOY

6.1 Introduction

A system can be forced to stay in metastable equilibrium when a high temperature homogeneous single phase system is rapidly quenched to a low temperature where two or more phases coexist. If given sufficient energy and time, such a system that is constrained in a metastable equilibrium would attempt to reach the thermodynamically stable phase mixture by phase separation [1]. The IUPAC definition of phase separation is "the process by which a solid (liquid) phase separates into two or more phases"[2]. Phase separation can occur through two distinguishable pathways, nucleation and growth or spinodal decomposition. Spinodal decomposition will be the path of phase separation if small compositional fluctuations in such a metastable system lead to a reduction in free energy. Whereas nucleation and growth will be the chosen pathway if the free energy of the system is increased as a result of small compositional fluctuation necessitating a large compositional fluctuation to reduce free energy [3]. A reduction in free energy on compositional fluctuations of an otherwise homogenous but metastable system can occur if the system has a clustering tendency. A positive enthalpy of mixing ($\Delta H_{mix}>0$) between the components of a system can lead to a clustering tendency. Few past theoretical studies point to positive enthalpy of mixing and therefore a clustering tendency in Ti-Mo binary alloys [4,5,6]. Subsequently Blackburn and Williams postulated that phase separation can occur in Ti-20wt% Mo on ageing a quenched alloy at an appropriate temperature for sufficiently long time [7]. Phase separation tendencies in Ti-20Mo alloy system was also observed during step quenching ageing experiments performed in Ti-20% Mo alloy by Chandrasekaran et al. [8]. Evidence of additional satellite spots around primary matrix reflection in selected area transmission electron microscopy (TEM) diffraction pattern along with dark field imaging was

indicative of β phase separation observed in the alloy on step quenching and ageing at 450^{o}C for 15 minutes. On longer term annealing at 450^{o}C, α precipitates were shown to nucleate on the solute lean β phase formed during phase separation [8]. Subsequently Furuhara et al. investigated the actual temperature range for β phase separation in Ti-10,20, 30 and 40 wt% Mo alloys and compared it with the existing calculated phase diagram of Ti-Mo binary alloys with the monotectoid reaction [9]. The information on morphology, crystallography and distribution of the α precipitates formed on isothermal ageing of the alloy at different temperatures was used as an indication of a possible phase separation reaction. The coherent binodal and spinodal lines were also calculated as a function of Mo content by calculating the effect of coherency strain on the free energy of β phase. The calculated coherent β phase separation boundary had a critical composition of 22wt% Mo [Fig. 10 in 9]. By comparing the calculated phase diagram with experimental results Furuhara et al. concluded that Ti-Mo binary alloy do not have a monotectoid reaction above 650^{o}C. Only Ti-40wt% Mo alloy aged below 550^{o}C was reported to show uniformly distributed α phase, which can be nucleated as a result of a β phase separation reaction [9].

Effect of ternary additions of Al, O, Sn and Zr in to binary Ti-Mo alloys on destabilization of omega phase and subsequent β phase decomposition was studied by Williams et al. [12]. Formation of uniformly distributed β_2 precipitates in the β matrix of Ti-10Mo-6Al alloy aged for 100hours at 350^{o}C after quenching from 950^{o}C was shown by dark field imaging formed by matrix reflections tilted away from the brag reflections. Authors attributed the observation of β_2 precipitates in the dark field images formed by using a BCC matrix reflection to a possible BCC structure for the precipitates. Also strain contrast observed in the matrix around the β_2 precipitates lead the authors to point to a possibility of having a coherent boundary

between the β_2 precipitates and matrix. On ageing Ti-8Mo-12Al alloys for 100hours at 350^{o}C after quenching from 950^{o}C, three different variants of α phase was shown to nucleate in the region were the β_2 precipitates were present. The preferential nucleation of α phase at the β2 precipitate location was used as a proof for the solute lean nature of the β_2 precipitates [7].

Along similar lines the alloys system chosen for the present work is Ti-20wt% Mo alloy with an addition of 5wt% Al. The candidate alloy was used for verifying the speculations of possible β phase separation during a low temperature ageing. Novel characterization tools including in-situ high energy synchrotron X-ray diffraction, selected area electron diffraction, dark field imaging, aberration corrected high resolution TEM and atom probe tomography were used to study the phase separation during in situ and ex situ isothermal ageing experiments. Coupling of these advanced techniques have helped to identifying the crystallographic and compositional partitioning associated with β phase separation observed in Ti-20Mo-5Al ternary alloy.

6.2 Experimental Procedure

The Ti-5Al-20Mo alloy was fabricated using Laser Engineered Net Shaping (LENS^{TM}). The process of LENS^{TM} has been discussed else were [10]. The oxygen content in the glove box was maintained below 10ppm for the entire deposition. The premixed Ti-5Al-20Mo powder was loaded into the powder feeder hoppers of LENS^{TM}. A mill annealed plate of Ti-6Al-4V was used as the substrate for the deposition. A cylindrical deposit of approximately 4mm height and 10mm diameter was fabricated. The LENS^{TM} deposit was sectioned along the axis of the deposit and was subjected to β solutionizing at 1000^{o}C for 30minutes in an atmosphere controlled furnace followed by water quenching. The water quenched sample was mounted and polished for metallographic characterization. The microstructure and composition along the compositional

gradient was characterized using scanning electron microscopy (SEM) and energy dispersive spectroscopy (EDS). The SEM studies have been conducted on an FEI Quanta 200 ESEM with solid state back scatter electron detector and EDAX detector. After SEM characterization conventional transmission electron microscopy (TEM) sample was prepared by argon ion beam milling of dimpled foils of 50μm thickness using 5KeV initial milling followed by 2KeV final milling. Transmission electron microscopy characterization was performed by selected area diffraction, bright field and dark field imaging using Tecnai F20 TEM operating at 200KV. The water quenched alloy sample was further sectioned to make two sample pieces. One sample was subjected to in-situ High Energy X-ray Diffraction (HEXRD) during ageing for 10hours at 400^{o}C at the 11IDC beam line of Advanced Photo source of Argonne National Lab. The other sample was sectioned to three pieces and was subjected to sequential ex-situ ageing at 400^{o}C for 6hours, 10 hours and 72 hours. Further the 400^{o}C 72hours aged sample was again up-quenched to 620^{o}C and aged for 1hour. All the ex situ heat treatments were done in atmosphere controlled Thermcraft furnace. The in situ heat treatment at Advanced Photon Source, Argonne national lab was performed in Linkam TS 1500 furnace.

After ageing treatments TEM and atom probe tomography (APT) samples were made using focused ion beam (FIB) from the 400^{o}C 6hours, 10hours, 72 hours aged samples and 620^{o}C 1hour aged sample. The FIB technique for TEM and APT sample preparation is described in section 3.4.3.1 and 3.4.3.2. Subsequently samples for APT-TEM coupling were made from samples that were aged for 72 hours at 400^{o}C and 1hour at 620^{o}C using procedures described in section 3.4.3.3. TEM diffraction, Dark Field imaging, Bright field imaging and high resolution TEM imaging of all TEM samples were performed using Tecnai^{TM} F20. Subsequently detailed high resolution imaging of 400^{o}C 10hours aged sample was performed using aberration corrected

Titan™ TEM. The atom probe analysis was carried out on Cameca APT 3000XHR system at a temperature of 60K in voltage evaporation mode. The evaporation rate was maintained in the range of 0.2 to 1% by using a pulse voltage with a magnitude of 20% of the applied standing voltage on the specimen. The TEM-APT coupling samples were analyzed using diffraction, dark field imaging and bright field imaging in Tecnai F20 before loading them in APT.

6.3 Results and Discussion

6.3.1 Investigation of Water Quenched Condition

The back scatter SEM image of water quenched Ti-5Al-20Mo showed predominantly large grains of β phase without any intra-granular or grain boundary α precipitates. SEM EDS analysis confirmed the composition to be Ti-20%Mo-5%Al in weight percent. Fig. 6.1(a) show the selected area diffraction (SAD) pattern recorded from the conventional TEM sample of the water quenched condition with a beam direction parallel to [110] direction of β phase. The primary reflections in this diffraction pattern can be consistently indexed as (0-11), (200) and (2-11) planes of BCC β phase with some faint reciprocal lattice streaking at 1/2{2-11} positions. This reciprocal lattice streaking can be attributed to β phase instabilities like ω formation or quenched in phase separation of a higher temperature. However the absence of any strong reflections from second phases like ω or α in the SAD pattern, render the Ti20Mo5Al to be a suitable candidate to study the decomposition of the metastable β phase on ageing. The ageing temperature was selected based on the experimental monotectoid diagram given by Furuhara et al. for Ti-Mo binary alloys [9].

6.3.2 In-situ High Energy X-ray Diffraction During Isothermal Ageing at 400^{o}C for 10 Hours

The water quenched Ti-20Mo-5Al alloy was aged at 400^{o}C for 10 hours in an atmosphere controlled Linkam T1500 Furnace placed in the Synchrotron X-ray diffraction beam line of

Advanced Photon Source in Argonne National Lab. The furnace temperature-time cycle and data acquisition was controlled remotely using scripts. Details of data acquisition and analysis procedure for in situ High Energy X-ray Diffraction (HEXRD) is given in section 3.4.5. For this study 2D X-ray diffraction spectrums were collected every minute throughout the length of 10hours of ageing at 400^{o}C. The images of the 2D X-ray diffraction spectrum were processed using Fit2D^{TM} software as per procedures given in section 3.4.5 to obtain the linear intensity vs. theta plots. Such linear intensity vs. theta plot for the entire period of ageing was analyzed to indentify the onset of β phase separation and subsequent α phase precipitation. The as quenched state exhibited an irregular β peak. No α peaks were observed as shown in Fig. 6.2(a) and (b). On ageing up to 318 minutes $\{200\}_{\beta}$ peak appeared to smoothen out to a symmetrical peak. The irregularity observed in the $\{200\}_{\beta}$ peak up to 318 minutes is probably due to the quenched in β instabilities. On further ageing from 318 minutes a progressively developing $\{200\}_{\beta}$ peak split can be observed as shown in Fig. 6.3 (a). Along with it the $\{10\bar{1}0\}_{\alpha}$ peak started to grow in intensity as shown in Fig. 6.3(b). The end condition at 400^{o}C 10hours shows a substantial peak of $\{10\bar{1}0\}_{\alpha}$ and a prominent split in $\{200\}_{\beta}$ peak.

6.3.3 β Phase Separation and α Phase Precipitation During Ex Situ Isothermal Ageing at 400^{o}C

In order to analyze the observation of sequential β phase separation and subsequent α nucleation in further detail, Ti5Al20Mo samples were aged at 400^{o}C for 6hours, 10hours and 72 hours. TEM samples were made after each ageing treatment to analyze the progress of β phase separation and α phase nucleation. The comparison of [110] β zone axis diffraction pattern for WQ and 400^{o}C/6hours, 400^{o}C/10hours and 400^{o}C/72hours aged condition are given in Fig. 6.4 (a) to (d). The progressive development of a strong reflection at ½ $\{112\}_{\beta}$ vector is an indication

of α nucleation. Diffraction spots from multiple variants of α and double diffraction spots start to show up on SAD patterns obtained from 10hours and 72hours aged condition.

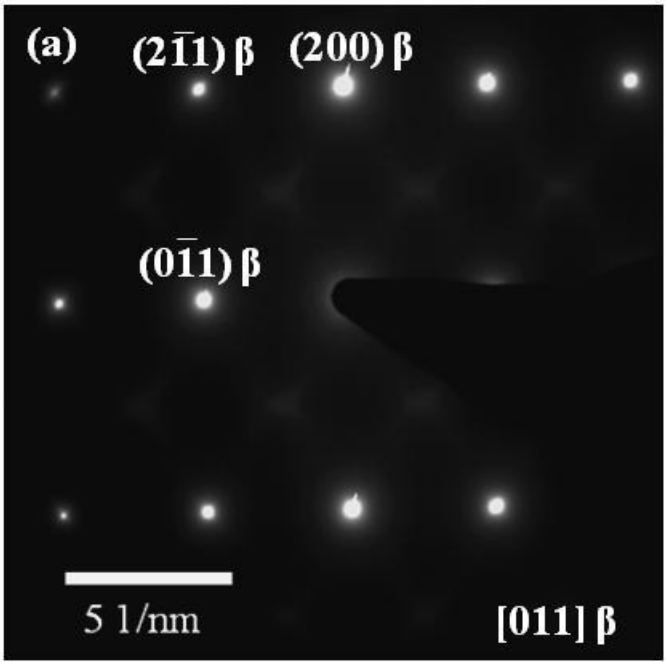

Fig. 6.1(a) β <011> selected area diffraction pattern from the water quenched Ti20Mo5Al alloy.

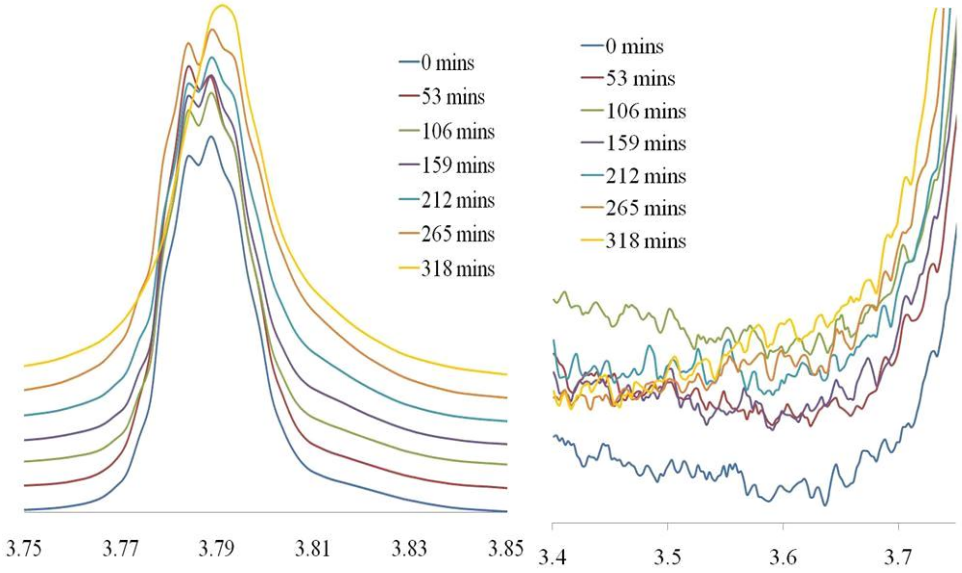

Fig. 6.2 (a) β {200} peak development as observed during in-situ HEX-ray Diffraction during annealing at 400^{o}C from 0 to 318 minutes (b) α {10-12} peak development as observed during in-situ HEX-ray Diffraction during annealing at 400^{o}C from 0 to 318 minutes.

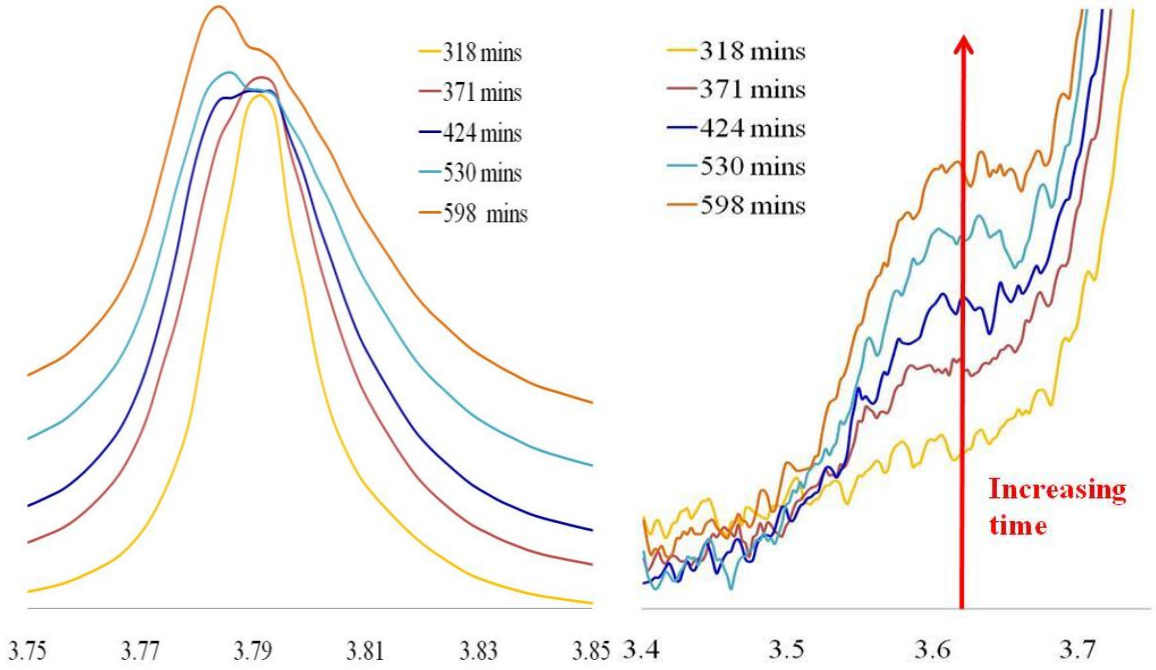

Fig. 6.3 (a) β {200} peak development as observed during in-situ HEX-ray Diffraction during annealing at 400^{o}C from 318 to 598 minutes(b) α {10-12} peak development as observed during in-situ HEX-ray Diffraction during annealing at 400^{o}C from 318 to 598 minutes.

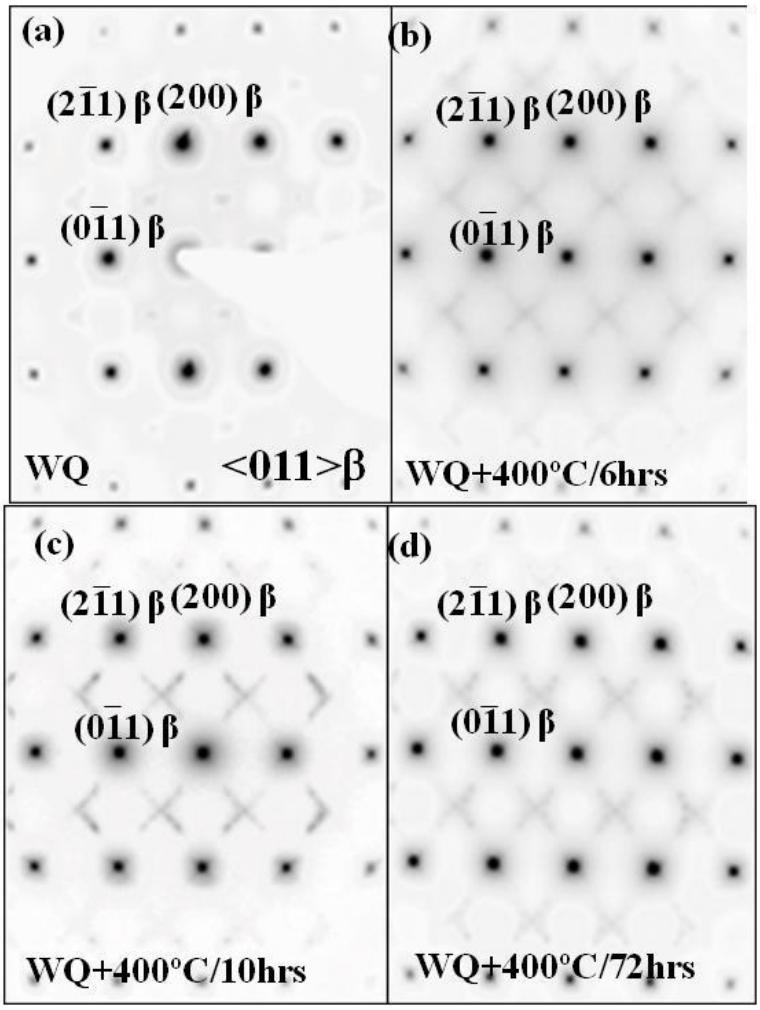

Fig. 6.4 progressive development of β <110> zone electron diffraction pattern for Ti20Mo5Al alloy (a) Water quenched condition (b) after 6hours aging at 400^{o}C (c) after 10hours aging at 400^{o}C (d) after 72 hours aging at 400^{o}C.

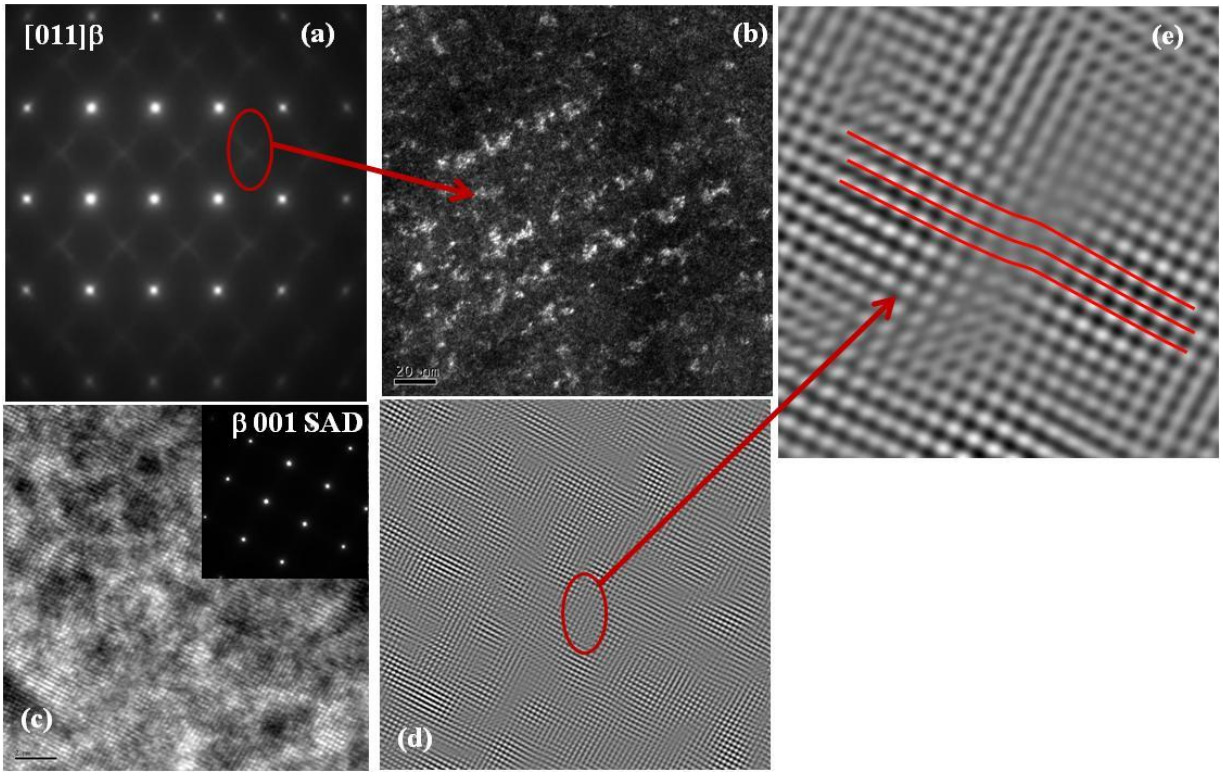

Fig. 6.5 (a) β <110> electron diffraction pattern for 400°C 6 hours aged condition after water quenching. The faint reflections marked by the red oval was used to form the dark field image given in (b). (c) The unfiltered β <001> HRTEM image with β <001> SAD given as inset. (d) Fourier filtered β <001> zone axis HRTEM image> with the red oval showing the magnified view given in (e). The change in lattice parameter and the plane bending observed between two regions are marked by the red lines in Fig. (e).

6.3.4 β Phase Separation in Ti-20Mo-5Al Alloy after Isothermal Ageing for 6 Hours at 400°C

To understand the origin of diffuse streaking in the β<110> SAD pattern from 400°C 6hours aged condition, DF images were taken using the reciprocal lattice streaking at ½ $\{112\}_\beta$ positions. The streak used to form the dark field image is marked with a circle in Fig. 6.5(a). The dark field image given in Fig. 6.5(b) is showing periodic bright contrast regions of less than 10nm size scale uniformly distributed across the entire image. To further understand the nature of these bright contrast regions, High Resolution TEM images were recorded. The unfiltered HRTEM image along $<100>_\beta$ zone axis is shown in Fig. 6.5(c). The corresponding diffraction

pattern is shown in the inset. The background subtracted (Fourier filtered) image is given in Fig. 6.5(d). On detailed analysis, substantial straining can be observed in the β lattice. This is evident further from the magnified view shown in Fig. 6.5(e) that clearly shows the boundary between two regions of β lattice with different lattice parameters. This leads to pronounced straining of the lattice planes at the interface. Such a phenomenon could be due to phase separation in β matrix leading to pockets of different composition, which in turn could result in a difference in lattice parameter value of those regions. To maintain coherency between such pockets of different composition, the lattice planes will need to be strained at the interface.

6.3.5 Coexistence of β Phase Separation and α Phase Precipitation in Ti-20Mo-5Al Alloy after Isothermal Ageing for 10 hours at 400^{o}C

The <001> β SAD pattern from 400^{o}C 10hours aged condition is shown in Fig. 6.6 (a). Fig. 6.6 (b) shows the simulated SAD pattern considering all 12 variants of α in β matrix and β phase separation in the β matrix. The primary β reflections, α reflections and reflections due to phase separation are marked in the simulated pattern. The dark field images formed from the α reflection (marked by red circle) is shown in Fig. 6.6(c). A high magnification view of the diffracting regions obtained in DF image is shown in Fig. 6.6(d). These bright contrast regions are of the order of 20nms. HRTEM imaging of the same region was performed to better understand the crystallographic nature. The unfiltered HRTEM image is shown in Fig. 6.7(a). The background subtracted (Fourier filtered) image is shown in Fig. 6.7(b). On cursory inspection of the filtered image, substantial strain contrast can be observed in the β matrix. On detailed analysis a region with crystallographic similarity to α (red circle) is observed within the β matrix. The magnified view of the region with α nuclei is shown in Fig. 6.7(c). An α nucleus of about 3-5nm size is marked with the yellow hexagon showing the <11-20> α motif. The

<001> β motif is marked with the red square in the same image. The bright regions with 20nm size scale, observed in the dark field images can be attributed to the strain contrast arising from long range straining of the β matrix due to the presence of coherent nuclei‟s of α. Aberration corrected high resolution TEM images were taken in a different zone axis in order to obtain a further clearer understanding of the nature of these α nuclei. The aberration corrected HRTEM image taken along <111> β zone axis is shown in Fig. 6.8(a). The magnified view of the strained regions corresponding to the α nuclei is shown in Fig. 6.8(b) and (c). The regions corresponding to α nuclei is shown highlighted with the black ellipse in the images.

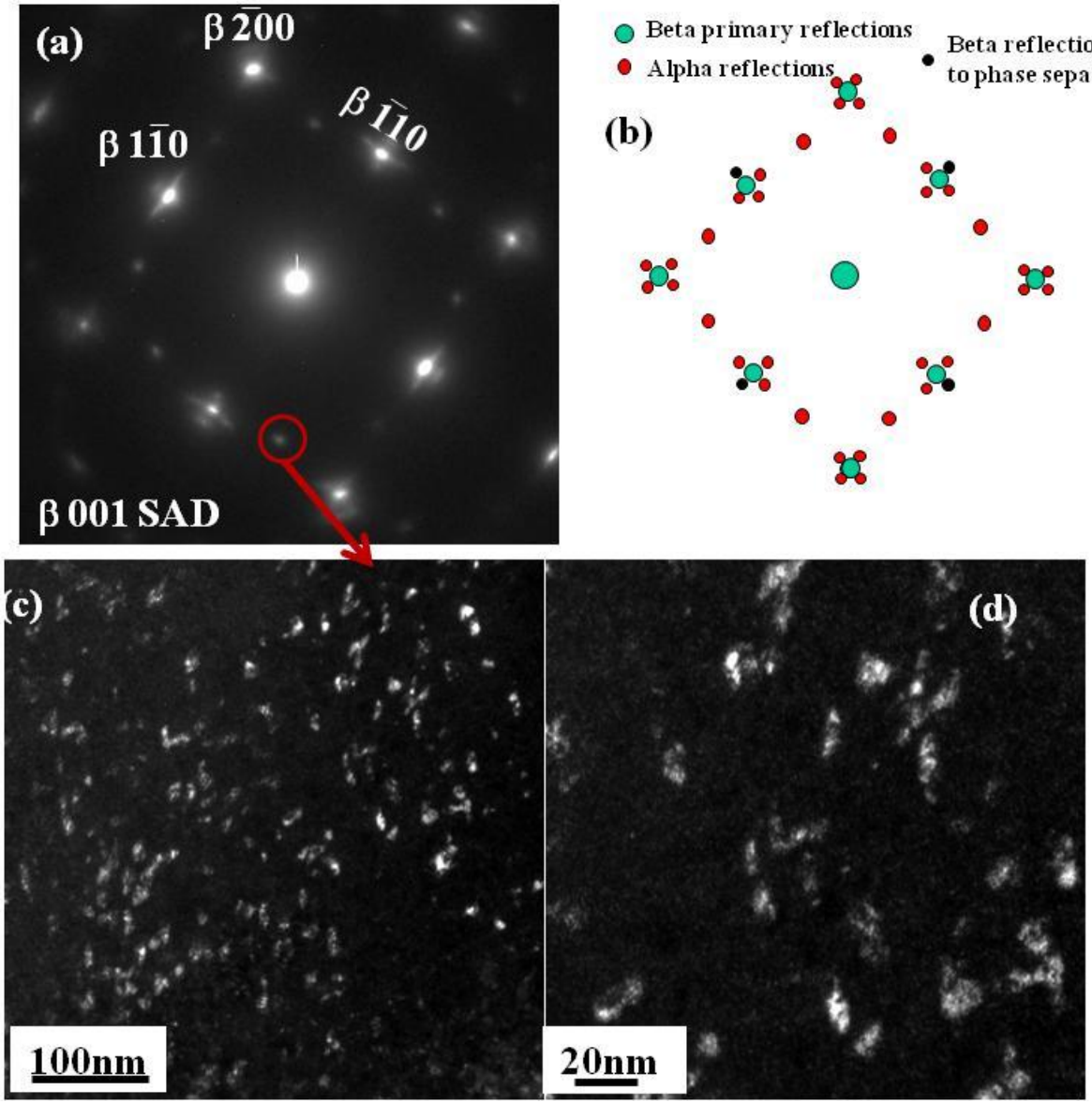

Fig. 6.6 (a) β <001> SAD electron diffraction from 400°C 10 hours aged condition with red circle showing the α reflection used to form the dark field image given in (c). (b) The simulated <001>β SAD considering all 12 variants of α and β phase separation. (d) High magnification view of bright contrast regions given in (c) showing a clearer view of the morphology.

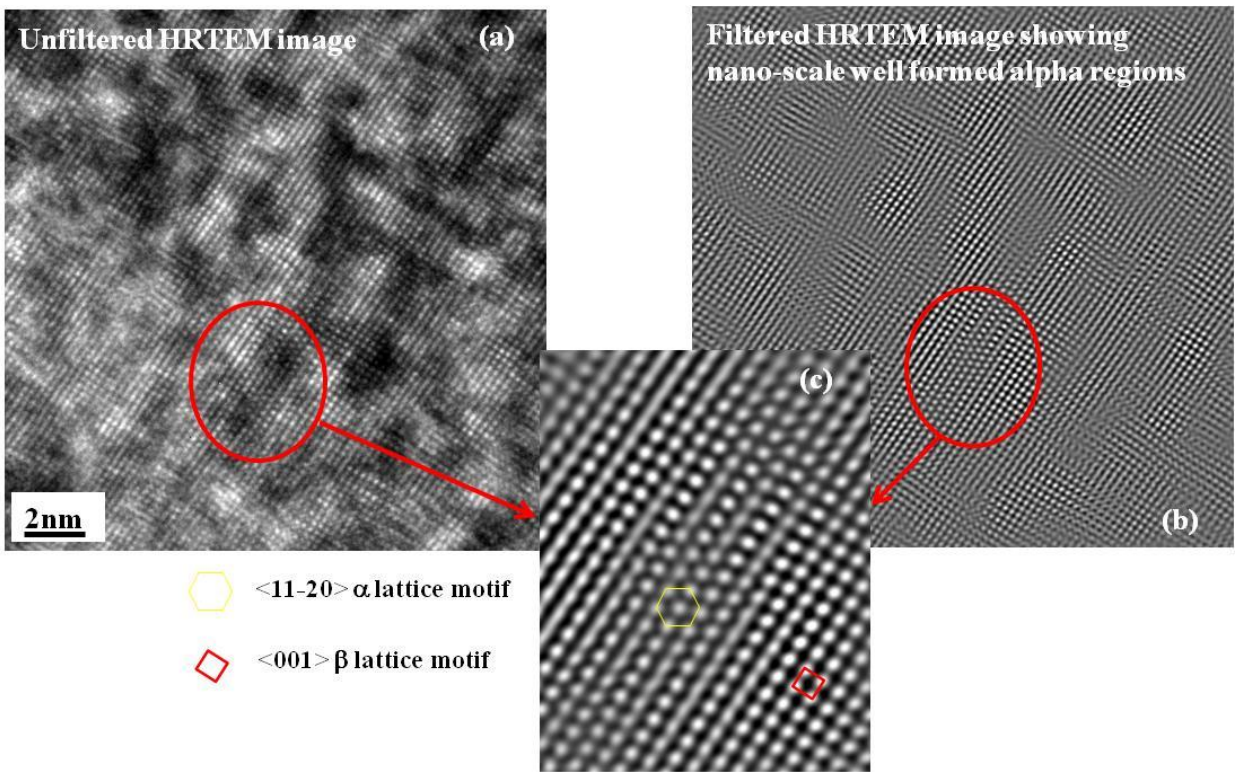

Fig. 6.7 (a) Unfiltered HRTEM image along β <001> beam direction from 400^{o}C 10 hours aged condition. The red circle shows the region given in (c). (b) Fourier filtered HRTEM image showing nano-scale α nuclei within the region marked by the red circle. (c) The region with α nucleus marked by the yellow hexagon and β<001> zone lattice marked by red square.

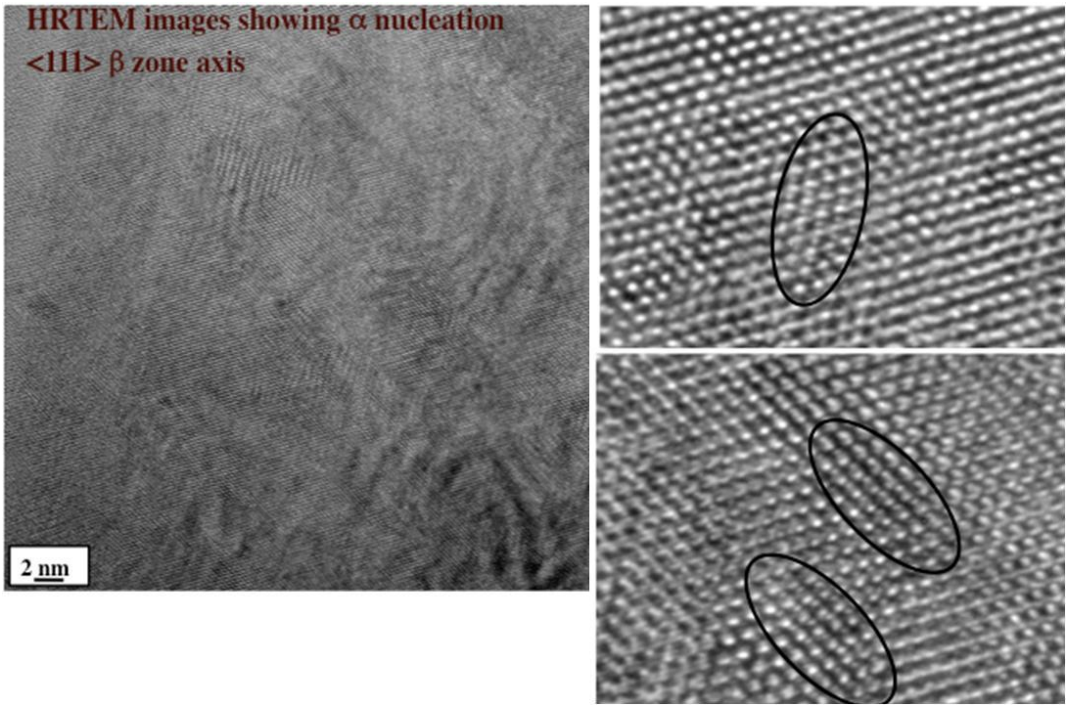

Fig. 6.8 (a) Aberration corrected HRTEM image along β <111> zone beam direction from 400°C 10 hours aged condition. (b), (c) magnified view showing three different a nuclei marked by the black ovals.

6.3.6 α Phase Precipitation in Ti-20Mo-5Al Alloy after Isothermal Ageing for 72 Hours at 400°C

Subsequently the isothermal ageing was continued to 72hours to investigate the development of morphology of α phase on long term ageing at 400°C. The TEM diffraction showed distinct α spots in the <110> β zone axis selected area diffraction pattern as shown in Fig. 6.9(a). A red circle is used to mark the specific α reflection used for forming the dark field image. The dark field image given in Fig. 6.9(b) shows the uniformly distributed star shaped clusters of multiple variants of α within the β matrix. A high magnification view of these clusters of multiple variants of α is shown in Fig. 6.9(c). Each of the α laths appears to be approximately 100nm long and 10nm thick. The slightly off zone bright field image is shown in Fig. 6.9 (d). This kind of periodic patchy α formation has been attributed to α nucleated by phase separation in past work on ternary additions to Ti-Mo alloys [7].

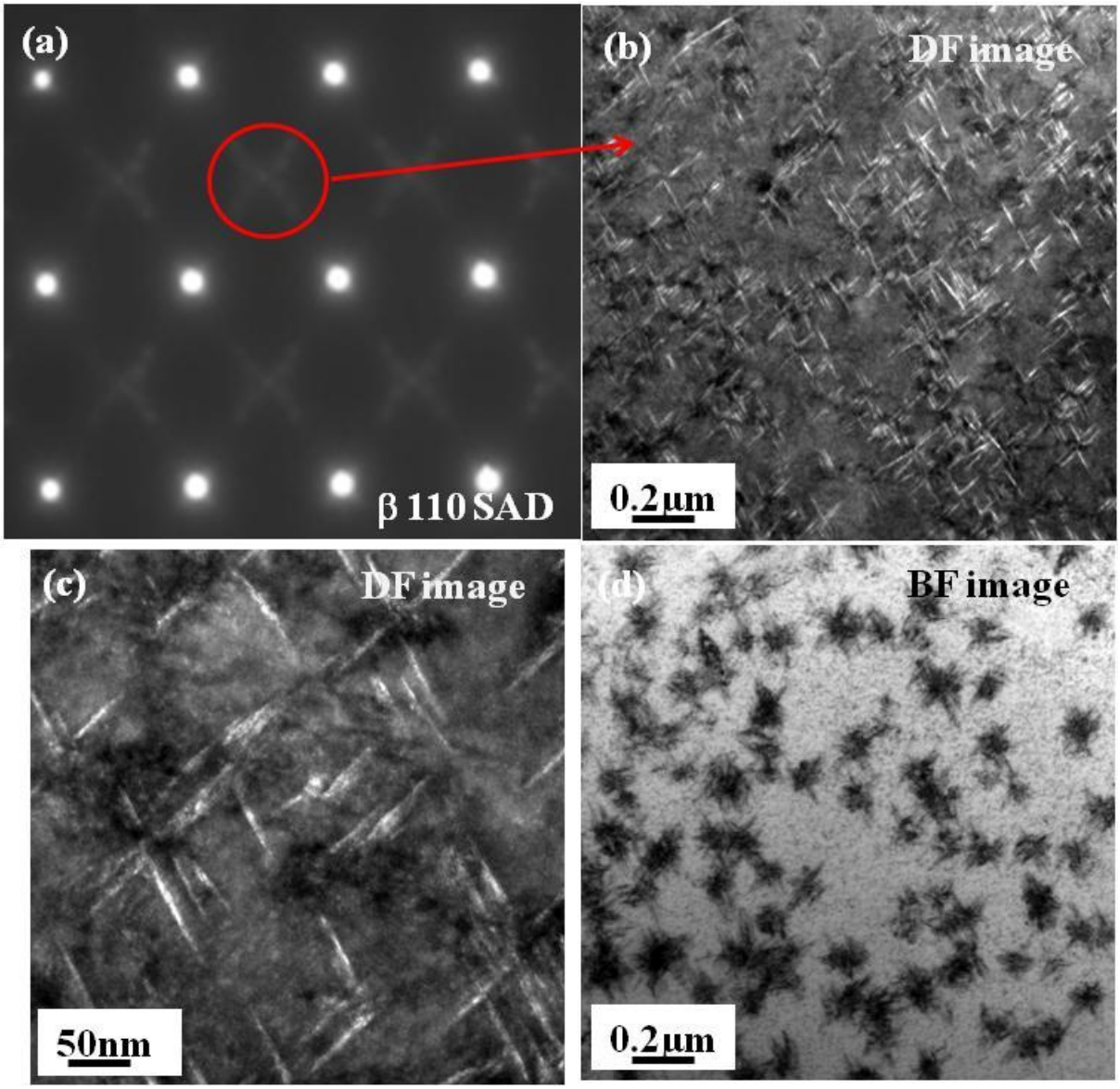

Fig. 6.9 (a). β <110> Selected area diffraction pattern from 400^{o}C 72hours aged condition with the red ellipse showing the α reflections used to form the dark field image given in (b). The dark field image showing the star shaped α clusters. (c) The magnified view of Fig. (b) clearly showing individual a clusters (d) bright field image of the region shown in (b) and (c).

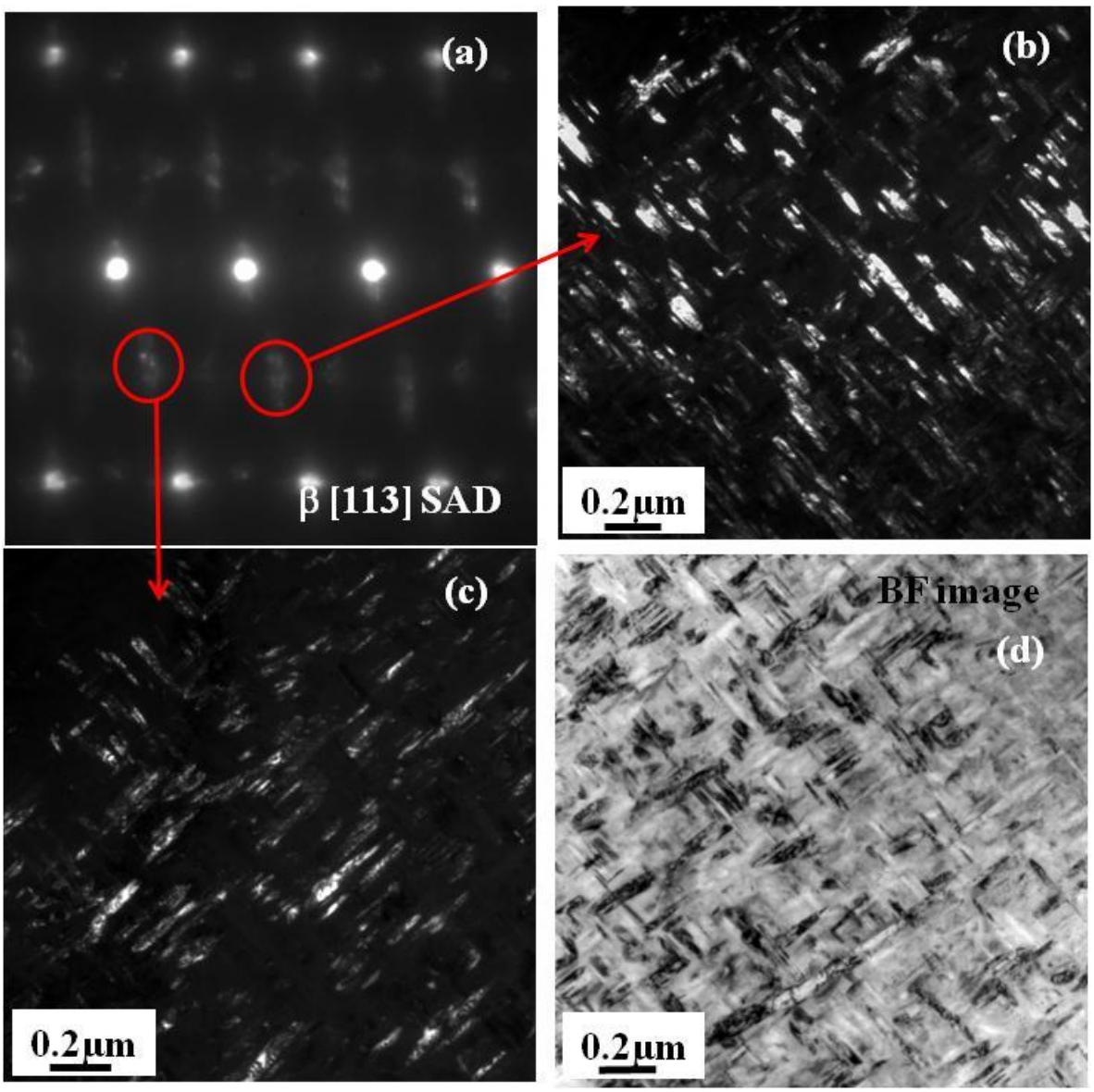

Fig. 6.10 (a). β<113> Selected area diffraction pattern from 620°C 1hour aged condition with red circles showing the alpha reflections used to form the dark field images given in (b) and (c). (d) The bright field image of the same region.

6.3.7 Growth of α Phase Precipitates in Ti-20Mo-5Al Alloy on Up Quenching to 620°C for 1 Hour

Subsequently the 400°C 72 hours aged sample was up-quenched to 620°C and held isothermally for 1hour followed by water quenching. The <113> β zone axis SAD diffraction pattern from the aged sample is shown in Fig. 6.10(a). Primary β reflections and additional α

reflections at ½{112} can be observed in the SAD pattern. The morphology of the α particles can be clearly seen in the dark field image formed by using the α reflections marked by the red circles. The two different variants of α contributing to the reflections are shown in Fig. 6.10 (b) and (c) respectively. The bright field image of the same region is shown in Fig. 6.10 (d). The α laths show substantial coarsening from the 400^{o}C 72hours aged condition. The α laths appear to be close to 100nm thick and almost 1 μm long. Also the volume fraction of α phase appears to have increased on 620^{o}C 1hour ageing.

STEM-EDS elemental mapping in TEM is a method to qualitatively estimate the compositional partitioning between phases [11]. Here we employed STEM EDS to evaluate the elemental partitioning between α and β phases in 400^{o}C/72hours aged condition. The STEM image of the regions analyzed for 400^{o}C/72hours aged condition is given in Fig. 6.11(a). The EDS mapping was done in the region marked with the red square, this region was chosen to include one complete cluster of α among the patchy α regions. The EDS elemental maps of Mo L and K are given in Fig. 6.11(b) and (c). Marginal depletion of Mo can be observed in the α region in comparison to the β regions. No distinct partitioning in Al or Ti is observable between α and β phases in Fig. 6.11 (d) and (e). To compare with this result the STEM-EDS elemental mapping was repeated for 620^{o}C 1hour up-quenched sample to analyze the elemental partitioning. Fig. 6.12 (a) shows the STEM image of the 620^{o}C 1hour aged sample. Two regions marked by red rectangles were used for EDS elemental mapping named as 1 and 2 in the image. The HAADF-STEM intensity map is given in Fig. 6.12(b) and (f) showing significant mass contrast between α and β phase. The Mo elemental maps given in Fig. 6.12(d) and (h) from the regions 1 and 2, show more pronounced partitioning in comparison to the 400^{o}C/72hours aged condition. Ti and Al elemental maps given in Fig. 6.12(c), (g) and (e), (i) only show a minor

extent of partitioning between α and β. However the overlap effects and the resulting composition smudging possible in STEM-EDS of such a sample with fine scale α precipitates in β matrix, should not be neglected. Even though STEM-EDS can provide qualitative information of solute partitioning, it is very difficult to quantify the solute partitioning accurately through this technique. Hence in order to quantify the elemental partitioning more accurately, a novel attempt was made to couple the crystallographic information obtained by diffraction and imaging in TEM with compositional information obtained from atom probe tomography.

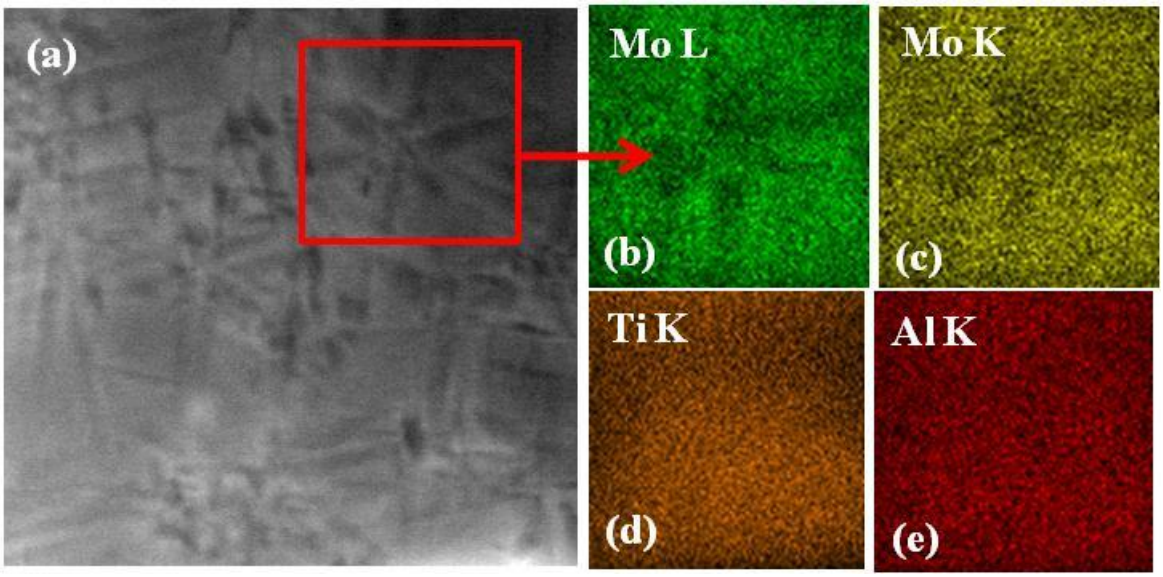

Fig. 6.11 (a). STEM image of 400oC 72hours aged condition showing the a clusters (b) Elemental maps of the same region given in (b) Mo L (c) Mo K (d) Ti K (e) Al K.

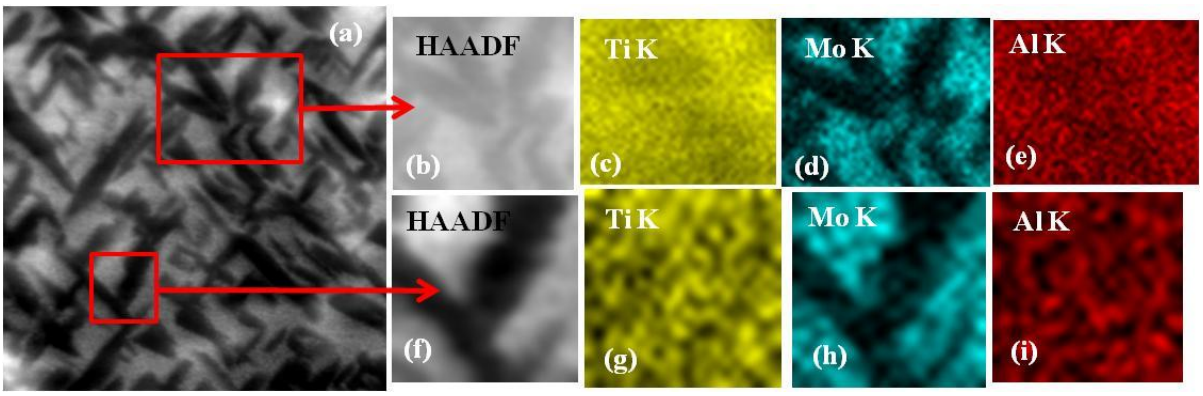

Fig. 6.12(a). STEM image of 620°C 1hour aged condition with two red rectangles showing the regions where STEM EDS mapping was performed. (b), (f) HAADF intensity maps of the regions 1 and 2. EDS Elemental maps of (c), (g) Ti K, (d), (h) Mo K, (e), (i) Al K of regions 1 and 2 respectively.

6.3.8 TEM-APT Coupling to Investigate Solute Partitioning Between α and β Phase

The needle shaped atom probe specimen of Ti5Al20Mo samples that was aged for 72 hours at 400°C were made on half cut Cu TEM grid posts using focused ion beam (FIB) technique as mentioned in section 3.4.3.3. The sample was loaded in the Tecnai™ F20 TEM immediately after the sample preparation in FIB to avoid any surface oxidation. TEM diffraction, bright field and dark field imaging of the tips are performed before loading the samples in the local electrode atom probe (APT). The low magnification TEM image of the half cut Cu grid is shown in Fig. 6.13 (a). Dark field imaging of the sample was performed using α reflections as previously described during the TEM analysis of the sample aged at 400°C for 72 hours. Fig. 6.13(b) shows the dark field image of the atom probe sample tip mounted on one of the Cu TEM grid posts. Multiple α variants can be clearly seen in the high magnification dark field image given in Fig. 6.14 (a). The tip diameter, shank angle and angle between the α laths seen in the image were measured. After the TEM analysis, the sample was loaded immediately into the load lock chamber of APT and subsequently transferred to the analysis chamber after attaining a vacuum level below 10^{-8} torr. The tips were field evaporated under voltage evaporation mode at

a temperature of 60K with 20% pulse fraction. The evaporation rate was maintained between 0.2 to 1%. The RHIT data after field evaporation was reconstructed using IVAS with 16nm tip diameter value and 12.8^{o} shank angle. The basics of IVAS reconstruction of atom probe data is given in section 3.4.6.1. Iso-concentration surfaces are a way to visualize the solute partitioning within the atom probe data. Such an iso concentration surface created using 89 at% Ti is shown in Fig. 6.14 (b). The remarkable correspondence between the morphology of α laths in the prior evaporation dark field image and the iso-concentration surface view help to conclusively identify the α lath regions in the reconstructed volume. Thereafter different methods of measuring the composition of individual phases were employed to quantify the composition of α and β phases accurately. The composition of three α laths and β region were estimated by fitting an ellipsoid of 20nm x 6nm x 5nm, within the α lath regions and in the inter lath β regions. The iso-concentration surface view of the three α laths and β region with fitted ellipsoid is shown in Fig. 6.15 (a)-(d). The average concentration of α regions obtained by ellipsoid fitting was 90.75% Ti-1.73% Mo-7.51% Al (all in at%) and the β concentration obtained was 84.27% Ti- 7.78% Mo-7.94% Al (all in at%). Significant partitioning in Mo and very less partitioning in Al is observed reconfirming the results obtained by STEM-EDS elemental mapping. While fitting the ellipsoid care was taken to keep the ellipsoid away from any interfaces and well within the α and β regions. The composition of α and β phases were also estimated using a technique of calculating the bulk composition from an extracted higher gradient and lower gradient pos file for 87% Ti iso-surface at which α precipitates are clearly visible. The higher gradient pos file exported for 87% iso-surface is shown in Fig. 6.15 (e). The average composition of α phase estimated from the higher gradient pos file was 89.88% Ti-3.34% Mo-6.77% Al, and the average composition of β phase estimated from lower gradient pos file was 82.68% Ti-9.48% Mo-7.82% Al (all in at%).

This technique also indicated a large extent of partitioning in Mo and very low partitioning in Al between α and β phases. A third technique of proximity histogram was employed to estimate the near interface solute partitioning at the α/β interface defined using 86% Ti iso-concentration surface as shown in Fig. 6.16 (a). The proximity histogram is plotted with distance across the interface on x axis and composition of Mo and Al on y axis as shown in Fig. 6.16(b). This technique also shows a pronounced degree of partitioning in Mo and very low partitioning in Al across the α/β interface. Thus similar results obtained from STEM-EDS mapping was obtained using three techniques of analyzing the composition of α and β phase in atom probe data. This result is contradictory to the conventional wisdom of expecting a larger compositional partitioning in a fast diffusing α stabilizing element Al and lower partitioning in slow diffusing β stabilizing element Mo. This motivated the attempt to quantify the solute partitioning after 1hour aging at even higher temperature of 620^{o}C.

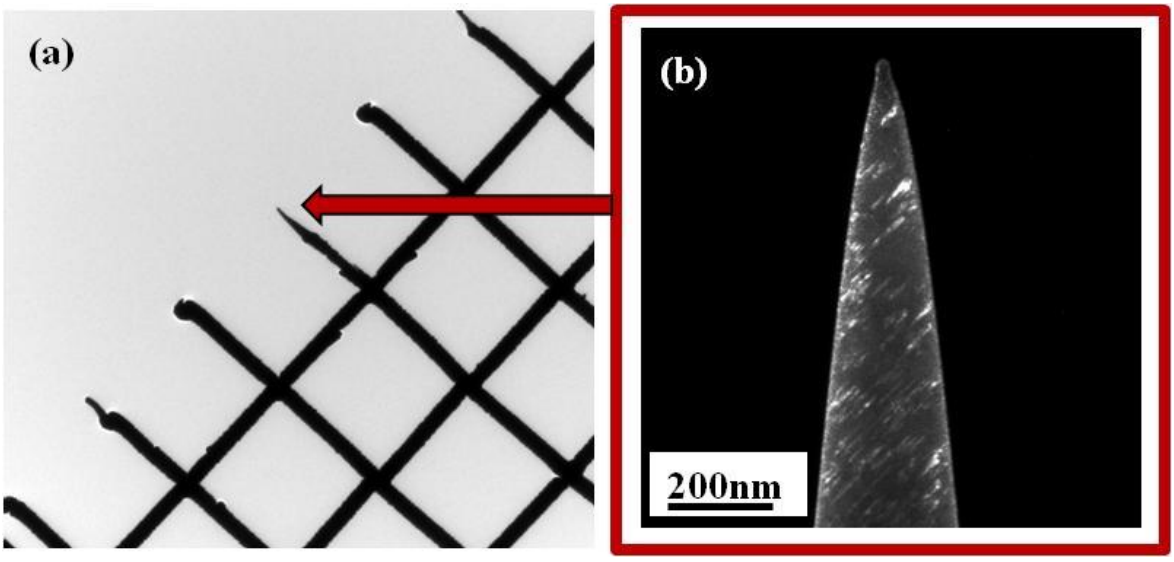

Fig. 6.13 (a). TEM low magnification view of half cut Cu grid with samples (b) Dark field image of the sample tip of 400^{o}C 72 hours aged condition.

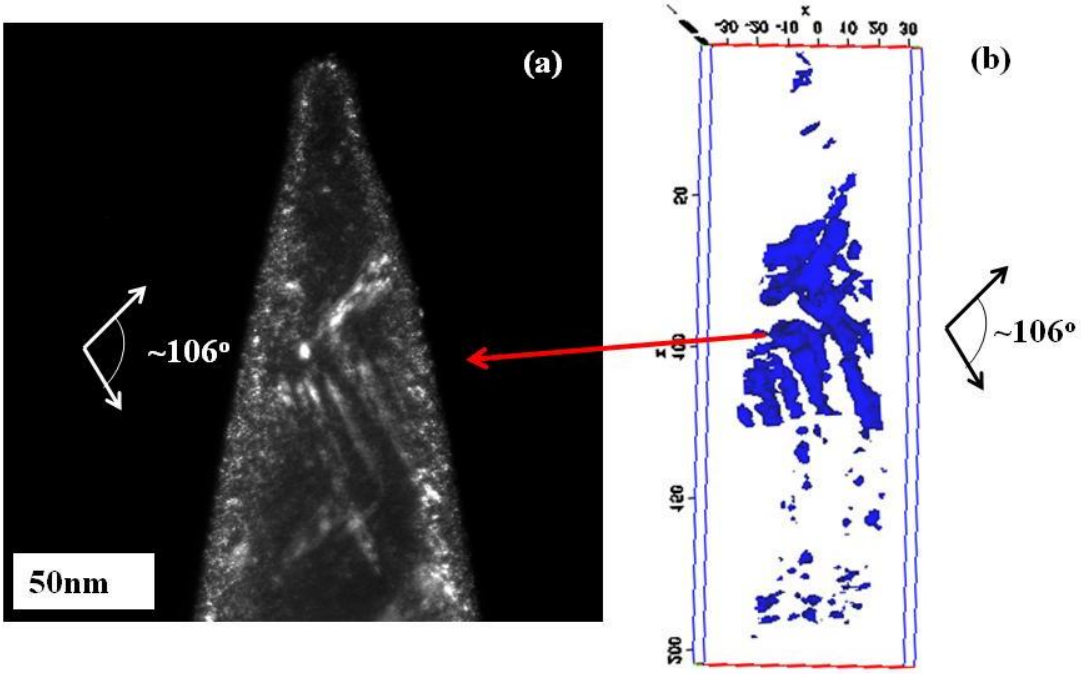

Fig. 6.14 (a). Dark field image of the 400°C 72hours aged condition atom probe tip showing the α cluster oriented with 106° angle (b) The 89% Ti iso-concentration surface view of the final atom probe data reconstruction showing the a cluster with 106° agle.

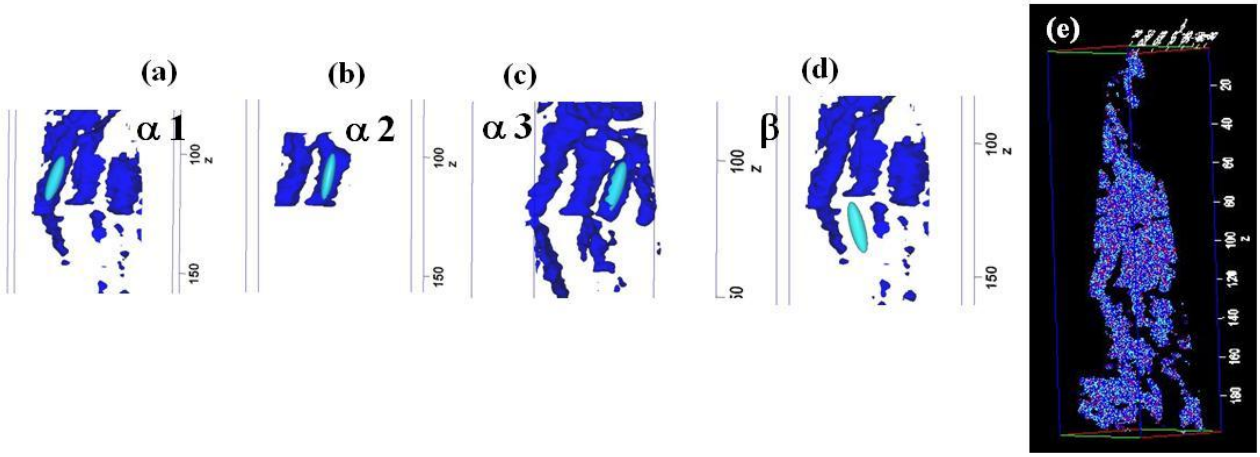

Fig. 6.15. 20nm x 6nm x 5nm ellipsoid fitted in (a) a1 (b) a2 (c) a3 and (d) b regions of the reconstruction to estimate the composition (e) Ionic view of higher gradient POS file showing the alpha regions within the reconstruction.

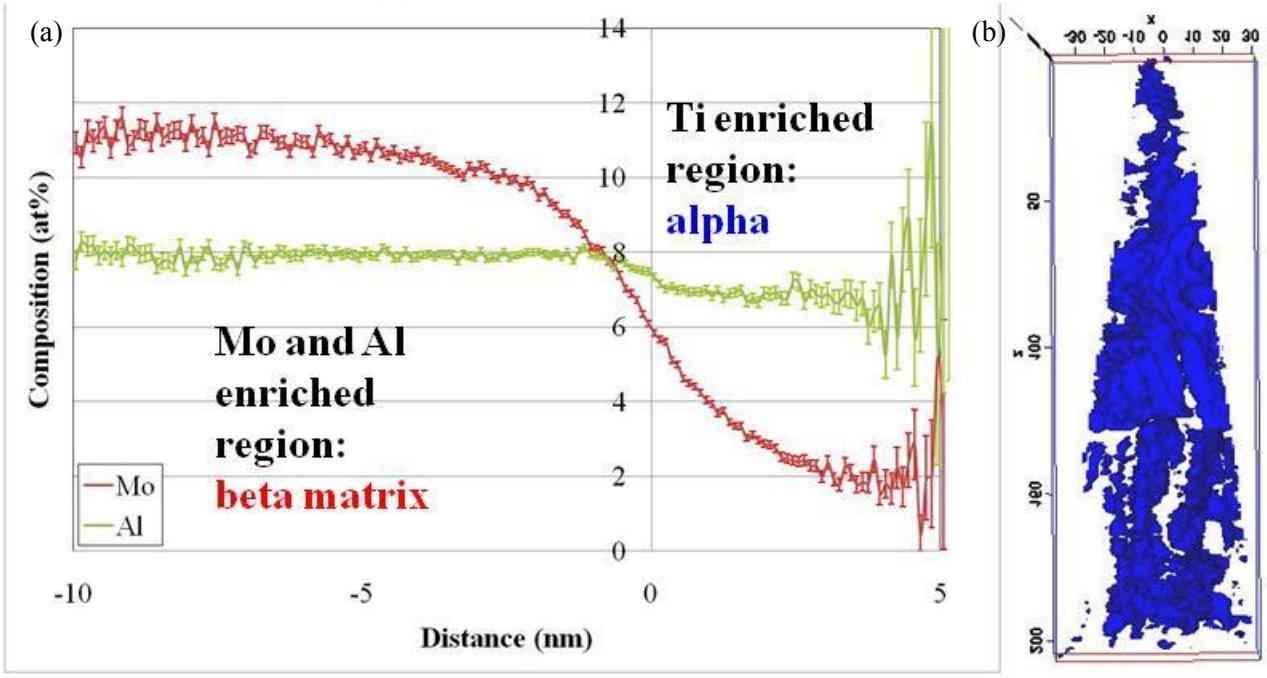

Fig. 6.16 (a). Proximity histogram across 86% Ti iso-surface showing Mo and Al partitioning across the α and β interface (b) corresponding 86% Ti iso-concentration surface view of the α regions.

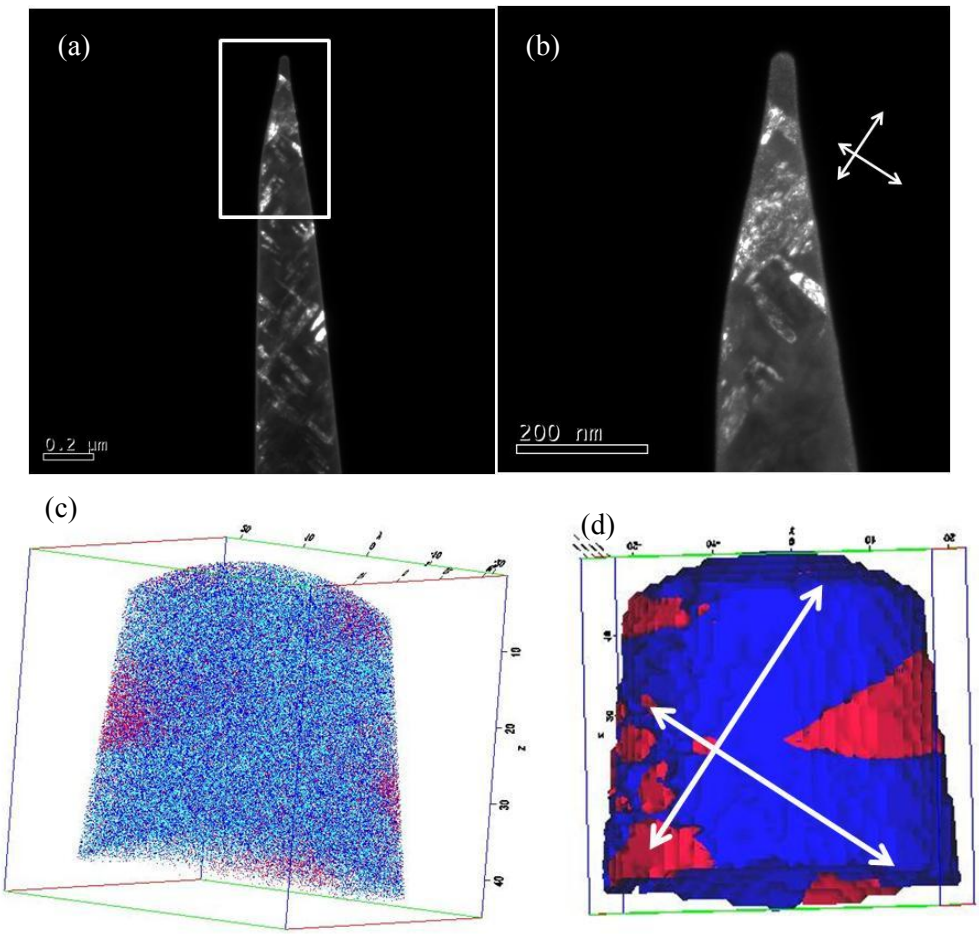

Fig. 6.17(a) Low magnification Dark field image of the TEM-APT coupling sample tip of 620^{o}C 1hour aged condition with white rectangle showing the region magnified (b) The high magnification tip view showing the geometry of a precipitates. The two white arrows are given to show the general α morphology observed on the tip (c) The ionic view of a part of the reconstruction obtained from the tip showing clustering of Mo atoms and Al atoms (d) the lower gradient filled iso-concentration surface view for 86% Ti and 6% Mo showing the same morphology of α plates as in the tip. The morphology of α plates are highlighted by the white arrows.

The low magnification TEM dark field image of the tip for 620^{o}C 1hour aged sample is given in Fig. 6.17(a). The region shown by the white rectangle in Fig. 6.17(a) is shown magnified in the high magnification dark field image given in Fig. 6.17(b). The characteristic morphology of multiple variants of intersecting α laths within the sample tip is represented by the two arrows shown in Fig. 6.17(b). As mentioned before, this geometrical relationship between different variants of α laths, tip diameter and shank angle of the tip were recorded for

using as inputs to IVAS reconstruction explorer. Subsequently the sample was analyzed in voltage evaporation mode at 60K with 20% pulse fraction. The data collected from atom probe analysis was reconstructed using the tip diameter and shank angle obtained by the TEM analysis. The ionic view of the reconstruction is shown in Fig. 6.17(c) with Ti ions in dark blue, Mo ions in red and Al ions in light blue color. Significant segregation of Mo and Al atoms can be noticed from the ionic view of the data. For a better visualization of α and β regions, lower gradient filled iso-concentration surfaces of 83% Ti and 7% Mo were used as shown in Fig. 6.17(d). A similar morphology of intersecting α laths as observed from the dark field image can be seen in the iso-concentration surface view given in Fig. 6.17(d). The white arrows drawn along the α laths in Fig. 6.17(d) confirm this geometrical relationship. Proximity histogram was plotted to quantify the solute partitioning across the α/β interface defined using 83at% Ti iso-concentration surface. Fig. 6.18 shows the proximity histogram of Mo and Al across such an interface showing an enrichment of Al in the Ti enriched α regions. The corresponding plot with Ti is shown in the inset given in Fig. 6.18. However the reconstruction had very low volume fraction of beta region resulting in higher error bar values in beta region of the reconstruction. For better statistics APT samples of the same heat treatment condition where made and independently analyzed in voltage evaporation mode. The ionic view of such a reconstruction is shown in Fig. 6.19(a) where Ti atoms are shown in dark blue, Mo atoms in red and Al in light blue. The ionic view clearly shows segregation of Al ions and Mo ions to specific regions. The entire reconstruction consisted of 13 million ions. A low gradient filled iso-concentration surface view using 86% Ti and 6% Mo helps in clearly visualizing the α and β regions in the reconstructed volume. The blue regions denote the α laths and red regions correspond to the β matrix in between the α laths. Proximity histogram for Mo and Al atoms made across an interface created by 86at% Ti iso-

surface describing the interface of an α lath with β matrix is shown in Fig. 6.20. The inset shows the entire proximity histogram of Ti, Mo and Al atoms. The proximity histogram shows considerable enrichment of Al in the Ti enriched region corresponding to α lath. This reconfirmed that annealing the sample that was aged at 400°C for 72hours at higher temperatures (600°C for 1hour) does help in enriching the α precipitates with Al.

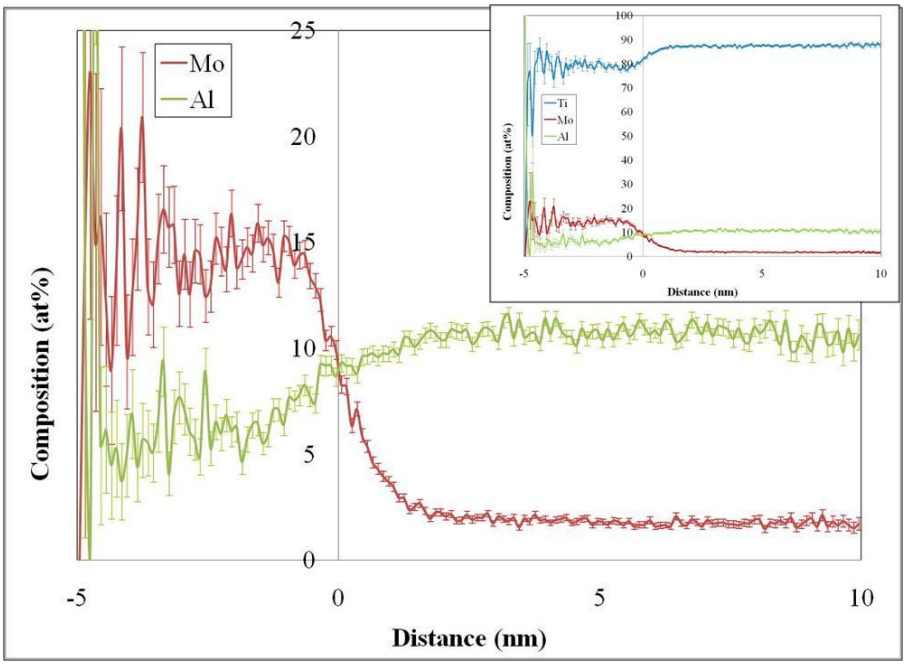

Fig. 6.18(a) Proximity histogram of Mo and Al across a Ti 86 at% iso-concentration surface showing the elemental partitioning between α and β phases. The inset shows the Ti atom partitioning along with Mo and Al.

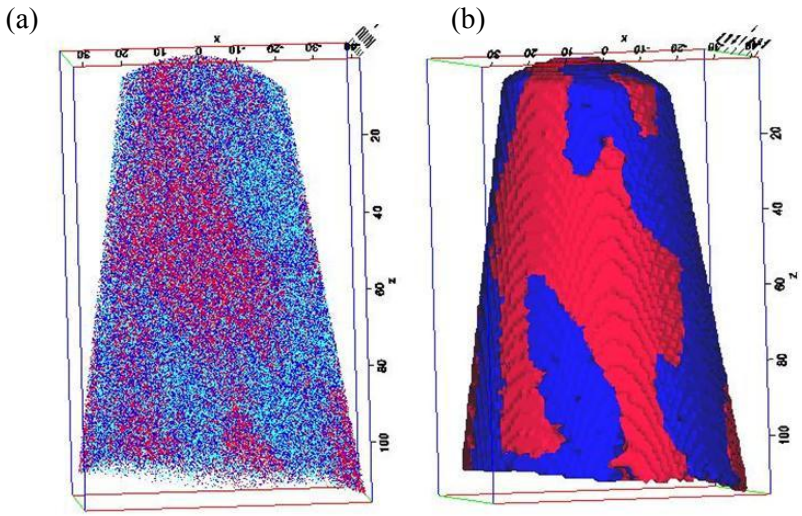

Fig. 6.19(a). Ionic view of the atom probe data showing clustering of Al and Mo to α and β phase regions in 620°C 1hour aged sample. (b) The α and β phase regions visualized by low gradient filled view of 86 % Ti and 6% Mo iso-concentration surface.

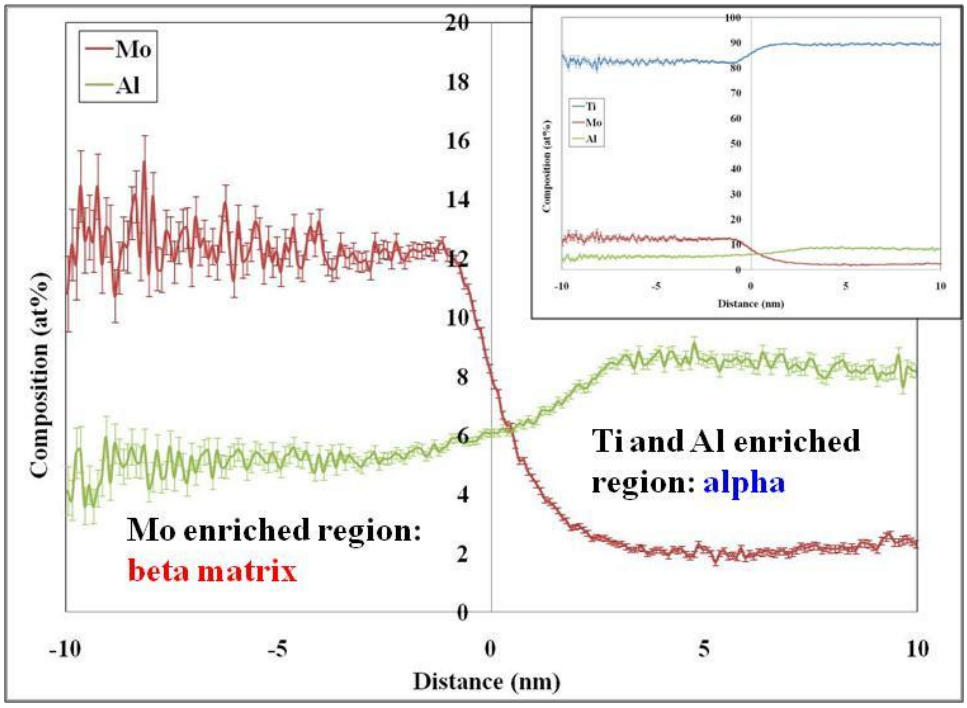

Fig. 6.20(a). Proximity histogram across an 86% Ti iso-concentration surface showing Mo and Al partitioning across the α/β interface. The inset shows the Ti partitioning also in addition to Mo and Al.

6.3.9 APT Analysis of Solute Partitioning During β Phase Separation and Subsequent Nucleation of α

Atom probe tomography analysis of 400^{o}C/6hours and 400^{o}C/10hours aged conditions were carried out to understand the earlier stages of solute partitioning during phase separation and initial stage of nucleation of α. Fig. 6.21(a) shows the ionic view of the reconstruction of 400^{o}C/6hours aged condition. An iso-concentration surface plotted using 83% Ti showed distinct regions of Ti enrichment as shown in Fig. 6.21(b). The corresponding proximity histogram using Mo and Al is shown in Fig. 6.21(c). The inset Fig. also shows the Ti partitioning across the chosen interface. As per the given proximity histogram, a depletion of both Mo and Al can be observed to occur in the Ti enriched regions (shown in Fig. 6.21(b)). The extent of Mo and Al partitioning was quantified by calculating the difference between steady state composition in Ti rich and Ti depleted regions from the proximity histogram. Care was also taken to keep the error bars appreciably low while estimating the steady composition on either side of the interface. While the average Mo and Al composition obtained from the proximity histogram in Ti depleted region was estimated at a distance of 3-5nm to the left of the interface, those in Ti rich region was estimated at a distance of 0.15 to 0.95nm to the right of the interface. Based on that calculation Mo was 3.4at% higher and Al was 2.4at% higher in the Ti depleted region in comparison to the Ti rich region.

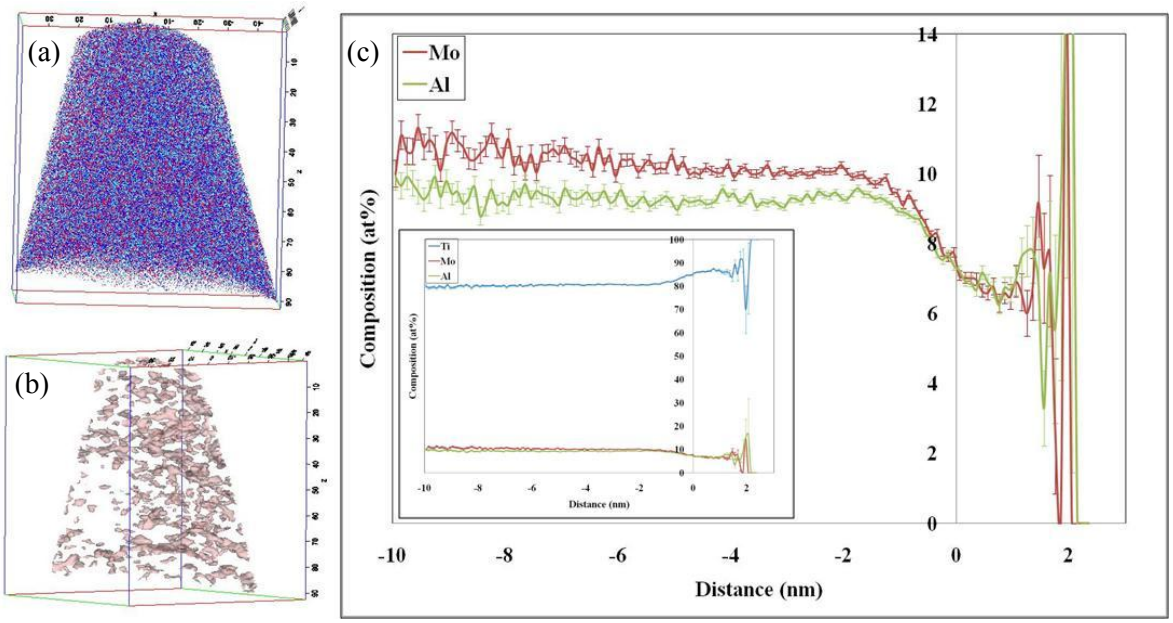

Fig. 6.21 (a) Ionic view of 400°C 6 hours aged condition where Ti atoms are shown in dark blue, Mo atoms in red, and Al atoms in light blue. (b) The 83% Ti iso-concentration surface view showing regions rich in Ti within the reconstructed data (c) Proximity histogram across an 83% Ti iso-concentration surface showing Mo and Al partitioning between the Ti rich regions and the matrix. The inset shows the Ti partitioning also in addition to Mo and Al.

Atom probe analysis of 400°C 10hours aged condition was performed to understand the progress of phase separation on subsequent ageing from 6 hours. Fig. 6.22(a) shows such a reconstruction of 10 hours aged Ti20Mo5Al alloy at 400°C. The total number of ions in the reconstruction was 10.8 million. Fig. 6.22(b) shows the 86 at% Ti iso-concentration surface revealing some possible crystallographic alignment of the Ti enriched regions. The compositional partitioning across such an interface was estimated using proximity histogram shown in Fig. 6.22 (c). The overall Ti, Mo and Al proximity histogram is shown as an inset in the Fig. The 10 hours aged condition also showed a Ti enriched region depleted in Mo and Al, similar to 6 hours aged condition. While the average Mo and Al composition obtained from the proximity histogram in Ti depleted region was estimated at a distance of 3-5nm to the left of the interface, those in Ti rich region was estimated at a distance of 0.75-1.55nm to the right of the

interface. Using such a calculation the Mo enrichment in Ti depleted region was observed to increase to 3.8at% and Al was observed to increase to 2.6at% resulting in a higher degree of solute partitioning in 10 hours aged condition.

In a similar manner the difference in steady state composition of Mo and Al in Ti depleted region to Ti enriched region was calculated for different samples that were aged at 400^{o}C for 6, 10 and 72hours and 620^{o}C for 1hour. This was done in order to better understand the progressive compositional partitioning. The table of the elemental partitioning estimated from the proximity histogram data is given in Table 6.1. The bar chart plotted in Fig. 6.23(a) shows the variation in Mo and Al enrichment in Ti depleted region with ageing. The magnitude of Mo and Al enrichment in Ti depleted region in 6 hours aged condition seems to have increased by 10 hours of ageing. On further ageing up to 72hours only Mo seems to have enriched further in Ti depleted regions, where as Al seems to have partitioned to a lower extent than in 10 hours of ageing. On further aging at a higher temperature of 620^{o}C for 1hour, Al appears to have enriched in Ti enriched regions. Highest Mo partitioning is observed in 620^{o}C 1hour aged condition in comparison to any other prior heat treatment condition.

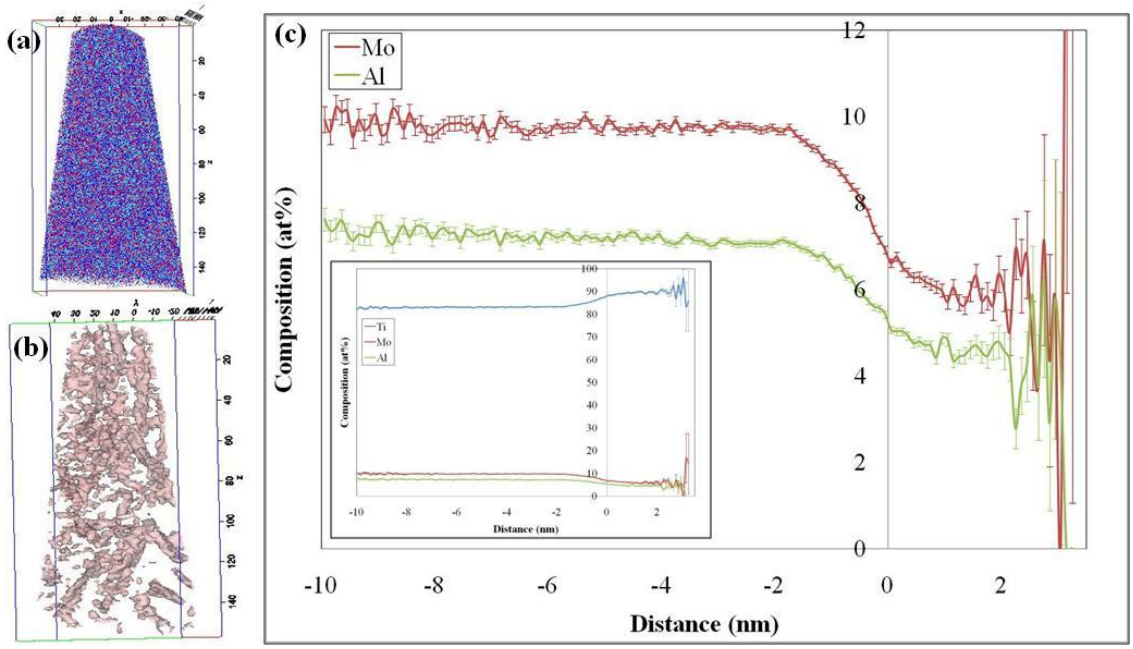

Fig. 6.22(a) Ionic view of 400^{o}C 10 hours aged condition where Ti atoms are shown in dark blue, Mo atoms in red, and Al atoms in light blue. (b) The 86% Ti iso-concentration surface view showing crystallographically aligned Ti rich regions rich within the reconstructed data (c) Proximity histogram across the 86% Ti iso-concentration surface showing Mo and Al partitioning between the Ti rich regions and the matrix. The inset shows the Ti partitioning also in addition to Mo and Al.

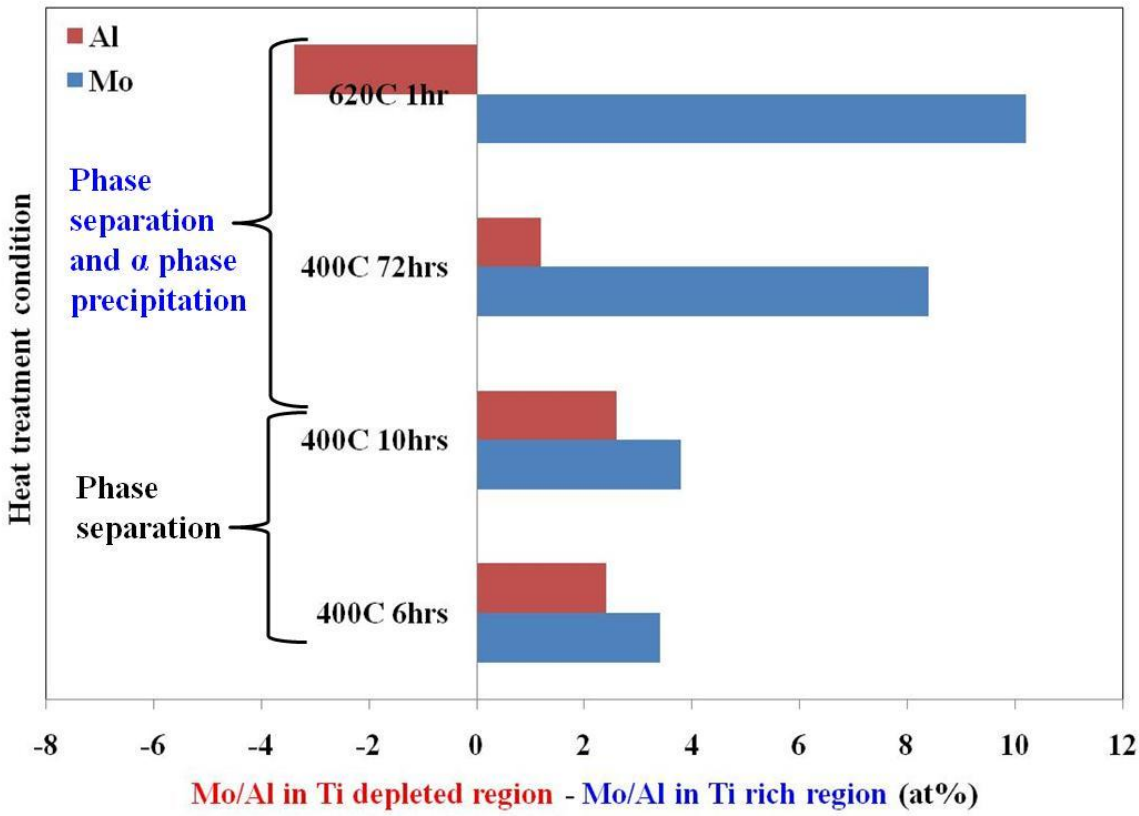

Fig. 6.23(a) Bar chart of table 6.1 showing the variation in Mo an Al enrichment in the Ti depleted region with ageing. X axis is the difference between Mo or Al concentration in Ti depleted region and Mo or Al in Ti rich region.

HT	Mo	Al
400C 6hrs	3.4	2.4
400C 10hrs	3.8	2.6
400C 72hrs	8.4	1.2
620C 1hr	10.2	-3.4

Table 6.1 The table of difference in Mo/Al composition between Ti depleted β2 regions and Ti rich β1 regions.

6.3.10 Mechanism of β Phase Separation and Subsequent α Phase Nucleation in Ti20Mo5Al Alloy

With all the experimental evidence an attempt is made to conclusively identify the mechanism of β phase separation and subsequent α phase precipitation in Ti20Mo5Al alloy. The in-situ ageing X-ray diffraction experiments point to a progressive development of {200}β peak

split from 5 hours to 10 hours of ageing at 400^{o}C along with a progressive increase in intensity of {10-12} α peak. The straining of β lattice observed in β<001> zone axis high resolution TEM image also confirm the presence of two regions with two different lattice parameter values within the 400^{o}C/6 hours aged condition. The early stages of α nuclei observed in the aberration corrected HRTEM images of 400^{o}C 10hours aged condition might be attributed to the ones contributing to the higher intensity of $\{10\bar{1}2\}$ α reflection in the X-ray diffraction spectrum. The corresponding proximity histogram from the atom probe data of the heat treated samples distinctly capture the solute depleted (Ti rich: Mo and Al depleted) and solute rich (Mo and Al enriched) regions present in the 6 hours and 10 hours aged condition. In this discussion the solute depleted (Ti enriched: Mo and Al depleted) zones will be called as β_1 and solute rich (Mo and Al enriched) regions will be called as β_2 for convenience. The size scale of Ti rich β_1 regions and the partitioning of Mo and Al across such an interface are found to increase on ageing from 6 hours to 10 hours at 400^{o}C. The observation of crystallographically well formed α nuclei in 400^{o}C/10hours aged condition along with the observation of solute depleted β_1 regions as per proximity histogram data from atom probe analysis, point to the possible nucleation of α precipitates within these solute depleted β_1 regions formed by prior β phase separation. Subsequently the TEM-APT coupling studies undertaken in 400^{o}C/72hours aged condition prove that the α precipitates in such a condition are also solute depleted in nature with a significant depletion in Mo and a lower extent of depletion of Al in comparison to the matrix. Eventually the higher temperature ageing at 620^{o}C for 1hour lead to a reversion in Al partitioning across the α and β interface as evident from the atom probe tomography data of Al enrichment within the α precipitates. The observation of substantially lower extent of Al partitioning and eventual reversion in Al between α and β matrix point to the possibility of back diffusion of Al into the α

precipitates nucleated in the β1 regions formed by phase separation. This can be explained based on the lower chemical potential of the α stabilizing element Al in α phase than in β phase. Therefore based on the quantitative compositional partitioning information and diffraction and imaging information the β phase separation in this ternary Ti-20Mo-5Al alloy can be said to form solute depleted (Ti rich, Mo and Al depleted) β_1 and solute rich β_2 regions (Ti depleted, Mo and Al rich) followed by nucleation of α phase in solute depleted β_1 regions (Ti rich regions). After α nucleation Al being an α stabilizer diffuses back into the α phase, eventually leading to a reversion in Al profile in comparison to the phase separated condition observed in 10 hours of ageing at 400^{o}C. These findings point to a unique mechanism via which phase separation and subsequent a nucleation and growth can occur in this alloy system. However further work needs to be conducted to conclude the mechanism more accurately.

6.4 Summary

Ti-20Mo-5Al alloy undergoes a coherent phase separation reaction forming solute lean (β_1) and solute rich (β_2) regions on isothermal ageing at 400^{o}C. Both Al and Mo segregate to β_2 regions leaving β_1 to be predominantly rich in Ti. On ageing from 6 hours to 10 hours the extent of solute partitioning between β_1 and β_2 phases increases with a concurrent increase in size scale of β_1 regions as evident from the atom probe data. Based on the observation of a solute lean nature of α phase in 72 hours aged condition it can be said that α phase precipitation occurs in the solute depleted β_1 regions created by phase separation. However after α precipitation, Al starts to diffuse from β_2 regions to α regions reducing the extent of solute partitioning of Al. On continued ageing at 620^{o}C for 1hour Al appeared to preferentially partition in to the α phase. The presence of an α stabilizing element Al thus helped in uniquely identifying the β phase

separation and subsequent α phase nucleation on isothermal ageing. Interestingly unlike Al, Mo continues to partition during longer term ageing even after the onset of α phase precipitation.

6.5 References

[1] Abyzov AS, Davydov LN, Mchedlov-Petrosyan PO, Schmelzer J. Physica A 1999;272:459.

[2] http://goldbook.iupac.org/P04534.html.

[3] Porter and Easterling

[4] Kaufman L, Bernstein H. The Science Technology and Application of Titanium 1970:361.

[5] Koul MK, Breedis JF. Acta Met 1970;18:579.

[6] Hoch M, Viswanathan R. Met. Trans 1971;2:2765.

[7] Blackburn MJ, Williams JC. Trans. TMS-AIME, 1968;242:2461.

[8] Chandrasekaran V, Taggart R, Polonis DH. Metallography 1972;5:393.

[9] Furuhara T, Makino T, Idei Y, Ishigaki H, Takada A, Maki T. Mater trans, JIM 1998;39(1):31.

[10] Collins PC, Banerjee R, Banerjee S, Fraser HL. Mat. Sci. and Engg 2003;A352:118.

[11] Doig P, Flewitt PEJ, Met. And mat. Transc. A 1983;14(10):1943.

[12] Williams JC, Hickman BS, Leslie DH. Met. and Mater Transact. B 1971;2(2):477.

CHAPTER 7
PHASE SEPARATION AND ω PHASE FORMATION IN BETA MATRIX OF Ti-10V-6Cu ALLOY

7.1 Introduction

The present study focuses on the competing processes of phase separation (or the development of compositional modulations) within the β phase and the β to ω phase transformation in a ternary Ti-10V-6Cu (wt. %) alloy under two different conditions. One set of samples has been water quenched followed by short-term isothermal aging, while a second has been air cooled from the high temperature single β phase field. An important aspect of the present system, deserving of emphasis, is that the alloy contains two β-stabilizers of very different nature. Vanadium is a monotectoid-type (classically, also referred to as isomorphous) stabilizer, while copper is a eutectoid-type stabilizer [1]. Consequently, V exhibits extensive solid solubility in β-Ti and forms $\alpha_{V\text{-}lean}+\beta_{V\text{-}rich}$ microstructures upon decomposition, while Cu has a tendency to form intermetallic compounds with Ti, and Ti-Cu alloys of low Cu content typically exhibit $\alpha+Ti_2Cu$ microstructures. In addition, both the binary Ti-V and Ti-Cu systems exhibit strong tendencies for phase separation within the β matrix via either homogeneous or heterogeneous fluctuations (i.e. spinodal decomposition versus nucleation and growth). Consequently, the Ti-V-Cu ternary system offers a unique opportunity in terms of investigating the interaction between V and Cu in the Ti matrix on β phase separation (compositional modulation) and formation of the ω phase.

7.2 Experimental Procedure

An alloy of nominal composition Ti-10V-6Cu (wt%) was arc melted from high-purity elemental components under argon atmosphere, with residual oxygen and nitrogen gases in the chamber removed by melting a titanium getter before alloy preparation. The alloy was re-melted

six times to ensure thorough mixing of components and the final alloy button was encapsulated in quartz tube, back-filled with 0.33 atmos. pressure of argon, for heat treatment. Solution heat treatment was carried out in an air furnace at 1100°C for 48h, followed by either a water quench (WQ) or air cooling (AC) to room temperature. The cooling rate in air was measured to be an average 8.5°Cs^{-1} in the range of 1100°C to 500°C and significantly less than 1°Cs^{-1} below 500°C. The water quench rate was estimated to be in excess of 500°Cs^{-1}. The alloy composition (wt %) determined by spectroscopic chemical analysis was as follows:

Ti	V	Ni	Cu	Fe	Al	Zr	Sn
Bal.	10.10	<0.01	6.08	0.03	0.02	<0.01	<0.01

Subsequent aging treatments were carried out in a salt bath at 500°C. Specimens for transmission electron microscopy (TEM) were prepared by Argon ion beam milling in a Gatan PIPS from mechanically dimpled thin foils (~50 μm thick) at an anode voltage of 5keV, followed by end polishing at 2keV. Philips CM20 and JEOL 2100F transmission electron microscopes (TEM), operating at 200kV, were employed for microstructural examination.

Samples for atom probe tomography (APT) were prepared using a dual-beam focused ion beam (FIB) instrument and procedures are described in detail in section 3.4.3.2. Subsequently, these samples were field-evaporated in the APT system, which is a local electrode atom probe (LEAP™) system from Imago Scientific Instruments, using the electric-field evaporation mode at a temperature of 70K, with an evaporation rate of 0.2 – 1.0% and a voltage pulse fraction at 20% of the steady-state applied voltage.

7.3 Results

7.3.1 Solution Heat Treated and Water Quenched Ti-10V-6Cu

Transmission electron microscopy (TEM) results from the WQ Ti-10V-6Cu alloy are shown in Fig. 7.1. The selected area diffraction (SAD) pattern from this sample, recorded along the <011> zone axis and shown in Fig. 7.1(a), clearly exhibits both fundamental reflections arising from the β matrix as well as additional reflections at the 1/3 and 2/3 {112} positions, attributable to the ω phase. A dark-field TEM image, Fig. 7.1(b), from the as-quenched sample, recorded using one of the ω reflections, reveals sub- 10nm scale ω domains, uniformly distributed throughout the β matrix. The domains represent one of four possible variants of the ω phase in this β crystal and appear to exhibit a near-equiaxed (spheroidal or ellipsoidal) morphology, although the relatively fine scale (~2-5nm) makes it rather difficult to determine the morphology uniquely. A high resolution TEM image of the same sample, viewed along an $<011>_{\beta}$ axis, is shown in Fig. 1(c). The early stages of formation of ω are visible in the inset, where the β the ω motifs have been highlighted using small and large rectangles respectively. The structure of the cell defined by the ω motif in the high-resolution TEM image indicates an incomplete collapse of $[111]_{\beta}$ planes, which has been suggested to be a characteristic of the early stages of ω formation within the body-centered cubic (bcc) lattice of the β phase [2].

Results of atom probe studies carried out on the same sample have been summarized in Fig. 7.2. An atom probe reconstruction (80nm x 80nm x 60nm) of the WQ Ti-10V-6Cu sample is shown in Fig. 7.2(a) with the Ti atoms (blue), V atoms (green) and Cu atoms (red) distinguished by color. All three species appear to be uniformly distributed within this sample of β matrix without any significant clustering of any given species, either individually or in combination. The average composition deduced from the data in this atom probe reconstruction is 83.6at.%Ti-

11.2at.%V-5.2at.%Cu, which compares well with the average measured composition of the alloy of 85.6at.%Ti-9.7at.%V-4.7at.%Cu. Confirmation of the compositional uniformity of this reconstruction has been carried out using a statistically relevant procedure in which the atoms within the entire reconstruction are divided into blocks of 10 atoms each, and the compositions of each of these blocks are subsequently plotted in a frequency distribution, where the number of blocks of a specific composition (Y-axis) are plotted against the composition (X-axis) as shown in Fig. 7.2(b). The experimentally observed distribution in Fig. 7.2(b) is almost identical to that calculated for a perfectly random solid solution, which would correspond to a standard binomial distribution. These results clearly indicate that there is minimal, if any, compositional segregation within the as-quenched Ti-10V-6Cu alloy and there is certainly no evidence of solute aggregation or partitioning on a scale equivalent to that of the ω phase observed by TEM. Coupling the results from the TEM and APT studies, it can be concluded that the ω domains in the water-quenched Ti-10V-6Cu sample form in a diffusion less manner and inherit the composition of the parent β matrix. The rapid cooling rate encountered by the sample during water quenching is likely to prevent any significant (and detectable) diffusion of alloying elements.

7.3.2 Ti-10V-6Cu β Solution Heat Treated / Water-quenched / Aged 60s at 500°C

TEM images from the same Ti-10V-6Cu alloy after water quenching and subsequent isothermal aging at 500°C for 60s are shown in Fig. 7.3. The $<011>_{\beta}$ zone axis electron diffraction pattern from this sample, shown in Fig. 3(a), clearly exhibits distinct ω reflections at the 1/3 and 2/3 $\{112\}_{\beta}$ positions. Dark-field TEM images from this sample, recorded using the ω reflections belonging to two distinguishable crystallographic variants, are shown in Figs. 7.3(b) and (c). Well-developed and comparatively coarse ω particles, exhibiting an ellipsoidal-like

morphology, are visible in these dark-field images. The particles have a minor axis in projection that varies between 10 and 50nm (average ~25nm) and a major axis between 25 and 100nm (average ~50nm), for an aspect ratio that is on average ~0.5.

Subsequent atom probe studies were carried out on this Ti-10V-6Cu sample aged 60s at 500ºC in order to assess any compositional fluctuations within the β matrix and in an attempt to determine the composition of the ω particles. An atom probe reconstruction of the Ti (blue), V (green), and, Cu (red) atoms within a nominal 100nm x 100nm x 200nm volume is shown in Fig. 7.4(a). The average composition of the sample volume employed in the overall reconstruction is 83.9at.%Ti – 10.3at.%V – 5.8at.%Cu, which is again very close to the measured alloy composition. However, there is now clear evidence of local variations in the concentrations of all three major elements within this reconstructed volume, with Ti-rich volumes (blue) distinguishable from local volumes rich in Cu (red) and V (green). One approach to highlighting these modulations in composition developed within the matrix is to define iso-concentration surfaces (or iso-surfaces in short) for the individual elements. The 3-D iso-surface reconstruction for a concentration of 92at.%Ti that is shown in Fig. 7.4(b) defines a near-continuous skeletal volume of matrix within which the Ti concentration consistently exceeds 92at.% and beyond which the local concentrations of Ti are everywhere lower. Fig. 7.4(c) shows similar iso-surfaces for concentrations of 17at.%V (green) and 9at.% Cu (red).

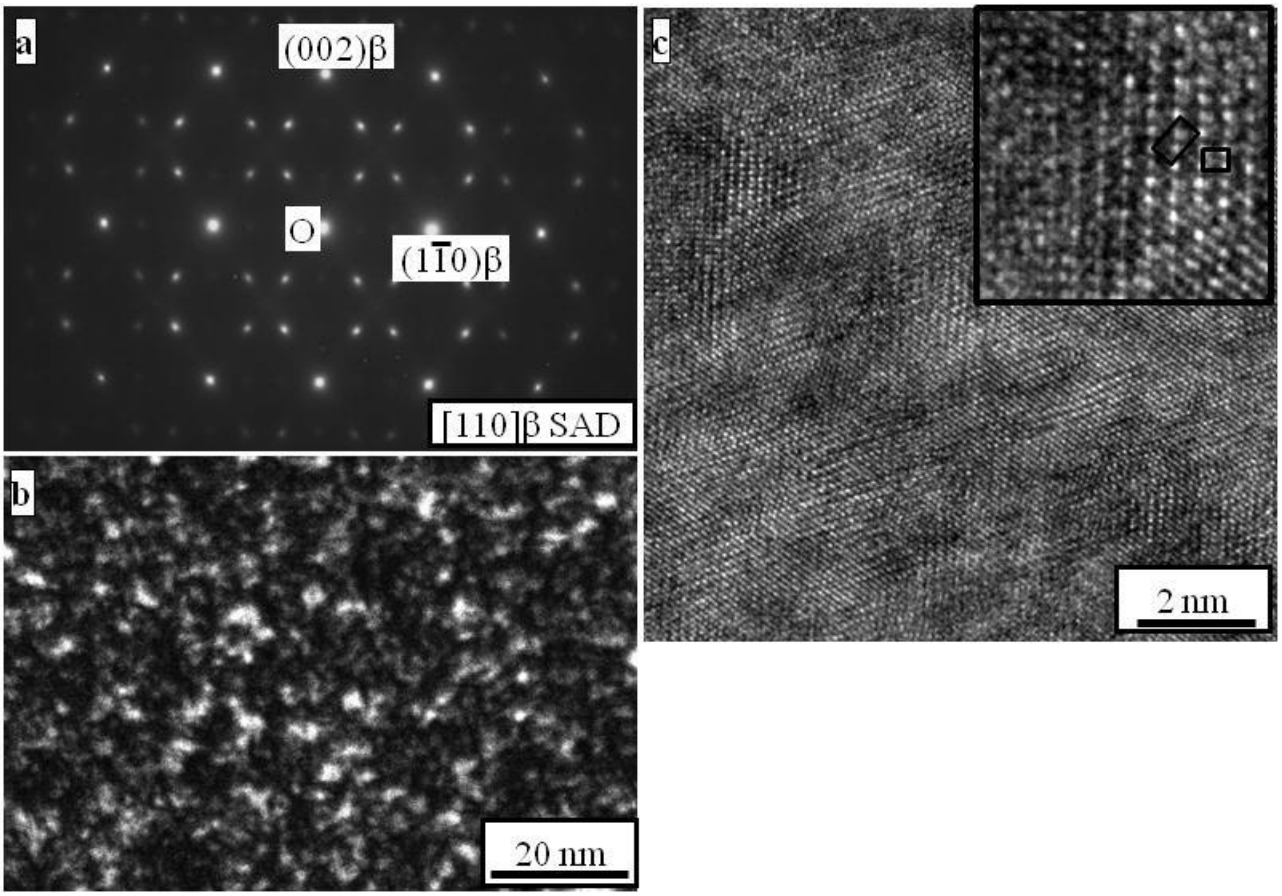

Fig.7.1 (a) Selected area diffraction pattern of <110>β zone axis of a β-solutionized and water quenched Ti-10V-6Cu sample showing the reciprocal lattice streaking at 1/3 and 2/3{112}β positions due to athermal ω domains. (b) Dark-field TEM image from the same sample, recorded using one of the ω reflections, showing nanometer scale ω domains, uniformly distributed within the β matrix. (c) High-resolution TEM image showing the early stages of ω formation within the β matrix. Inset shows a higher magnification view with the motifs for the β (small rectangle) and ω (large rectangle) phases marked.

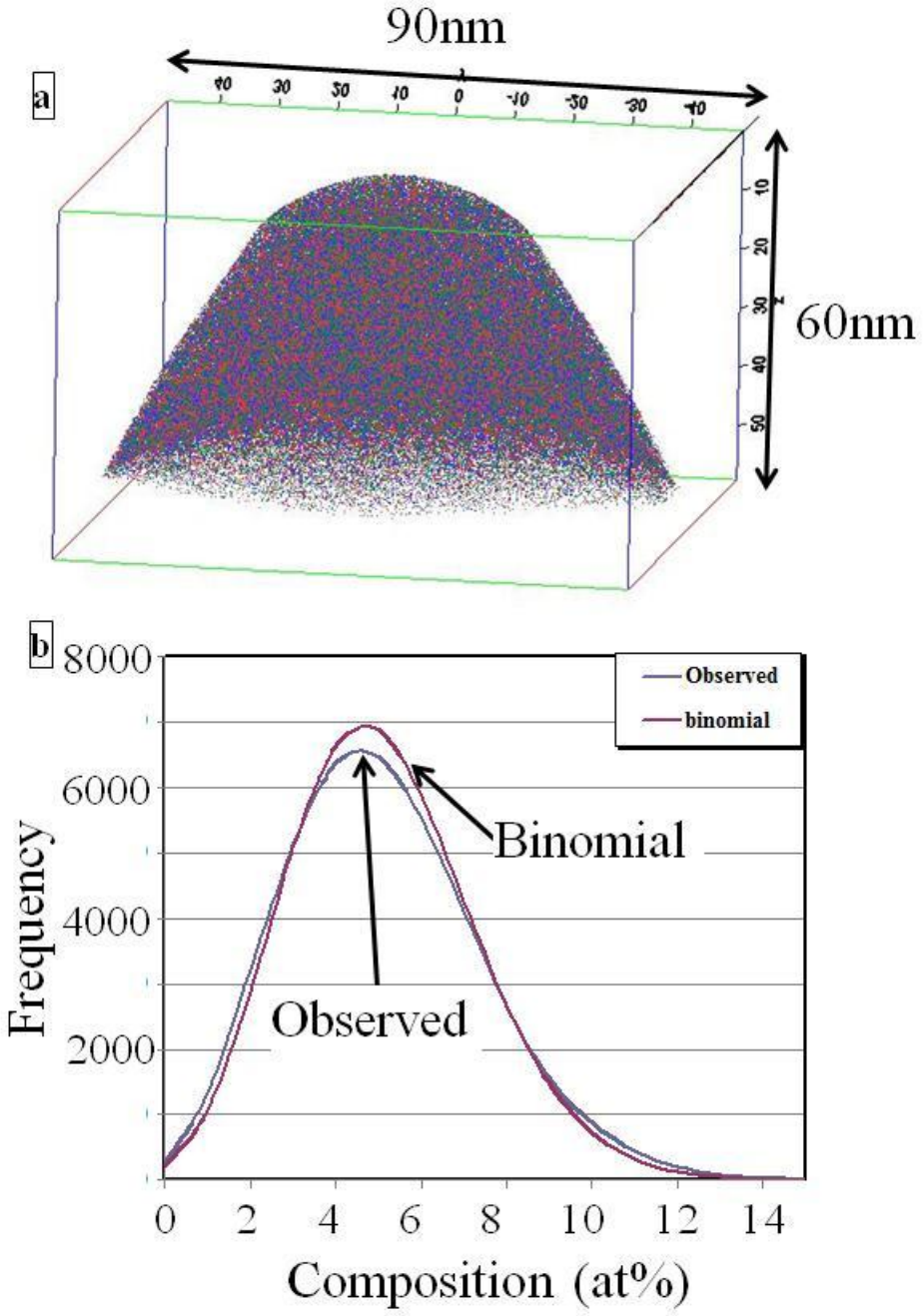

Fig. 7.2 (a) 3-DAP reconstruction of Ti(blue) V(green), and, Cu(red) atom distribution in solution heat-treated and water quenched Ti-10V-6Cu sample, showing the β matrix with a near-uniform solute distribution. (b) Frequency distribution plot from the same reconstruction showing near-identical curves for observed as well as for perfectly random solution (binomial distribution).

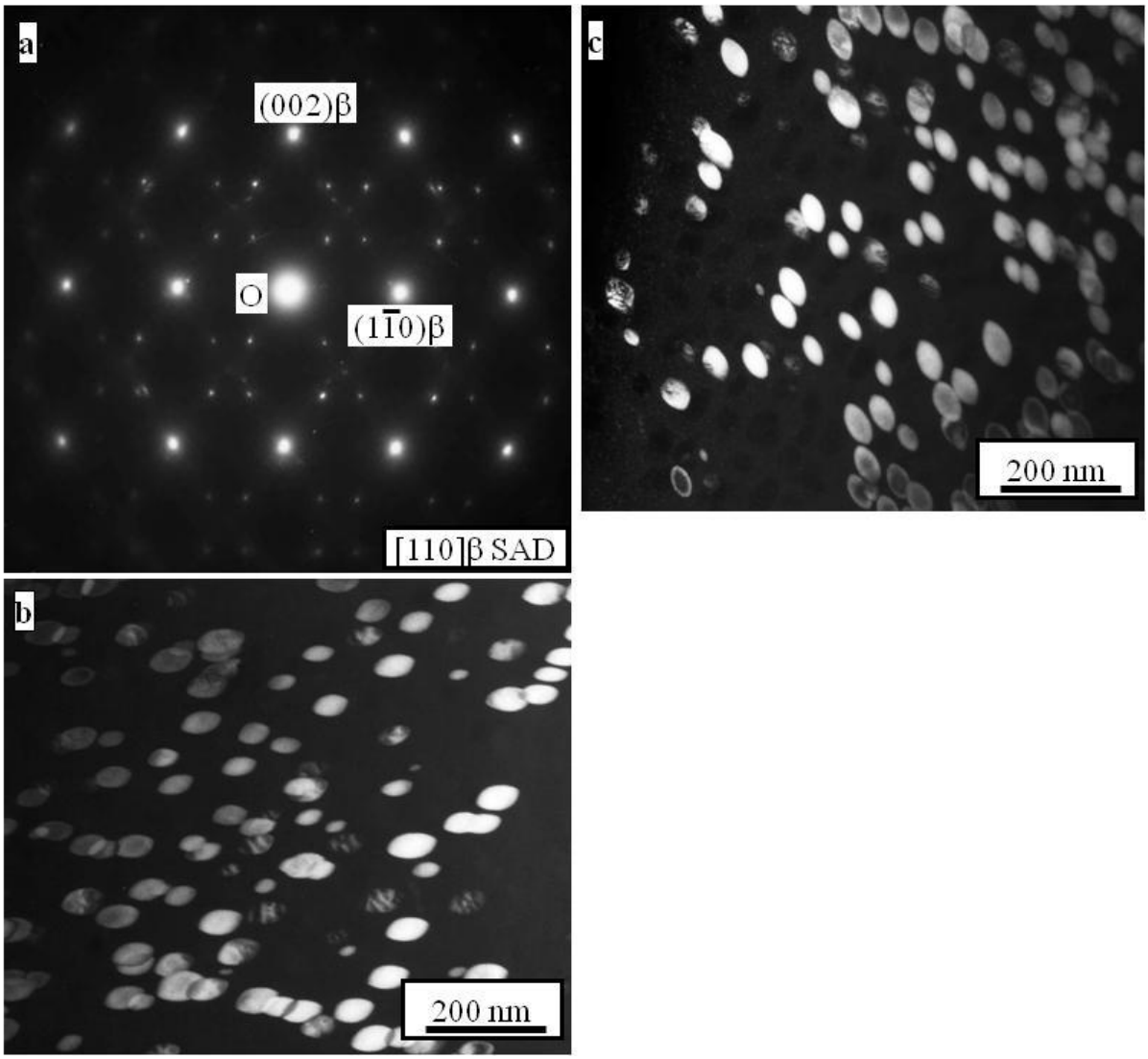

Fig.7.3 (a) Selected area diffraction pattern of <110>$_\beta$ zone axis of a sample of Ti-10V-6Cu alloy β-solution heat treated, water quenched and age 60s at 500ºC, showing distinct reflections at 1/3 and 2/3{112}$_\beta$ positions due to isothermal w domains. (b) and (c) Dark-field TEM images from the same sample, recorded using two different ω reflections to reveal two of four possible ω variants. The images show considerably coarser particles (compared with Fig. 7.1).

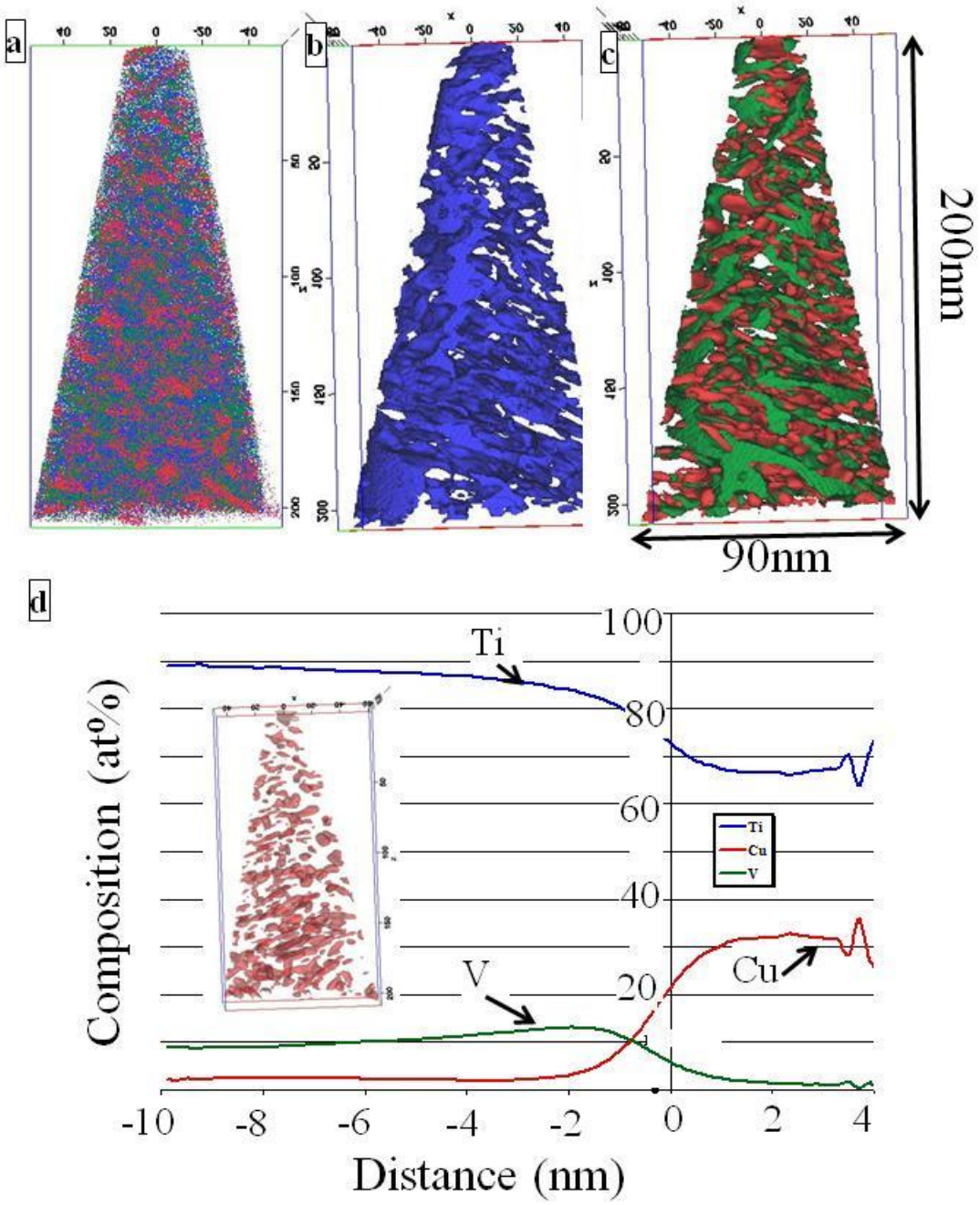

Fig. 7.4 (a) 3-DAP reconstruction of Ti(blue) V(green), and, Cu(red) atom distribution in sample of Ti-10V-6Cu alloy solution heat-treated, water quenched and aged 60s at 500C and air cooled Ti-10V-6Cu sample, showing compositional modulations uniformly across the reconstructed volume, with Ti-rich regions (blue rich) separated by Cu- and V-enriched regions (red and green rich respectively). (b) 3-D iso-surface view of the same reconstruction for 92at.%Ti. (c) 3-D iso-surface view of the same reconstruction for V (16at.%) in green, and Cu (9at.%) in red.

For the purpose of illustrating typical amplitudes of the modulations in composition within the 3-DAP reconstruction of Fig. 7.4, an arbitrary iso-surface at a concentration of 16at.%Cu was used to define interfaces surrounding local volumes determined to be substantially Cu-enriched, as shown in the inset to Fig. 7.4(d). The variations in the average elemental concentrations normal to all such interfaces are plotted in Fig. 7.4(d) as a function of distance from the interface position thus defined. It is observed that, within the Cu-enriched volumes, the local Cu concentration may be as high as 33at.%, with minimal V content (<1at.%) and correspondingly reduced levels of Ti (<70at.%). Beyond these volumes, the Cu concentration decreases rapidly to less than 2at.%, the V content increases to in excess of 10at.% and the Ti concentration typically exceeds 85at.%. The average compositions of the Cu-enriched and V-enriched volumes in this compositionally modulated reconstruction were 67.1at%Ti-1.5at%V-31.4at%Cu and 86.0at.%Ti-12.2at.%V-1.8at.%Cu respectively. Those volumes enriched in Cu approached the composition of the intermetallic compound Ti_2Cu, but TEM observations revealed no evidence of this phase in the sample aged 60s at 500°C.

Detailed analysis of such data sets (Fig. 7.4), together with the iso-surface constructions, indicated that the composition modulations within the reconstruction were typically of a length scale of the order of 5nm. As such, they are on a scale that is substantially refined (by as much as an order of magnitude) when compared with the dimensions of the ω-phasedomains in the same sample. For increased statistical significance, three further atom probe reconstructions of similar dimensions, from independent specimens subjected to the same heat treatment, were analyzed and they showed similar results in terms of the uniformity, and characteristic amplitudes and length scales, of the compositional modulations throughout the analysis volumes. In none of these cases was there any detectable evidence of partitioning of solute V and Cu on a length

scale commensurate with the scale of the ω particles expected in the nanostructure. Given that the electron micrographs of Fig. 7.3(b,c) represent just two of four crystallographic variants of ω domains that are densely and uniformly distributed in this sample, the combination of such a high volume fraction of ω phase and the scale of individual ω domains makes it improbable that at least segments of ω domains would not be encountered in the 100 nm x 100 nm x 200 nm atom probe reconstructions arising from four independent data sets.

It would appear that the fine-scale phase separation associated with the composition modulations evident in Fig. 7.4 takes place uniformly and continuously across both the β matrix and the ω domains. There is no obvious evidence of independent solute partitioning accompanying the necessarily rapid growth of the ω domains in this sample aged just 60s at 500ºC. The ω domains are effectively undetectable by atom probe tomography in this sample.

7.3.3 β Solution Heat Treated and Air-Cooled Ti-10V-6Cu

Representative TEM observations from the solution treated and air-cooled Ti-10V-6Cu alloy are shown in Fig. 7.5. A $<011>_\beta$ zone axis selected area electron diffraction pattern from this sample, with distinct ω reflections at the 1/3 and $2/3\{112\}_\beta$ positions, is shown in Fig. 7.5(a). Dark-field TEM images of the two associated variants of the ω domains are shown in Figs.7.5(b) and (c). Well-developed coarse-scale ω domains (~ 20-50 nm), exhibiting a more faceted or cuboidal morphology, are visible in these dark-field images. While the size scale of these ω domains is similar to those observed in the case of the sample solution treated, water-quenched and aged 60s at 500°C, the faceted, equiaxed morphology (average aspect ratio ~1.0) is distinctly different from the ellipsoidal forms observed in the quenched and aged sample. An atom probe reconstruction of the Ti (blue), V (green) and Cu (red) atom distributions within a typical 100nm x 100nm x 150nm volume is shown in Fig. 7.6(a). The average composition of the overall

sample volume involved in the reconstruction was 84.0at.%Ti–10.4at.%V–5.6at.%Cu and, although in reasonable agreement with the bulk alloy composition, may not necessarily be representative of the average alloy composition, since the reconstructed volume may not capture the appropriate average volume fractions of the β and ω phases present in this alloy.

The reconstructed sample volume represented in Fig. 7.6 is non-uniform in composition and there is, in this case, evidence of solute partitioning on a significantly coarser scale, with Ti-rich (blue) volumes separated by V-enriched (green), near-continuous matrix. Zones of Cu-enrichment appear to be associated preferentially with the interfaces between the Ti-rich and V-enriched volumes. The 3D iso-surface construction for a concentration of 92at.%Ti is shown along two different directions in Figs. 7.6(b) and (c). Based on these two 3-D representations, as well as other views (not shown) of this reconstruction, it can be concluded that the Ti-rich volumes are discrete, faceted and approximately equiaxed, consistent with particles of cuboidal morphology. With typical dimensions of 20-40nm, the size scale of these volumes is also commensurate with that of the average ω domains observed in the dark-field images shown in Figs. 7.5(b) and (c), and the cuboidal Ti-rich volumes observed in the APT reconstruction are thus deemed likely to correspond to the ω domains. The composition of these ω domains, averaged over all such volumes within the 3-D reconstruction shown in Figs. 7.6(b) and (c), was determined to be 95.9a.t%Ti-3.6at.%V-0.5at.%Cu, with only a very small residual Cu content present within these domains. The average composition of the surrounding β matrix (residual reconstruction volume), as determined from atom probe measurements, was 78at.%Ti-13.9at.%V-8.1at.%Cu.

Figs 7.6(d) and (e) show two different orientations of the same data set reconstruction, including iso-surfaces for Ti (92at.%) in blue, V (16at.%) in green, and, Cu (9at.%) in red. A second independent reconstruction from a separate specimen of the same sample is shown in Fig. 7.6(f) to confirm the general form of the atom distribution in the air-cooled sample and highlight the discrete coarse-scale, cuboidal Ti-rich ω domains. Both of these reconstructions also demonstrate clearly that the β matrix separating these domains is non-uniform in composition and exhibits a strong tendency for apparent (phase) separation into V-enriched (green) and Cu-enriched (red) zones at the nanometer length scale Figs 7.6(d)-(f).

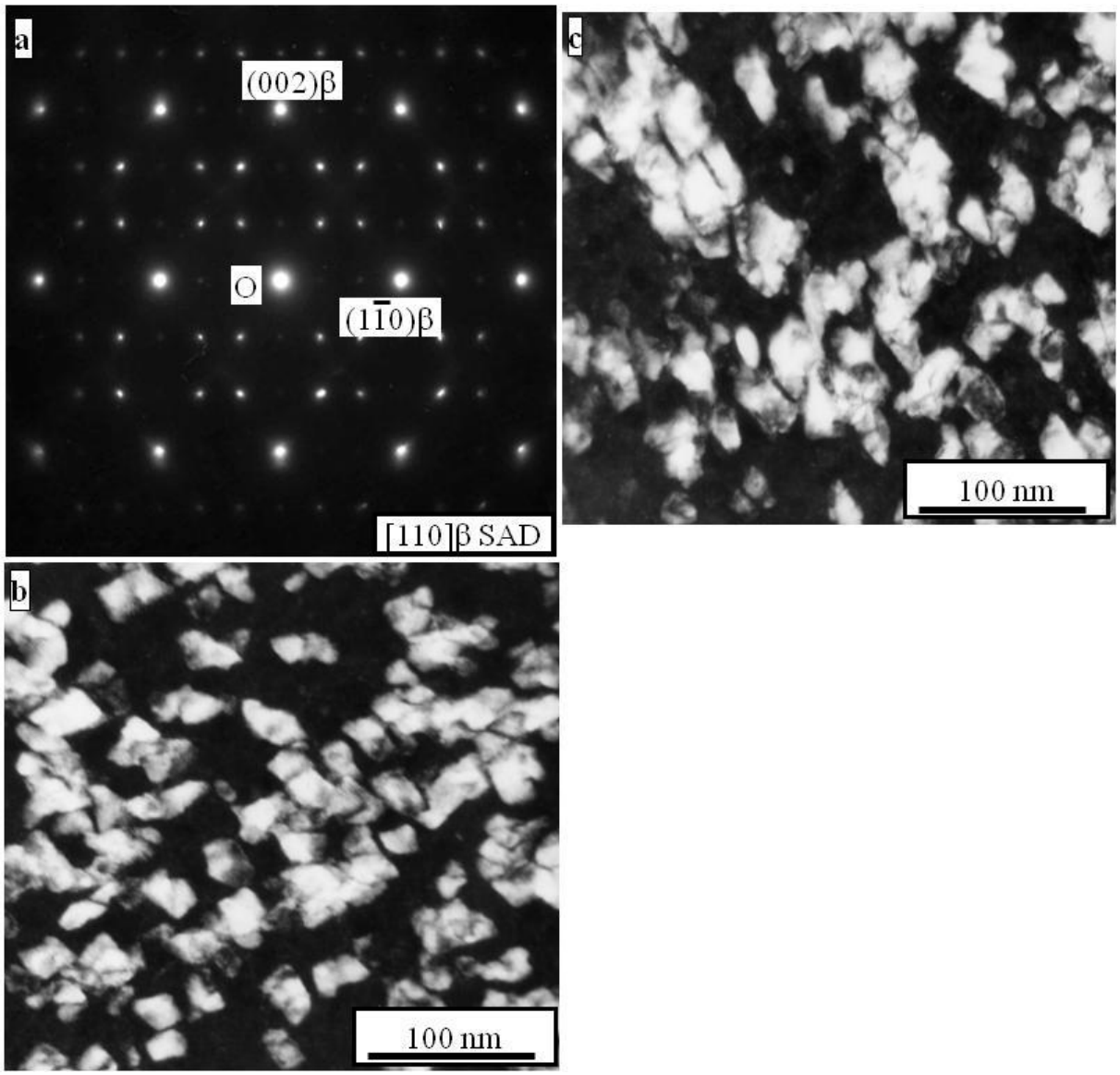

Fig. 7.5 (a) Selected area diffraction pattern of $<110>_{\beta}$ zone axis of a β-solution heat treated and air cooled Ti-10V-6Cu sample showing distinct reflections at 1/3 and 2/3$\{112\}_{\beta}$ positions due to isothermal ω domains. (b) and (c) Dark-field TEM images from the same sample, recorded using two different ω reflections to reveal two of four possible ω variants. The images show coarse ω particles that are more equiaxed and faceted in form (compared with Fig. 1).

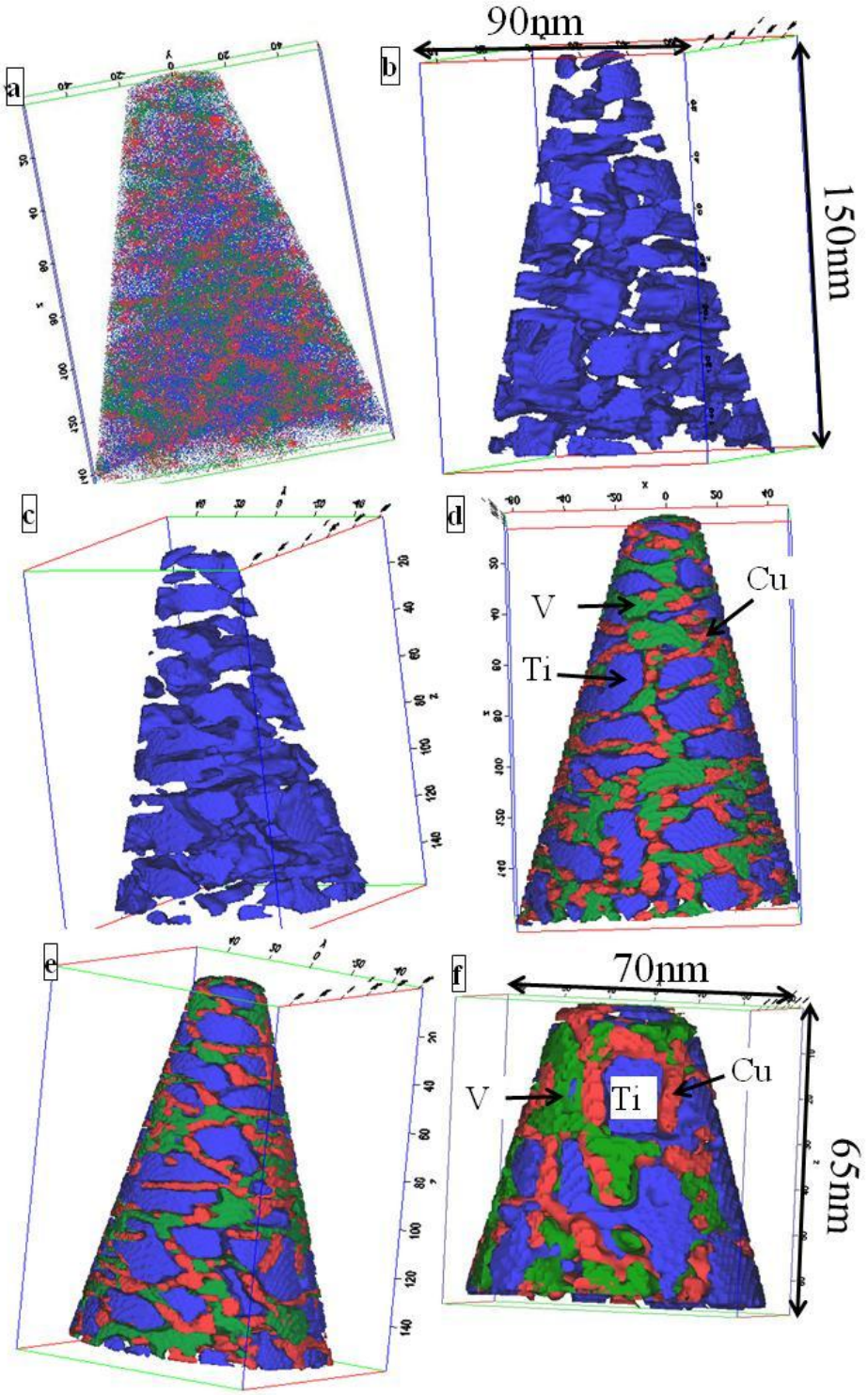

Fig. 7.6 (a) 3-DAP reconstruction of Ti(blue) V(green), and, Cu(red) atom distribution in solution heat-treated and air cooled Ti-10V-6Cu sample, showing compositional modulations within the reconstructed volume, with Ti-rich regions (blue rich) separated by Cu and V rich regions (red and green rich respectively). (b) and (c) 3-D iso-surface views of the same

reconstruction for 92at.%Ti, viewed along two different directions. (d)-(f) 3-D iso-surface views of the same reconstruction for Ti (92at.%) in blue, V (16at.%) in green, and Cu (9at.%) in red, viewed along different directions, showing the Ti-rich ω particles, along with Cu-enriched wetting layers and V-enriched volumes further from the ω domains.

A more detailed representation of the compositional variations between specific ω domains, and across the ω/β interface and through the adjacent β matrix, is evident in the iso-surface representations and the corresponding composition profiles shown in Figs 7.7(a) and (b). Fig. 7.7(a) shows two cuboidal ω domains separated by a volume of β matrix, within which there has apparently been phase separation into Cu- and V-enriched regions. There are Cu-enriched zones in close proximity to both the ω domains, with a V-enriched zone separating them. Concentration profiles for Ti, V and Cu, calculated as a function of position along a cylinder of 5nm diameter, shown in Fig. 7.7(a), are plotted adjacent to the 3-D reconstruction. The Cu-enriched layers adjacent to both Ti-rich ω domains are clearly evident, with the concentration in these zones approaching ~20at.%Cu. The V-enriched volume separating the two Cu-enriched zones within the β matrix approaches a concentration of ~30at.%V. Similar Cu-enriched wetting layers are visible on either side of the single ω domain shown in the separate reconstruction of Fig. 7.7(b).

While these composition profiles are readily interpretable, they suffer from the limitation of sampling only one specific direction for a specific ω domain. A more statistically significant representation of the concentration profile across the β/ω interfaces involves plotting a proximity histogram that averages the compositional gradient over all locations across these interfaces, along a local orthogonal direction [3]. Such proximity histogram concentration profiles for Ti, V and Cu are plotted in Figs. 8(a) and (b), from two separate atom probe reconstructions in which iso-surfaces have been defined at 92at.%Ti. The profiles represent averages across all such β/ω

interfaces, which are shown in the 3-D representations inset in the respective Figs. They demonstrate that the average Ti concentration within the ω phase exceeds 95at.%, the V concentration is typically <5at.% and the Cu concentration is <1at.%. Moving from the ω interface into β phase matrix, the V concentration increases continuously to a value of ~20at.% over a distance of some 5nm from the interface. In contrast, the Cu is locally enriched (to concentrations exceeding ~10at.%) within a zone of ~5nm width adjacent to the interface, but the Cu concentration then declines significantly with increasing distance from the interface. While the form of this information is similar to that in the 1-D composition profiles shown in Fig. 7.7, the profiles in the proximity histograms of Fig. 7.8 are averaged across the entire ω/β interface, for all such interfaces, and consequently the levels of Cu and V enrichment are not the same. For example, while the local Cu enrichment adjacent to a particular section of the ω/β interface can be as high as ~20at.%, as in Fig. 7.7(b), the average Cu enrichment surrounding the ω domains is ~10at.%, as in Figs 7.8(a) and (b).

In order to quantify and understand the phase separation (compositional clustering) occurring in the β matrix in greater detail, the Ti-rich ω domains were subtracted from the 3-D atom reconstruction and the remaining volume of β matrix phase analyzed separately. The extracted β matrix from one such atom probe reconstructions is shown in Fig. 7.9(a), with the Ti, V and Cu atoms again plotted in blue, green and red, respectively. The significant variations in composition within what is solely β phase are clearly evident, and the local aggregation of Cu is further amplified in Fig. 7.9(b) by plotting an iso-concentration surface with Cu = 16at.% to delineate the Cu-enriched zones within the β matrix. Concentration profiles with respect to this iso-surface (abscissa x = 0) have been plotted for Ti, V and Cu, in the form of proximity histograms, in Fig. 7.9(c). The Cu-enriched zone lies to the right and the V-enriched volume to

the left; the average compositions of the Cu- and V-enriched volumes within the phase-separated β matrix of the air-cooled sample, measured using atom probe, were 64at.%Ti-3.2at.%V-32.8at.%Cu and 79.3at.%Ti-17.4at.%V-3.3at.%Cu, respectively. Based on the composition profile, it appears that there are certain volumes within the β matrix in which the Cu concentration is as high as ~34at.%, which might render these volumes amenable to precipitation of the intermetallic compound Ti_2Cu. While there was no direct evidence of Ti_2Cu formation from the TEM studies on the air-cooled Ti-10V-6Cu alloy, this does not preclude the possibility that these Cu-enriched, phase-separated regions within the β matrix may precipitate Ti_2Cu on post air-cooling aging treatments.

7.4 Discussion

The ternary Ti-V-Cu system is rather interesting from the perspective of the thermodynamic interaction parameters between the various binary elemental combinations involved. While the Ti-Cu and Ti-V binary systems have small positive enthalpies of mixing, ΔH_{mix} = +7-8 kJ/mol > 0 [4] and thus might each be expected to exhibit a weak tendency to solute aggregation in solute-lean solid solutions, the Cu-V binary system has a comparatively large positive ΔH_{mix} = +70 kJ/mol >> 0 [5]. Consequently, there is likely to be a strong tendency for de-mixing of solute (or phase separation) within any β-phase solid solution in a Ti-10V-6Cu alloy.

This alloy also exhibits a strong tendency for formation of metastable ω phase, presumably via the well-accepted mechanism involving displacive collapse of the $\{111\}_\beta$ planes [2,6,7]. While phase separation within bcc β solid solution can be considered a compositional instability arising from the individual or collective clustering tendencies of the various solute elements, formation of ω arises from a structural instability typically attributed to anisotropic

elastic softening of the bcc structure [2, 6, 7]. The relationship and possible competition between these two types of instabilities, and the potential dominance of one over the other, will ultimately determine the resultant nanostructure under conditions in which both are potentially operative. Results of the present investigation clearly indicate that changing the rate of cooling of this alloy from the high temperature single phase β field, strongly influences the sequence of transitions and the extent to which they may compete during early-stage decomposition of the supersaturated β phase. The effect of the competing instabilities consequently modifying the sequence of transformations is discussed in detail in the following sections.

7.4.1 Formation of ω Phase During Water Quenching

During rapid water quenching from the high temperature β single phase-field, there is insufficient time (at high temperatures) for any substantial long-range diffusion of the solute atoms and consequently any detectable compositional clustering to take place within the supersaturated β phase. The resulting quenched Ti-10V-6Cu alloy exhibits compositional homogeneity, based on atom probe analysis. Nevertheless, during the water-quenching, ultra-fine, nanometer-scale ω domains form via what is conventionally described as the athermal collapse of the $\{111\}_\beta$ planes [6-10]. The athermal nature of the β to ω transformation in this case is rationalized on the basis that the transformation apparently occurs during the quench and a high quench rate cannot inhibit the transformation. The so-called athermal ω domains typically inherit the composition of the parent β phase [8, 9].

7.4.2 Concurrent Growth of ω Phase and β Phase Separation during Short-Term Isothermal Aging (500°C/60s)

A combination of unexpected phenomena emerged during a very short-term (60s at 500°C) isothermal aging treatment, subsequent to the water-quenching of solution treated Ti-

10V-6Cu. Observations using TEM revealed relatively coarse-scale (~40-100nm) ω domains, exhibiting classical ellipsoidal morphology, in the aged sample. Considering the fact that the athermal ω domains in the water-quenched sample were only ~2-5 nm in size, there has been extremely rapid growth of these domains in just 60s at 500°C. However, when specimens of the same sample were observed in the atom probe, there was no evidence of solute partitioning on the same size scale (40–100nm) as that of the ω domains. The ω domains were essentially undetectable in four independent and large sets of representative atom probe data interpreted purely in terms of compositional mapping. These observations suggest that the ω domains grow rapidly during short-term (60s at 500ºC) isothermal aging via a mechanism that does not involve long-range substitutional diffusion and might thus be regarded as diffusion less. Given that the atomic displacements associated with growth are short-range, growth might be considered to be interface-controlled, but clearly the ω/β interface is glissile and capable of migrating at high velocities.

What was observed in the APT results, Fig. 7.4, was clear evidence of the development of compositional modulations (or phase separation) at a much finer length scale (~5-10nm). These modulations appeared to develop uniformly throughout the volume of all specimens examined and, in addition to the refined scale, were of a form that did not bear any obvious resemblance to the morphology of the ω domains observed in the dark-field TEM images, Fig. 7.3. These observations suggest that during the short-term aging treatment, the rapid growth of the ω domains is accompanied by shorter-range modulations in solute content that develop concurrently but apparently independently. The form and scale of the modulations suggest a process that does not acknowledge a difference between the β and ω structures and the interfaces

that exist between these constituent phases. There appears to be no direct relationship between the growth of the ω phase and the compositional modulations.

The refined length scale (~5-10nm) characteristic of the modulations in composition developed uniformly within and across the β and ω phases during the 60s aging treatment at 500ºC is likely to reflect the limited time for longer-range diffusion. However, quantitative assessment has proven difficult. Diffusion data for solute diffusion in simple binary systems Ti-V and Ti-Cu [11, 12] are limited to temperatures typically in excess of 900-1000°C, and exhibit significant variation. Extrapolation to lower temperatures is subject to significant uncertainty. Based on the available binary data extrapolated to 500ºC, calculations of diffusion lengths $x = 2\sqrt{Dt}$, (where D is solute diffusivity and t diffusion time) give values in the range 1- 525nm for Cu in β-Ti and the range 0.001 – 165nm for V in β-Ti, with the preponderance of values for both in the range 1-10nm. Without being definitive, these values indicate that it is not unreasonable to conclude that the scale of the composition modulations is diffusion-limited.

The refined scale of the modulations compared to that of the ω domains (40-100 nm) suggests that there will be no significant difference in the average compositions of the ω domains and the adjoining β matrix, and on average any lattice mismatch between these two phases will be small. The continuity of the composition modulations across ω/β interfaces also ensures that any local misfit at these interfaces will be minimized. It is thus unsurprising that the ω domains preserve an ellipsoidal morphology typical of what are commonly deemed low-misfit systems [13-19].

7.4.3 β Phase Separation Preceding Formation of ω During Air-Cooling

The situation is rather different in the case of the slower air-cooling treatment of the same alloy from the high temperature β single phase-field, wherein the sample experiences longer

residence times at higher temperatures, allowing for increased solute diffusion during the cooling process. In this case, the nanostructure comprises coarse (nm), cuboidal ω domains that are rich in Ti and depleted in both V and Cu, in a matrix in which there is also significant internal partitioning of the solute V and Cu. There are commonly zones enriched in Cu immediately adjacent to the ω domains, while the remaining volumes of matrix remote from the domains are V-enriched.

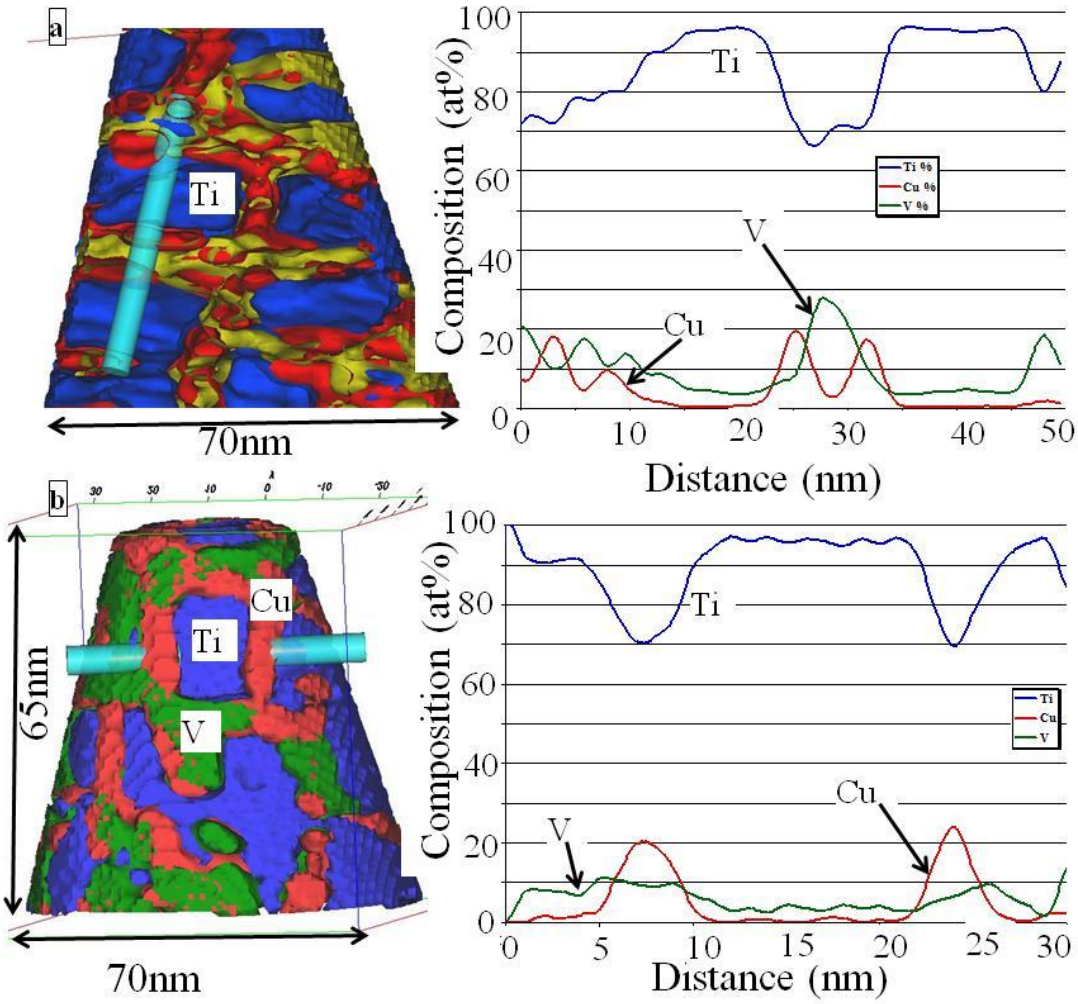

Fig. 7.7 (a) 3-D cross-sectional view of same reconstruction for Ti (92at.%) in blue, V (16at.%) in green and Cu (9at.%) in red, showing two cuboidal ω particles separated by a volume of β phase, within which the Cu- and V-enriched regions have phase-separated. Corresponding 1-D composition profiles for Ti, V and Cu along the long axis of the cylinder shown schematically are plotted adjacent to the 3-D reconstruction. (b) 3-D iso-surface view of the same

reconstruction showing identical volumes as in (a). Corresponding 1-D compositional profile show Cu-enriched zones around the ω particles.

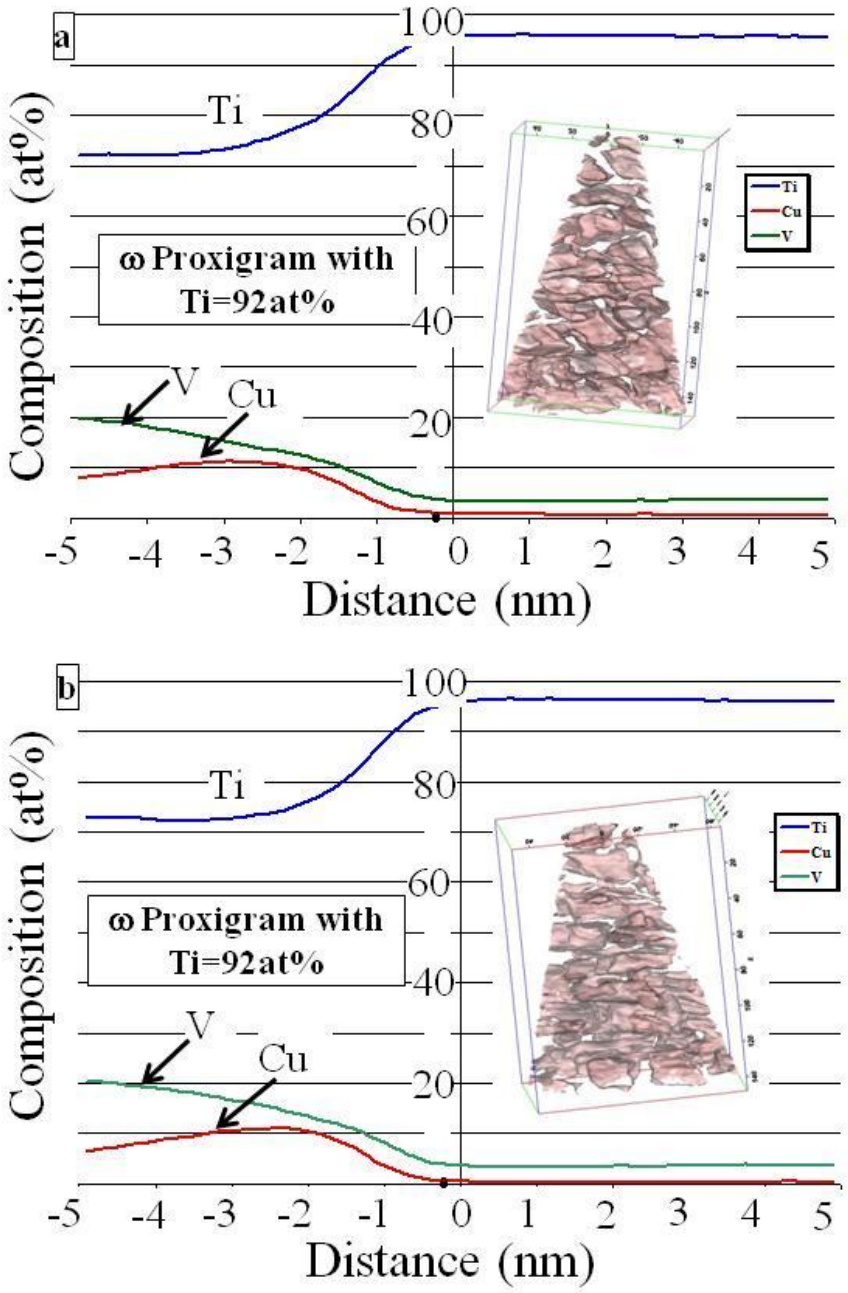

Fig. 7.8 (a) and (b) Two different proximity histogram profiles for Ti, V and Cu using the above 3-D reconstruction for Ti (92at.%), showing local enrichment of Cu around the ω particles, while at longer distances from the interface, the V content increases.

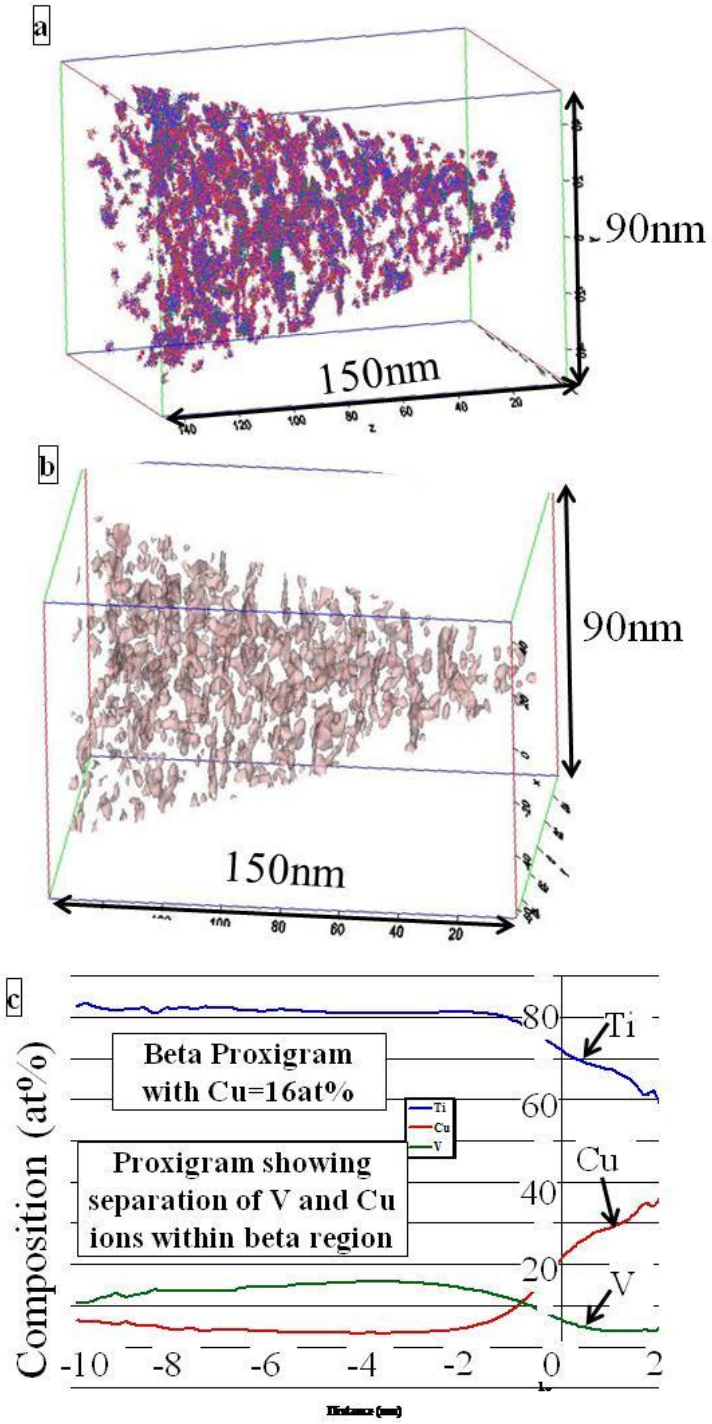

Fig. 7.9 (a) An extracted volume of β matrix from one of the atom probe reconstructions, where the Ti, V, and, Cu atoms have been plotted in blue, green and red respectively, showing the compositional partitioning of the solute elements. (b) Corresponding iso-surface with Cu = 9 at.% which delineates the Cu-enriched volume within the β matrix. (c) 1-D compositional profiles for Ti, V and Cu showing separation of V and Cu ions within the β regions.

The intrinsic tendency to de-mixing of β-phase Ti-10V-6Cu solid solution, coupled with extended periods for diffusion at elevated temperatures in the air-cooled sample, will likely provide the opportunity for phase separation within the β phase, leading to solute (V, Cu)-enriched regions (designated β_1) and solute-depleted regions (designated β_2). It is anticipated that any such decomposition will occur within the metastable miscibility gap for this alloy composition and at higher temperatures where solute transport is most rapid. The associated modulations in composition will be accompanied by local variations in lattice dimensions, with the scale of the lattice misfit and the associated gradient in elastic strain energy increasing with increase in the average composition difference between β_1 and β_2.

Furthermore, if the β phase separation occurs within the coherent spinodal, then the composition modulations are expected to develop along the elastically-soft $<001>_\beta$ directions. A previous investigation of Zr_3Al-Nb alloys [20] has indicated that three orthogonal compositional waves can superimpose, resulting in solute-rich nodes separated by solute-depleted regions, with the resulting form of these phase-separated regions being cuboidal. At lower temperatures, one of these phase separated regions, either β_1 or β_2, will likely be susceptible to transformation to ω phase. Previous studies on Ti alloys have shown that alloying elements that are either α or β stabilizers can reduce the intrinsic stability of ω [21, 22]. When coupled with the present observations and previous reports that ω forming isothermally is solute-depleted, it is reasonable to conjecture that the solute-depleted β_2 regions are most likely to transform to ω phase at temperatures below the ω solvus.

In addition to the composition difference and thus misfit with surrounding matrix that they inherit, the morphology of these ω domains may well be constrained by the form of the phase-separated pockets within the β matrix that are cuboidal in shape. Any further isothermal

growth or cooling to lower temperatures will likely result in further partitioning of solute, with the ω domains rejecting both V and Cu. Those ω domains examined in the air-cooled sample contained typically <5at.%V and <1at.%Cu. Any increase in the difference in the average compositions of ω and β matrix will sustain an increase in lattice misfit and thus a cuboidal ω morphology.

Based on the detailed atom probe analyses of the composition profiles across the ω/β interface, it appears that the V and Cu rejected by the growing ω precipitates do not distribute homogeneously within the surrounding β matrix, but partition into relatively V-enriched and Cu-enriched regions. The proximity histograms of Fig. 7.8 suggest that there is typically Cu enrichment immediately adjacent (within ~5nm) to the ω/β interface. The strong positive enthalpy of mixing in the binary Cu-V system would suggest that these elements are likely to disassociate in any solid solution in which they are present in significant concentrations, and this would seem to be the likely origin of the metastable phase separation observed within the β matrix. Interestingly, the levels of solute partitioning in the V-enriched and Cu-enriched volumes within the β phase in the air-cooled sample are very similar to those observed within both the β and ω phases, which were compositionally indistinguishable, in the case of the quenched sample aged 60s at 500°C. The average composition of the Cu-enriched zones in the air-cooled sample was, for example, determined to be 64at.%Ti-3.2at.%V-32.8at.%Cu from atom probe measurements. Such high Cu contents could potentially lead to the precipitation of Ti_2Cu on subsequent annealing. Longer-term aging experiments are currently underway and the analysis of these samples constitutes part of future work.

7.5 Summary

With a focus on the earliest stages of decomposition, the present observations indicate that nano-scale (<10nm) fluctuations or modulations in composition (phase separation) may develop uniformly throughout the β matrix of this Ti-Cu-V alloy, concurrently with and apparently independently of the formation and rapid growth of the ω phase. Water-quenching an alloy of composition Ti-10V-6Cu from the high temperature single β phase field preserves compositional homogeneity but leads to the formation of 2-5nm athermal ω domains. When subsequently aged isothermally 60s at 500°C, these domains grow rapidly to sizes of 40-100nm, without any significant long-range diffusional partitioning of the alloying elements between the β and ω phases. However, fine scale (5-10nm) modulations in solute concentration develop uniformly within and across both these phases. In contrast, on slower air cooling of the Ti-10V-6Cu alloy from the high temperature single β phase field, phase separation, presumably via spinodal decomposition, precedes the ω formation. Results indicate that ω domains develop within solute-depleted pockets of cuboidal morphology, the shape likely being defined by the superposition of three orthogonal $<001>_{\beta}$ modulations in composition. Furthermore, the strong tendency of Cu and V to disassociate within solute-rich β matrix, leads to partitioning of the solute into V-enriched and Cu-enriched volumes, with Cu concentrations as high as ~33at.% in some volumes of the β matrix.

7.6 References

[1] Boyer RR, Welsch G, Collings EW. Materials Properties Handbook: Titanium Alloys, ASM Handbook; 1994.

[2] Banerjee S, Mukhopadhyay P. Phase transformation: examples from titanium and zirconium alloys; Oxford, UK: Pergamon Press; 2004.

[3] Hellman OC, Vandenbroucke JA, Rusing J, Isheim D, Seidman DN. Micro. Microanalysis 2000;6:437.

[4] Collings EW ed, Timmerhaus KD, Clark AF. Springer Publication, NY:1986;57.

[5] Turchanin MA. Powder Met and Metal Ceramics 2006;45(5-6):272.

[6] De Fontaine D, Paton NE, Williams JC. Acta Metall 1971;19:1153.

[7] *Williams JC*, *De Fontaine D*, *Paton NE*. Met Trans 1973;4:2701.

[8] Boyer RR, Welsch G, Collings EW. Materials Properties Handbook: Titanium Alloys, ASM Handbook; 1994.

[9] Sass SL. J. Less-Common Metals 1972;28:157.

[10] McCabe KK, Sass SL. Phil Mag 1971;23:957.

[11] Mehrer H. Numerical Data and Functional Relationships in Science and Technology, in Landolt-Börnstein (Eds.). Diffusion in Solid Metals and Alloys. Berlin: Springer-Verlag; 1990. Group III, Vol. 26, pp. 102-4.

[12] G. Neumann G, C. Tuijn C Self-Diffusion and Impurity Diffusion in Pure Metals: Handbook of Experimental Data, Pergamon Materials Series, V. 14, London (2009) p. 154/160.

[13] Pennock GM, Flower HM, West DRF. Titanium „80: Science and Technology 1980:1343.

[14] Langmayr F, Fratzl P, Vogl G. Phys Rev, 1994;49B(17):11759.

[15] Moffat DL, Larbalestier DC. Met Trans A 1988;19A:1687.

[16] Menon ESK, Krishnan R. Jour Mater Sci 1983;18:375.

[18] Williams JC, Blackburn MJ. Trans TMS-AIME 1969;245:2352.

[19] Duerig TW, Terlinde GT, Williams JC. Metall Trans 1980;11A:1987.

[20] Banerjee S, Tewari R, Dey GK. Intl Jour of Mat Res 2006;97(12):963.

[21] Vassel A. (editors Eylon D, Boyer RR, Koss DA) Beta Titanium in the 1990ʻs, , TMS Warrendale, PA: 1993;173.

[22] Williams JC, Hickman BS, Leslie DH. Metall Trans 1971;2:477.

CHAPTER 8

SUMMARY AND FUTURE WORK

The focus of this present study was directed at improving the understanding of the mechanism of β phase separation and its influence on precipitation of second phases like ω and α in simple binary and ternary β titanium alloys. The first investigations were carried out on rapidly cooled Ti-18wt% Mo alloys to understand the mechanism of formation of isothermal ω precipitates by coupling high resolution scanning transmission electron microscopy with three dimensional atom probe studies. Preexisting β phase separation and resulting isothermal ω phase transformation in the Mo depleted pockets present due to phase separation was uniquely identified. For the first time the atomic displacements along <111>β directions required for β to ω phase transformation were resolved using HRSTEM imaging and these displacements were quantified by atomic column intensity measurements. Subsequent solute partitioning and the development of three dimensional morphology of ω precipitate on isothermal ageing were investigated by coupling three dimensional atom probe with high resolution TEM imaging. Thereafter first principle computations were carried out using Vienna ab-initio simulation package (VASP) to calculate the energetic of β to ω phases in Ti-Mo binary alloys. The minimum energy pathway generated by nudged elastic band computations showed existence partially transformed configurations offering states of local energy minima. Thus instead of complete collapse of atomic planes where the shift of atomic columns have to be $0.5d_{222}$, NEB calculations showed that for Ti-8.33at%Mo the minimum energy configuration corresponded to 0.25d222, hence the collapse being partial. The quantified displacements by HRSTEM intensity measurements in rapidly cooled Ti-9at% Mo showed similar value of partial collapse of 0.2 d(222) present within the Mo depleted pockets.

Subsequently the development of β phase separation in ω destabilized model ternary Ti-20Mo-5Al alloys were studied by coupling insitu high energy X-ray diffraction with aberration corrected TEM and three dimensional atom probe analysis. The Al addition helped to decouple the effects of β phase separation from the concurrent ω phase formation observed in Ti-18wt% Mo alloys. The occurrence of β phase separation in this β titanium alloy was uniquely identified by probing the peak splitting of β{200} peak in X-ray diffraction, appearance of satellite reflections in β [001] zone axis electron diffraction and lattice straining observed using HRTEM imaging. Using atom probe tomography the β phase separation pattern in the alloy was uniquely identified to be of a solute lean-solute rich character creating a modulated β structure with regions rich in Ti and region rich in both Mo and Al. The coherent arrangement of solute depleted β_1 regions and solute rich β_2 regions were imaged using HRTEM. Influence of the β phase separation on subsequent α phase nucleation was studied by the progressive development of $(10\bar{1}0)_\alpha$ peak during in situ HEXRD experiments. Also selected area electron diffraction showed the progressive development of additional reflections from the α phase precipitates. Aberration corrected HRTEM imaging captured the early stage nuclei of α phase formed in the alloy after aging for 10 hours at 400^{o}C. Three dimensional atom probe studies were able to identify a reverse diffusion of Al to the α phase from the solute rich β phase regions on longer duration isothermal aging at 400^{o}C. A substantial enrichment of Al in α phase was observed after 1hr aging at 620^{o}C. The experimental evidence pointed to the existence of a spinodal mode of phase separation and subsequent nucleation of α at the solute lean β1 regions. This was followed by back diffusion of Al to these nano-scale α precipitates.

Lastly the concurrent β phase separation and ω phase formation during continuous cooling in Ti-10V-6Cu alloy was studied. Water quenching of the alloy showed formation of athermal ω domains which grew substantially on isothermal ageing at 500^{o}C for 60 seconds apparently independent of a uniform β phase separation observed in the alloy across both β and ω phase regions. The w phase formed on aging after water quenching inherited the parent β composition and hence had an ellipsoidal morphology, a characteristic of low misfit alloy systems. However a slower cooling attained by air cooling of the alloy lead to the development of cuboidal Ti rich regions presumably due to a spinodal decomposition of β matrix followed by the β to ω transformation in such solute depleted β_1 regions giving cuboidal morphology to the ω phase. Within the β matrix a phase separation between Cu and V was observed leading to regions with Cu concentration as high as 33 at% which could probably form Ti_2Cu precipitates on longer term ageing.

There is a huge scope for further investigations in this field of study. Some the important future directions are listed below.

1. In the current study no attempt has been made to study the athermal ω phase domains that can be formed in Ti-Mo binary alloys on water quenching. Hence it will be of interest to study the formation of athermal ω and their growth on low temperature ageing in absence of a pre existing phase separation in the β matrix. Also efforts can be made to couple the current results with in situ High energy X-ray diffraction experiment during similar ageing treatment of rapidly cooled Ti-18wt%Mo alloy to probe the sequence of lattice parameter change of ω phase due to the continuous solute partitioning. Such an experiment would help to conclude the correlation of

continuous development of compositional partitioning with the extent of displacive collapse in ω precipitates.

2. Other binary Ti-Mo compositions need to be manufactured and heat treated in similar conditions to confirm the effect of composition on β phase separation and the extent of displacive collapse of (111) planes to form ω phase.
3. The system size of first principle calculations can be increased to 48 or 96 atoms to obtain more composition data points within the 0 to 16.66at% range. This would help in identifying the exact dependency of composition on extent of displacive collapse. Also the atomic displacements in the energy minima configurations in 8.33at% and 12.5at% compositions need to be studied in detail to identify any underlying empirical relation between composition and average atomic displacement providing the lowest energy configuration. Also effect of vacancies on β to ω transformation can be studied using similar first principle calculations.
4. Detailed peak fitting and area under the curve analysis of high energy synchrotron X-ray diffraction data is required to obtain lattice parameter and volume fraction information of α and β phases in Ti-20Mo-5Al alloy. EELS and EFTEM studies can be performed to strengthen the observation of phase separation and subsequent nucleation of α in Ti20Mo5Al alloys.
5. Further studies are required to understand the annihilation of the nature of quenched in phase separation on isothermal ageing of Ti-20Mo-5Al alloy. Short duration ageing of quenched alloy can be coupled with TEM electron diffraction, HRTEM imaging and three dimensional atom probe analysis to obtain insights towards this mechanism. Longer duration ageing experiments at 400^{o}C are required to identify the point of

reversion of Al to α phase on isothermal ageing of Ti20Mo5Al alloys. Tendency of beta phase separation in such alloys can also be studied by thermodynamic calculations based on PANDAT.

6. The growth of ω precipitates in β solutionized water quenched and aged at 500^{o}C 60s is found to be independent of the uniform composition modulation developed in the β matrix. Such a composition independent growth is very similar to the athermal ω formation. However the current observation is an athermal mode - purely displacive transformation occurring on isothermal aging. A detailed analysis of the atomic mechanism of such a phase transformation would help in obtaining some newer insights to β to ω phase transformation.